DESIGN AND FABRICATION OF STRAINED LIGHT EMITTING GERMANIUM MICROSTRUCTURES BY LIQUID PHASE EPITAXY

A THESIS SUBMITTED TO
THE GRADUATE SCHOOL OF NATURAL AND APPLIED SCIENCES
OF
MIDDLE EAST TECHNICAL UNIVERSITY

BY

BUSE ÜNLÜ

IN PARTIAL FULFILLMENT OF THE REQUIREMENTS
FOR
THE DEGREE OF MASTER OF SCIENCE
IN
MICRO AND NANOTECHNOLOGY

SEPTEMBER 2021

Approval of the thesis:

DESIGN AND FABRICATION OF STRAINED LIGHT EMITTING GERMANIUM MICROSTRUCTURES BY LIQUID PHASE EPITAXY

submitted by **BUSE ÜNLÜ** in partial fulfillment of the requirements for the degree of **Master of Science in Micro and Nanotechnology, Middle East Technical University** by,

Prof. Dr. Halil Kalıpçılar
Dean, Graduate School of **Natural and Applied Sciences** _____

Prof. Dr. Almıla Güvenç Yazıcıoğlu
Head of the Department, **Micro and Nanotechnology** _____

Assoc. Prof. Dr. Selçuk Yerci
Supervisor, **Micro and Nanotechnology, METU** _____

Assist. Prof. Dr. Çiçek Boztuğ Yerci
Co-Supervisor, **Electrical and Electronics Eng., TED Uni.** _____

Examining Committee Members:

Assoc. Prof. Dr. Alpan Bek
Physics, METU _____

Assoc. Prof. Dr. Selçuk Yerci
Micro and Nanotechnology, METU _____

Assoc. Prof. Dr. Serdar Kocaman
Electrical and Electronics Eng., METU _____

Assist. Prof. Dr. Talip Serkan Kasırga
Physics, Bilkent University _____

Assoc. Prof. Dr. Dinçer Gökcen
Electrical and Electronics Eng., Hacettepe University _____

Date: 08.09.2021

I hereby declare that all information in this document has been obtained and presented in accordance with academic rules and ethical conduct. I also declare that, as required by these rules and conduct, I have fully cited and referenced all material and results that are not original to this work.

Name Last name : Buse Ünlü

Signature :

ABSTRACT

DESIGN AND FABRICATION OF STRAINED LIGHT EMITTING GERMANIUM MICROSTRUCTURES BY LIQUID PHASE EPITAXY

Ünlü, Buse
Master of Science, Micro and Nanotechnology
Supervisor : Assoc. Prof. Dr. Selçuk Yerci
Co-Supervisor: Assist. Prof. Dr. Çiçek Boztuğ Yerci

September 2021, 99 pages

Germanium is compatible with CMOS technology and can be utilized for the development of an integrated laser on Si platforms. Nevertheless, it is a very inefficient light emitter owning to its indirect bandgap. On the other hand, the application of tensile strain reduces the split in between direct and indirect band edges of Ge, which in turn enhances its light emission efficiency, and converts it into a direct bandgap material.

In this thesis, firstly finite element model simulations are performed to determine the dimensions of the most efficient Ge microstructures providing the highest possible biaxial and uniaxial strain levels. Following that, Ge microstructures are fabricated, in which silicon nitride acts as a stressor layer on top and sides. Radio frequency magnetron sputtering, a straightforward, low-cost, and environmentally friendly method, is used for both amorphous Ge and the stressor film deposition processes. The liquid phase epitaxy technique is utilized to crystallize the amorphous Ge. It is demonstrated that one single annealing step converts the Ge to a single crystal and induces tensile stress to the nitride film, simultaneously. Moreover, the proceeding wet chemical etching steps promote the tensile strain induction in the Ge microstructures. The amount of strain can easily be tuned by changing the type and duration of wet etching processes. A uniaxial strain level of up to 3.5% has been

demonstrated by Raman and micro photoluminescence spectroscopy, and verified by FEM simulations. Results of this study pave the way to obtain infrared Ge lasers on Si chips by utilizing cost-efficient and easy-to-use deposition and crystallization techniques.

Keywords: Germanium, Strain Introduction, Stressor Layer, LPE, Luminescence

ÖZ

SIVI FAZ EPİTAKSİ YÖNTEMİYLE GELİŞTİRİLMİŞ ÇEKME GERİNİMLİ IŞIK SAÇAN GERMANYUM MİCROYAPILARININ TASARIMI VE ÜRETİMİ

Ünlü, Buse
Yüksek Lisans, Mikro ve Nanoteknoloji
Tez Yöneticisi: Doç. Dr. Selçuk Yerci
Ortak Tez Yöneticisi: Dr. Öğr. Üyesi Çiçek Boztuğ Yerci

Eylül 2021, 99 sayfa

Germanyum, CMOS teknolojisi ile uyumludur ve Si platformlarında entegre bir lazerin geliştirilmesinde kullanılabilir. Ancak, dolaylı bant yapısı gereği çok verimsiz bir ışık yayıcıdır. Diğer yandan, gerinim uygulanması, germanyumun direk ve dolaylı bantları arasındaki farkı düşürür, ki bu da karşılığında malzemenin ışık yayma verimliliğini artırır ve germanyumu direk bant aralığına sahip bir malzemeye dönüştürür.

Bu tezde ilk olarak, mümkün olan en yüksek çift eksenli ve tek eksenli gerinim seviyelerini veren, en verimli Ge mikroyapılarının boyutlarını belirlemek için sonlu elemanlar yöntemi simülasyonları gerçekleştirilmiştir. Bunu takiben, silisyum nitrürün üstte ve yanlarda bir stres katmanı görevi gördüğü Ge mikroyapıları üretilmiştir. Amorf Ge ve stresör filmlerinin biriktirme işlemleri, basit, düşük maliyetli ve çevre dostu bir yöntem olan radyo frekansı magnetron saçtırma ile yapılmıştır. Amorf formdaki Ge mikroyapılarının kristallenmesi için sıvı faz epitaksi tekniği kullanılmıştır. Tek bir tavlama adımının amorf germanyumu tek kristale dönüştürdüğü ve aynı zamanda silisyum nitrür filmde çekme stresini indüklediği gösterilmiştir. Dahası, devamındaki ıslak kimyasal aşındırma adımlarının tek kristal

Ge mikroyapılarında çekme gerinimi indüksiyonunu desteklediği gösterilmiştir. Bu ıslak aşındırma işlemlerinin türü ve süresi değiştirilerek gerinim miktarının kolayca ayarlanmıştır. %3,5'e kadar olan tek eksenli gerinim seviyesi Raman ve mikro fotolüminesans spektroskopisi ile gösterilmiş ve FEM simülasyonları ile doğrulanmıştır. Bu çalışmanın sonuçları, düşük maliyetli ve kullanımı kolay biriktirme ve kristalizasyon tekniklerini ile Si çipleri üzerinde kızılötesi Ge lazerleri elde etmenin yolunda önemli bir aşama sunmaktadır.

Anahtar Kelimeler: Germanyum, Gerinim Uygulama, Stres Katmanı, LPE, Lüminesans

Dedicated to my parents and my brother

ACKNOWLEDGMENTS

Firstly, I would like to thank my supervisor, Assoc. Prof. Dr. Selçuk Yerci, for providing me the opportunity to be a member of his APP research group and supporting me throughout my Master's study. I would like to express my deepest gratitude to my co-supervisor, Assist. Prof. Dr. Çiçek Boztuğ Yerci. I have an opportunity to continue my research in the light of her unique guidance. I have always been motivated by her constant support and encouragement. Working under her supervision has helped me become a better researcher.

I would also like to thank Prof. Dr. Raşit Turan and all GÜNAM members. They were always kind and helpful to me.

I am also very grateful to Arman Ayan and Can Özcan for sharing gently with me all their knowledge about germanium and fabrication processes. Their enthusiasm during the fabrication always motivated me.

I would like to thank Milad Ghasemi for being a great labmate working in harmony and Gence Bektaş for his never-ending support both technically and psychologically. My sincere thanks also go to Damla Koçak and Ceren Korkut for making Lab118 a workable place for me through their positive energies and support all the time. They always reminded me to take a break when I have been stressed out.

I am very thankful to all APP members for providing a pleasant time and enjoyable atmosphere throughout my Master's study, especially Eren Bahri Uzuner and Muhammet Mustafa ÇODUR, for their technical assistance whenever I needed it.

Finally, I would like to thank my beloved parents and my brother. They were always right next to me whenever I needed them. They always made me believe in myself and motivated me to get through hard times. This study would have been impossible without their moral support and endless love.

This thesis work was supported by the Scientific and Technical Research Council of Turkey (TUBITAK) under contract number 117F052.

TABLE OF CONTENTS

LIST OF TABLES

TABLES

LIST OF FIGURES

FIGURES

LIST OF ABBREVIATIONS

ABBREVIATIONS

Si	Silicon
ICs	Integrated Circuits
SOI	Silicon-on-Insulator
SiO_2	Silicon Dioxide
CMOS	Complementary-Metal-Oxide-Semiconductor
Ge	Germanium
MOSFETs	Metal Oxide Semiconductor Field Effect Transistors
LED	Light Emitting Diodes
Sn	Tin
VCA	Virtual Crystal Approximation
PL	Photoluminescence
InGaAs	Indium Gallium Arsenide
GaAs	Gallium Arsenide
NMs	Nanomembranes
Ni	Nickel
SiNx	Silicon Nitride
LW-NIR	Long-Wave Near Infrared
σ	Stress
ε	Strain

E	Young’s Elastic Modulus
ν	Poisson's Ratio
C_{11}, C_{12}	Elastic Stiffness Tensors
VB	Valence Band
HH	Heavy Hole
LH	Light Hole
DOS	Density of States
Ξ_d, Ξ_u	Dilation and Shear Deformations
a_c	Hydrostatic Deformation Potential
SO	Split-off
$E_{c\Gamma}$	Γ Valley Conduction Band Energy
E_{cL}	L Valley Conduction Band Energy
v	Wave Functions Of Valence Band
E_g	Bandgap Energy
m_c	Electron Effective Mass
Δ	Spin-Orbit Split-Off Energy
TE	Transverse Electric
TM	Transverse Magnetic
IB	Interband
FEM	Finite Element Method
L_{Bridge}	Bridge Length

$L_{Underetcing}$	Underetching Length
t_{SiNx}	Silicon Nitride Thickness
t_{Ge}	Germanium Thickness
w_{Ge}	Germanium Width
R_{Air}	Radius of Circular Air Gap
LPE	Liquid Phase Epitaxy
RMG	Rapid Melt Growth
RTA	Rapid Thermal Annealing
EBSD	Electron Backscattering Diffraction
PVD	Physical Vapor Deposition
RF	Radio-Frequency
N_2	Nitrogen
Ar	Argon
FTIR	Fourier Transform Infrared Spectroscopy
E_s	Young Modulus of Substrate
h_s	Thickness of Si
h_f	Thickness of film
R_o	Curvature Radius Before Deposition
R_f	Curvature Radius After Deposition
sccm	Standard Cubic Centimeter Per Minute
NH_4OH	Ammonium Hydroxide

H_2O_2	Hydrogen Peroxide
DI	Deionized
HF	Hydrofluoric Acid
CZ	Czochralski
DSP	Double Side Polished
IPA	Isopropyl Alcohol
PR	Photoresist
UV	Ultraviolet
BOE	Buffered Oxide Etchant
SEM	Scanning Electron Microscope
W	Watts
AFM	Atomic Force Microscopy
RMS	Root Mean Square
Rq	Roughness
H_3PO_4	Phosphoric Acid
H_2O	Deionized Water
KOH	Potassium Hydroxide
µ-PL	Micro Photoluminescence
M#	Mirror
P#	Pinhole

B#	Beam Splitter
L#	Lens
F#	Filter
O#	Objective
MB	Microbridge

CHAPTER 1

INTRODUCTION

This chapter briefly introduces the roles of Group-IV semiconductor elements in microelectronics and microphotonics, followed by the advantages and disadvantages of silicon technology. Then, how germanium takes the place of Si is explained.

1.1 Group-IV Semiconductors in Microelectronics and Microphotonics

In the early 2000s, silicon (Si), one of the group-IV semiconductor elements, left an outstanding mark on microelectronics in the wake of Si photonics. One of the main reasons was being the most abundant element on Earth after oxygen, which paves the way for manufacturing Si-based industrial devices with substantial cost saving [1]–[3]. Besides its high optical damage threshold, high third-order optical nonlinearities [3], and having a high thermal conductivity make silicon an exemplary substrate to eliminate the heat caused by the increasing number of transistors in the integrated circuits (ICs) [4].

Silicon-on-insulator (SOI) is another reason; losses originate from connection and reduce light propagation [5]. Hence, SOI gives a lead for planar waveguide circuits[3]. For micro-photonic chips, considerable refractive index difference in between silicon and silicon dioxide (SiO_2) by 2 provides strong optical confinement and decreases propagation losses. In this manner, SOI gives rise to the fabrication of nanometer-scale devices, and research in monolithic integrated circuit technology has dramatically increased [3], [5], [6]. Ultrasmall lattice filters in which the total length is smaller than 100 μm is an example of enabling a controllable channel-dropping with 10 nm bandwidth and 84 nm free spectral range [7]. Not only trouble on many-core memory bandwidth has been solved, but also fast switching and

energy-saving international communication have been achieved through photonic and electrical interconnections, respectively [8].

Nevertheless, these favorable properties of silicon are not feasible to meet the main call for light emission property. Several methods should be introduced to silicon for increasing the radiative recombination in between its bands. For instance, the band structure has been modified through alloys and hybrid integration models like SiGe [9], [10] and GaAs on Si [11], respectively; luminescence around 1550 nm has been exhibited via assisting of impurities like doping Si with erbium [12], [13]. However, those methods return as a cost increase [14]. Similarly, other complementary-metal-oxide-semiconductor (CMOS) compatible group-IV semiconductors also have indirect bandgap structures, which puts a barrier to be directly utilized as light sources [10], [15], [16]. In this regard, a slight energy difference of around 0.14 eV between the direct band and indirect band edges of germanium makes it a promising solution to overcome the optical limitations on indirect bandgap semiconductor materials [17]–[19] with cost efficiency in mass manufacturing.

1.1.1 Germanium Promising Material

Germanium (Ge) is a Group-IV semiconductor element located just below Si with group number 14 and the atomic number 32 [20], [21]. The density and atomic weight of Ge are 5.3234 g/cm^2 and 72.593, respectively at 25 °C [22]. It has a diamond-type crystal structure [22]–[24] that lattice constant is 0.5646185 nm for 99.999 % at the 30 °C temperature [22]. The phase of Ge changes from solid to liquid roughly at 1210.15 K [21], [25], [26]. The energy band structure of Ge is obtained considering spin-orbit interactions as shown in Fig. 1.1, and its eigenvalues are in Table 1.1 [27].

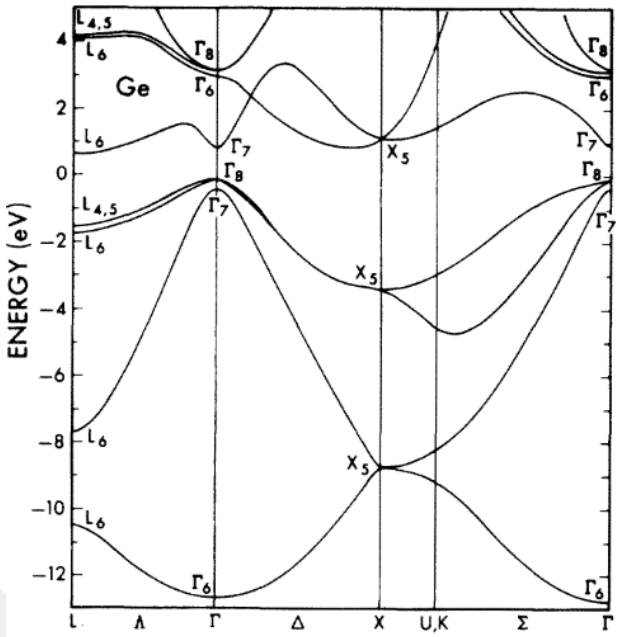

Figure 1.1 Germanium energy band structure [27].

Table 1.1 Germanium eigenvalues of Γ, L and X in eV.

Energy of Γ (eV)					
Γ_6^v	Γ_7^v	Γ_8^v	Γ_6^c	Γ_7^c	Γ_8^c
-12.66	-0.29	0.00	3.01	0.90	3.22
Energy of L (eV)					
L_6^v	L_6^v	L_6^v	$L_{4,5}^v$	L_6^c	L_6^c	$L_{4,5}^c$
-10.39	-7.61	-1.63	-1.43	0.76	4.16	4.25
Energy of X (eV)					
X_5^v		X_5^v		X_5^c	
-8.65		-3.29		1.16	

Ge's direct band gap energy is 0.800 eV, while 0.644 eV is indirect band gap energy [28]–[30]. Hence, germanium with a minimal band splitting of 0.136 eV between Γ

valley and L valley is a pseudo-direct gap semiconductor [31], not a non-convertible indirect material.

Historically, germanium in bulk form was used in the first transistors, which brought in Nobel Prize 1956 in Physics. Ge was a popular material in the solid-state manufacturing and integrated circuit industry [32], [33]. Even though the quality of oxidized Ge forms is incomparably low compared to thermally-growth silicon dioxide [33], having a weak passivation layer gives rise to dark current at undesirable levels [3]. In the following years, Ge and some materials with high dielectric constant (high k) became more pronounced in the gate terminal of metal oxide semiconductor field-effect transistors (MOSFETs) [33]. Germanium turned into a research subject again with not only the emergence of the high-k dielectrics but also higher electron mobility of Ge compared to Si by 2500 cm^2/V-s at 300 K [34], [35]. Limited drain current coming from the saturation velocity of Si was overcame with Ge and established greater refractive index contrast through Ge, further scaling of the MOSFETs was continued [36], and Ge-based MOSFET functionality was improved [37].

Above all, germanium meets the main requirements for the lasers having Si compatibility; because, as well as being compatible with CMOS technology on top of Si, electrical pumping of Ge is possible. Ge is increasingly in demand in the area of photonic band-gap engineering. Its band structure can be engineered to emit around the wavelength of 1.55 μm. Thereby, Ge on Si chips is widely utilized in fiber-optic communication [19]. The data transmission rate is rose appreciably. Additionally, this wavelength paves the way for usage in living space, such as fire detection, sensors measuring motion without harming human health [38] and sensing the biochemical species. Luminescence in the direct bandgap region is achieved; hence, germanium-based light-emitting diodes (LED) are fabricated [14], [39], [40]. Thanks to the shift in the active wavelength, detectors and sensors can be modified to work in several desired spectral regions. Ge can be used not only as a light absorber but also as an emitter in the telecom optical wavelength bands [41]. The expanded spectrum of absorption provides an opportunity for functional

improvement in CMOS via the integrated Ge in optoelectronic devices [42] as well as high-speed, high-efficient and low-cost Ge photodetectors [38], [43].

1.2 Thesis Outline

This thesis begins with Chapter 1, which briefly introduces Group-IV semiconductor elements and the motivation behind using Ge in microelectronics and microphotonics. In Chapter 2, how Ge band structure can be modified by three main methods to achieve a light emission is mentioned. Following that, the relation between strain and stress is given in Chapter 3, and the remarkable effects of strain on altering the Ge band structure are explained in detail. Chapter 4 covers the construction of the microstructures to be fabricated using COMSOL Multiphysics software, and strain distribution varying with the dimension of structures is investigated. Thus, geometrical optimization providing the highest possible biaxial and uniaxial strain is acquired, which is implemented in the design of the photolithography mask. Fabrication steps of both uniaxially and biaxially strained Ge microstructures are described in Chapter 5. Their characterization by EBSD, micro-Raman spectroscopy and micro photoluminescence (μ-PL) measurements is presented in Chapter 6, starting with explaining how the μ-PL system is constructed. The study is concluded in Chapter 7, including the possible future works.

1.3 Contributions

In this thesis, deposition of the films, namely germanium, silicon nitride and silicon dioxide, was performed by Milad Ghasemi using sputtering, and Hande Çiftpınar carried out thermal silicon oxide growth. Necati Işık analyzed stressor layers. He took surface profiles of the layers by Veeco Dektak 6M Profilometer and calculated the corresponding stress levels. Raman spectroscopy and EBSD measurements were performed in the METU Central Laboratory.

CHAPTER 2

ENERGY BAND ENGINEERING OF GERMANIUM

As stated in the previous chapter, the band structure of germanium can be modified to achieve radiative recombination, resulting in light emission. It is revealed that alloying Ge with tin (Sn) [44]–[51], tensile strain introduction [40], [46], [52]–[62] and n-type doping [14], [19], [63], [64] are the techniques increasing the efficiency to convert Ge band form indirect to direct one. In this chapter, these methods will be explained in detail.

2.1 Tin Incorporation

When Ge is incorporated with a sufficient amount of Sn atoms, its energy level of direct Γ valley falls below the indirect L valley. Thus, the direct transition is observed at k = 0 in Brillouin zone [45], [65]. The significant point here is the ratio of Sn atoms, which modifies the bandgap of the structure. As seen in Fig. 2.1, dependency of direct and indirect energy levels to the proportion value of x for $Ge_{1-x}Sn_x$ alloy can be estimated from the equations of $0.78x^2 - 2.00x + 0.87$ and $0.34x^2 - 0.91x + 0.71$, respectively through virtual crystal approximation (VCA) of tight-binding method; and also, energy gap formula of Γ valley equals $2.49x^2 - 3.76x + 0.88$ and L valley is $2.28x^2 - 2.85x + 0.72$ if the mixed-atom method is utilized [66].

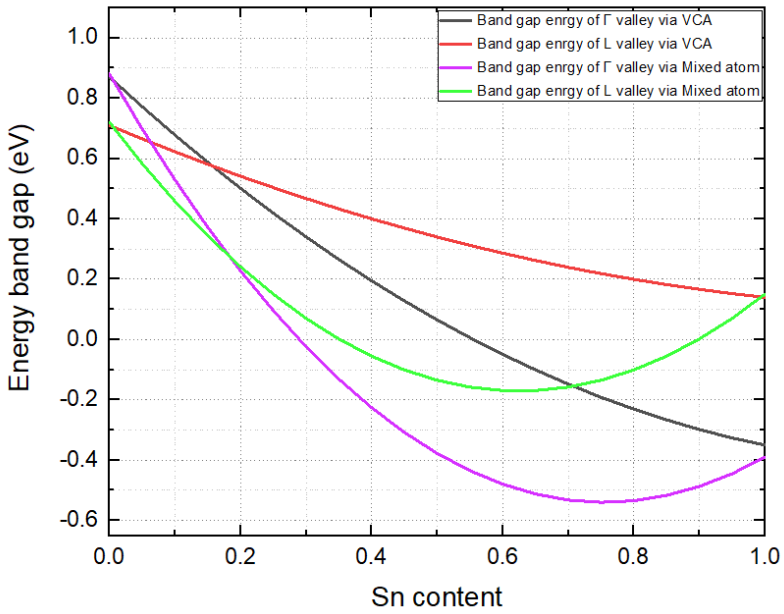

Figure 2.1 Bandgap energy value of $Ge_{1-x}Sn_x$ regarding Sn content calculated with VCA and Mixed atom methods [66].

The intersection points of the two graphs in Fig. 2.1 correspond to the required Sn amount for the Ge radiative emission. Hence, the percentages for that purpose are 17% and 15% through mixed-atom and VCA methods, respectively. Besides, Bandgap transition is experimentally demonstrated with an Sn ratio of 13% and 16% [48]. Photoluminescence (PL) measurement reports indicate the desired change in band structure [44], [45], [47], [48]

On the other hand, alloying Ge with Sn is not such an easy task. The main reasons are the high lattice mismatch between Ge and Sn by 0.0843 nm, stability problem of amorphous cubic structure Sn after 13°C [66], [67] and inefficient solid solubility [46], [68], which results in different surface concentration than its film alloy GeSn. In other words, segregation of surface material is observed [68]. As a result, GeSn film growth is very effort-driven and complicated.

2.2 Strain Induction

The spatial arrangement of Ge atoms can be disturbed by strain induction. This situation affects the band mechanism of Ge, similar to Sn incorporation. Required level of tensile strain leads to a decrease in energy for both direct and indirect levels where Γ valley goes down faster than the L valley [58], [69]. Thus, a change in band structure is acquired. Increasing the induction of tensile strain until Γ point is at a lower energy level than L makes Ge direct band gap material. As well as optical improvement, a climb in carrier mobility is also achieved in the presence of the strain [70].

There exist two types of strain formation depending on optical axes. Biaxial strain refers to strain existing in two perpendicular directions on a plane, and in the case of having strain in one optic axis, it is called uniaxial strain. The band structure is affected differently with respect to the strain types. Thus, the amount of tensile strain that needs to be applied for the direct transition of Ge varies accordingly. Studies have pointed out that tensile strain of 4.6% along the [100] direction [71]–[73] and biaxial strain about 2% in the (100) plane [28], [58], [73]–[76], where the band transition from indirect to direct is demonstrated in Fig. 2.2 [58], are necessitated for direct-band gap behavior of Ge.

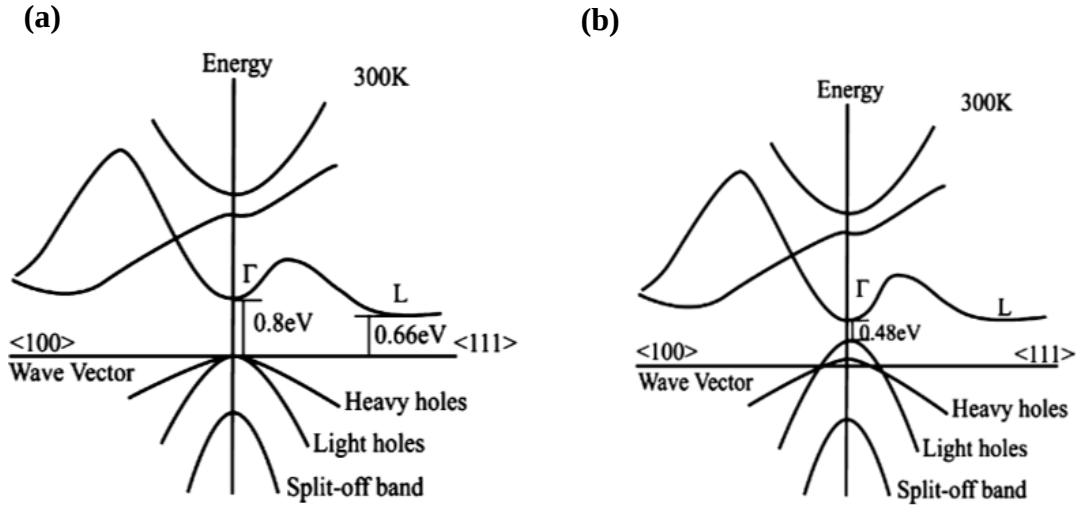

Figure 2.2 Effect of strain on Ge bandgap. (a) Unstrained Ge band structure. (b) Ge band structure after 1.9% biaxial tensile strain is induced on Ge, reduction in band energy from 0.66 eV to 0.48 eV [58].

Another important issue here is whether the strain is tensile or not. While tensile strain that results in elongation due to pulling apart decreases the difference between the direct Γ and indirect L valleys, the compressive strain which causes shortening own to squeezing increases the difference even more. Hence, to enhance the optical properties, tensilely strained Ge is desired [38]. In the light of studies, several fabrication designs have been investigated to form the tensile strain on Ge with a required amount, such as epitaxial growth [18], [77]–[81], mechanical-electrical inductions [82]–[84], and utilization of stressor layers [52], [54], [61], [62], [85]–[94].

2.2.1 Epitaxial Growth

One of the designs is epitaxial growth of Ge on top of an alloy, including group III-V elements. The idea here is to take advantage of the relation between strain and lattice mismatch, formulated as follows [95].

$$\text{Strain} = \frac{d_{hkl}(\text{substrate}) - d_{hkl}(\text{film})}{d_{hkl}(\text{film})}$$

In the formula above, d and *hkl* refer to space and atomic planes, respectively. While the positive result of the equation indicates tensile strain, negative is compressive strain [95].

Applying this method, 2.33% biaxially tensile strained Ge is achieved where Ge is sandwiched between InGaAs buffer layers on top of GaAs wafer [78]. This result is observed with a 40% concentration of indium and the lattice constant of $In_{0.40}Ga_{0.60}As$ is 0.5792 nm. Following that, with a more straightforward structure than Y. Huo *et al.'s,* nearly 2% strain is observed for 6 nm-thick Ge film with 0.30 In concentration; the importance of the interface stoichiometry on band modification is indicated in their study [80].

As well as InGaAs, GeSn is also studied. Through curved layer effect, fabricated Ge-GeSn structure results in uniaxial tensile strain in the direction of (110). The transition of Ge from direct to indirect band material has been verified by the peak position shift in photoluminescence (PL) measurements [81].

However, heteroepitaxial growth can be utilized if the film is thin considering the lattice mismatch between the layers because the film thickness is directly proportional to the dislocation formation [96]. Thus, the critical thickness should be taken into account [95].

2.2.2 Mechanical-Electrical Inductions

Another method to induce strain is the external application of stress after sample fabrication; so, the property of strain tunability is the primary acquisition in using this technique. The gap between energy bands declines with tensile stress [97].

In the study of J. Greil *et al.*, tensile stress is acquired through a 3-point bending design; electrical and optical properties of Ge are controlled with varying the amount of applied tensile strain [82].

J. R. Sanchez-Perez *et al.* offers such a structure in Fig. 2.3, causing mechanical strain to Ge in the biaxial direction [98]. For this purpose, Ge nanomembranes (NMs) are transferred onto a polyimide film, after which a gas with a very high level of pressure is supplied into the system. Thus, Ge NMs are mechanically stretched. Controllable strain with respect to applied gas pressure level is reported through Raman spectroscopy. Also, photoluminescence measurements are performed to observe the change in band energy of Ge at room temperature.

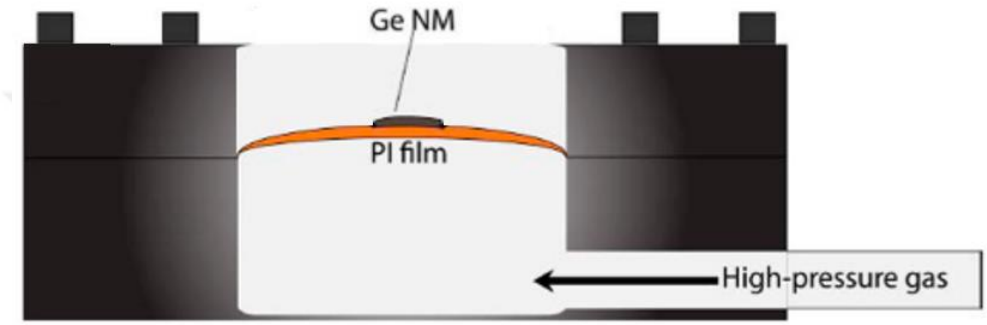

Figure 2.3 Illustration of strained Ge NM on a polyimide film via the application of high-level gas pressure [98].

Electrical force is claimed to be a functional candidate for strain formation on Ge [84]. Based on this idea, voltage is induced in between Ge and bottom layer of Si; attraction of accumulated charges leads to bending of Ge microstructure as seen in Fig. 2.4. Therefore, strain resulting from bending changes as a function of the applied voltage level. Simulation results reveal the possibility of >4% tensile uniaxial strain by increasing the applied voltage amount.

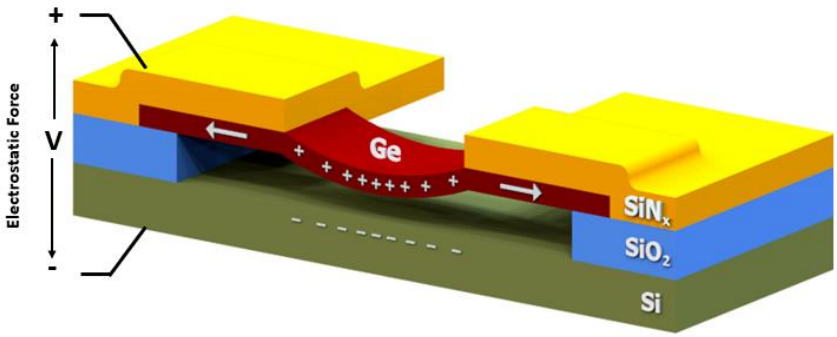

Figure 2.4 Cross-sectional sketch of A. Ayan *et al.'s* design for strain induction. Electrostatic force application and bending of Ge nanobeam are demonstrated [84].

2.2.3 Stressor Layers

Besides those techniques, strain formation is also observed via the use of stressor layers. Through a stress layer deposition, the atomic symmetry of the substrate is irritated; in other words, the strain has been transferred [99]. Strain induction goes up by thicker stressor layers [93]. In accordance with this purpose, nickel (Ni) [100], tungsten [93], [94] and silicon nitride (SiN_x) [52], [54], [61], [85]–[91] are reported materials.

Tungsten with a compressive stress about $4x10^9$ Pa enables an appreciable amount of tensile strain transfer via the deposition of tungsten under the suspended Ge structure [93]. It is stated that the energy of direct bandgap is declined by 0.1eV through the stressor tungsten layer.

Silicon nitride with the property of CMOS compatibility puts the other stressors in the shade. SiN_x with several patterns and deposition techniques/conditions has been investigated. Thus, several distinctive designs for strain engineering are reported. Silicon nitride is deposited just top surface of Ge [86], [89], [91], and covers also sidewalls of Ge [52], [54], [61], [88] which offers a possibility of current injection mechanism [85].

When germanium is encapsulated with SiN_x layer [52], [90], direct band emission is achieved [90]. In the study of M. El Kurdi *et al.*, Ge is patterned like a disk with 6 μm and 9 μm diameters covered with SiN_x stressor layer is shown in Fig. 2.5. Γ valley is acquired as in the same energy level with L valley for 9 μm Ge microdisk; even smaller energy level of Γ point is reported in the case of reducing the diameter by 3 μm. Ge disks with 6 μm and 9 μm diameters offer biaxial tensile strain of 1.75% and 1.67%, respectively, which is demonstrated as sufficient biaxial strain values to convert the indirect energy band of Ge to direct one.

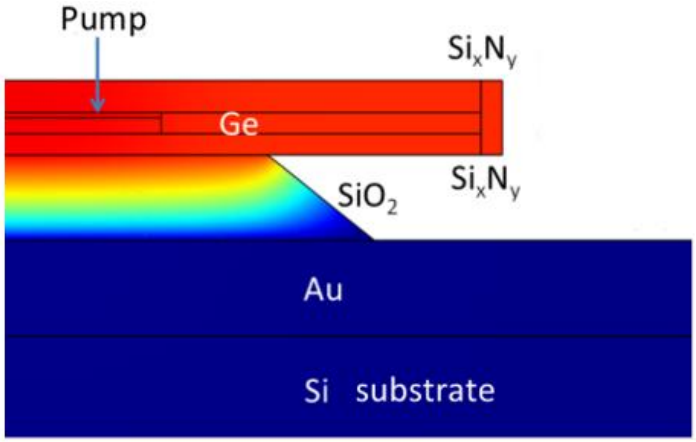

Figure 2.5 Demonstration of Ge microdisk encapsulated by silicon nitride [90].

2.3 n-type Doping

Doping has a different effect on the band structure of germanium in comparison with Sn incorporation and strain induction. L valley of the conduction band is filled with n-type impurities; in other words, the indirect conduction band is doped with a certain level of electrons until compensation of energy difference in between valleys. Thereby, unfilled band levels of Γ and L points become equal to each other so that optically or electrically injected carriers are forced to recombine with holes of direct Γ valley radiatively [14], [19], [63], [101], [102]. Direct transition can also be boosted through the continuation of carrier injection because, in this case, inter-band scattering occurs from L valley to Γ valley [69].

Direct growth of Ge on top of Si without any modification is not a feasible method owning to the lattice constant mismatch in between Si (~5.43 Å) and Ge (~5.65 Å) by roughly 4% [30], [103], which obstructs the phonon transportation between the interfaces [104], [105], and reorganization of atoms towards the Si/Ge border increases complexity [104]. Deterioration of atomic order is directly proportional to the lattice mismatch. On the other hand, just by adjusting the deposition temperature during the growth of Ge on Si, the intended growth is possible, which in turn, thermal expansion between the two layers brings in approximately 0.2% tensile strain [14]. Thereby, the future decreased gap of bulk Ge (136 meV) via the existence of the strain can be compensated (in Fig. 2.3) by less amount of electron carriers.

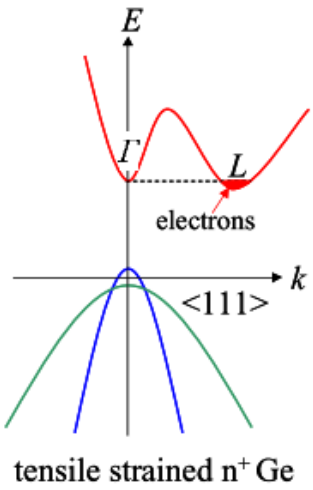

Figure 2.6 Illustration of tensile strained Ge band structure filled L valley through n-type doping [19].

While Ge has a tensile strain of 0.25%, $7.6\text{x}10^{-19}$ cm^{-3} electron concentration is reported as the required amount to obtain roughly 400 cm^{-1} optical gain Ge-based lasers [19]. When strained Ge is optically pumped with nearly 7 kW/cm^2, an optical gain of 56 cm^{-1} is obtained with $1.0\text{x}10^{-19}$ cm^{-3} doping density [31].

Furthermore, the combination of bandgap engineering methods is an effective technique to be applied. The reason for that is averting shrinkage of bandgap seen after exceeding tensile strain of 2%, which results in not 0.8 eV, but 0.5 eV bandgap

difference. Therefore, the energy level of L valley is filled by electrons, n-type doping, till being in same energy level with Γ valley where Ge is 0.25% tensilely strained. Such, through the combination of strain introduction and n-type doping methods, monolithic integration of Ge on Si has a potential to achieve an optical gain in the long-wave (LW-NIR) region with the wavelength of 1550 nm [14], [19].

However, parasitic absorption becomes more pronounced with increasing doping level; lasing is obstructed in the case of carrier density around $10^{-20}\,\mathrm{cm}^{-3}$ [106]. Furthermore, the quality of crystal decreases with increasing the carrier injection [102], and high threshold current density arising from high carrier density obstructs Ge laser to be used practically. Even though the number of carriers has been increased with doping, excessive doping causes absorption of free carriers [82]. As a result, doping alone without being supported by any other techniques is not a sensible method.

CHAPTER 3

STRAIN MODIFICATION ON GERMANIUM ELECTRONIC BAND STRUCTURE

As aforementioned in the previous chapters, the band structure of germanium is in the form of an indirect band. Nevertheless, various applications convert Ge into direct band-gap material by closing the energy separation between the direct valley and indirect valley and making the energy level of the direct band even smaller than the indirect one. Strain induction is a promising method to meet this demand, as the energy band structure is corrupted in the presence of strain. The underlying reason is that strain alters the lattice constant of material [70]. When the amount of strain applied to Ge is sufficient, around 4.6% uniaxial strain in the <100> direction and in the range of 1.6% and 2.0% biaxial strain, Ge can be used as a light emitter. To what extent the strain affects Ge band structure is explained in this chapter.

3.1 A Brief Introduction to Strain-Stress

Strain is the ratio of change in length (i.e., deformation) to the material's original length. Positive strain means that the resulting strain is the tensile strain; otherwise, it is compressive. Stress (σ) is the quantity of the force applied per unit area. A linear relationship exists between strain and stress, which is explained by Hooke's Law ($\sigma = E\,\varepsilon$) varying according to the material's property called Young's Elastic Modulus (E), which is valid for a small amount of strain. Even though stress is implemented in one coordinate axis, all three axes, x, y and z, feel the strain. While the material extends longitudinally, at the same time, it shrinks in the other two directions. The proportion of lateral strain to longitudinal one is denominated by Poisson's ratio (ν). As a result, strain with respect to stress in each direction is calculated following [97].

$$\varepsilon_{xx} = \frac{\sigma_{xx}}{E} - \frac{\nu}{E}(\sigma_{yy} + \sigma_{zz}) \quad (3.1)$$

$$\varepsilon_{yy} = \frac{\sigma_{yy}}{E} - \frac{\nu}{E}(\sigma_{xx} + \sigma_{zz}) \quad (3.2)$$

$$\varepsilon_{zz} = \frac{\sigma_{zz}}{E} - \frac{\nu}{E}(\sigma_{yy} + \sigma_{xx}) \quad (3.3)$$

For lattice-mismatched biaxial strain (Fig.3.1), in which stress is exercised in the z-axis direction to (001) surface [107],

$$\varepsilon_{xx} = \varepsilon_{yy} = \frac{a_o - a}{a} = -\frac{1}{2}\frac{C_{11}}{C_{12}}\varepsilon_{zz} \quad (3.4)$$

$$\varepsilon_{xy} = \varepsilon_{zy} = \varepsilon_{zx} = 0 \quad (3.5)$$

where C_{11} and C_{12} are the elastic stiffness tensors.

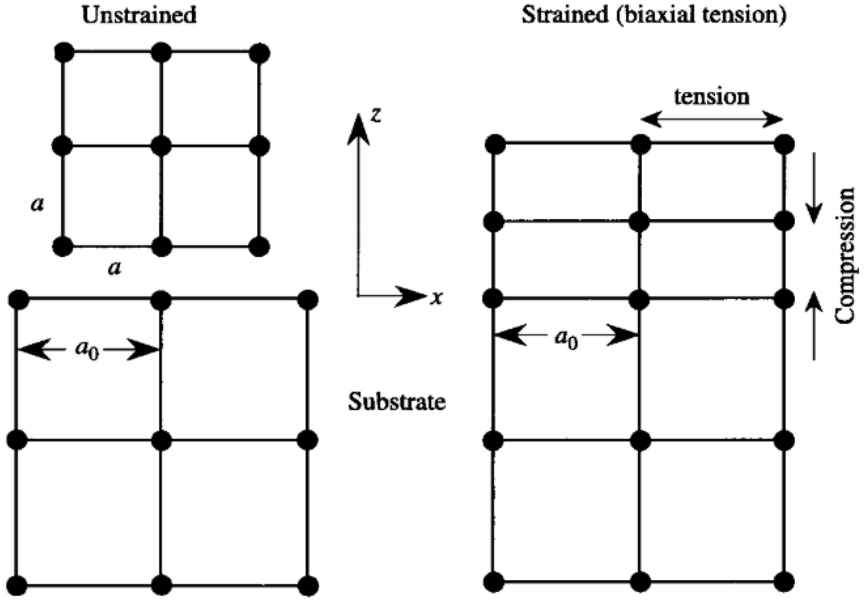

Figure 3.1 Biaxial strain formation in the presence of lattice mismatch in between two layers (lattice constants of substrate and film a_o and a, respectively) [108].

If the stress is externally applied,

$$\varepsilon_{xx} = \varepsilon_{yy} = -\frac{C_{12}}{{C_{11}}^2 + C_{11}C_{12} - {C_{12}}^2}\sigma_z \quad (3.6)$$

$$\varepsilon_{zz} = \frac{C_{11}+C_{22}}{{C_{11}}^2+C_{11}C_{12}-{C_{12}}^2}\sigma_z \tag{3.7}$$

Strain can be divided into three as hydrostatic strain and two types of shear strain [58], [70], [97]. While hydrostatic strain (isotropic strain) refers to volume change, the shear strain applied to the surface in parallel (uniaxial or biaxial strains) refers to the change in the shape of the material. The matrix representations of strain are given as follows [97].

$$\text{Hydrostatic Strain} = \frac{1}{3}\begin{pmatrix} \varepsilon_{xx}+\varepsilon_{yy}+\varepsilon_{zz} & 0 & 0 \\ 0 & \varepsilon_{xx}+\varepsilon_{yy}+\varepsilon_{zz} & 0 \\ 0 & 0 & \varepsilon_{xx}+\varepsilon_{yy}+\varepsilon_{zz} \end{pmatrix} \tag{3.8}$$

$$\text{Shear Strain} = \frac{1}{3}\begin{pmatrix} 2\varepsilon_{xx}-\varepsilon_{yy}-\varepsilon_{zz} & 0 & 0 \\ 0 & 2\varepsilon_{yy}-\varepsilon_{xx}-\varepsilon_{zz} & 0 \\ 0 & 0 & 2\varepsilon_{zz}-\varepsilon_{xx}-\varepsilon_{yy} \end{pmatrix} + \begin{pmatrix} 0 & \varepsilon_{xy} & \varepsilon_{xz} \\ \varepsilon_{yx} & 0 & \varepsilon_{yz} \\ \varepsilon_{zx} & \varepsilon_{zy} & 0 \end{pmatrix} \tag{3.9}$$

In Eq. (3.9), where all nondiagonal entries are zero, the shear strain component is responsible for the length change, such as observed in the case of stress implementation along the <100> direction. Other shear strain corresponds to rotational effects in which stress is only in the direction of <110> or <111>. The material's band structure subjected to strain exhibits several characteristics by the existing strain types [58]. To demonstrate, unlike the energy band splitting effect of shear strain, just a shift in energy bandgap is observed with hydrostatic strain [70]. In addition to this, as stated in chapter 2, the level of strain resulting in direct optical transition varies with respect to the direction of strain being uniaxial or biaxial.

3.2 Change in Band-Edge Energies via Strain

Shear strain deforms the periodicity of the arrangement of the atoms in a crystal, which in turn causes degenerate bands splitting, lifting and band wrapping [70], [97]. In the existence of tensile strain (not including the (111) in-plane), Γ valley comes to smaller energies faster than L valley [37]. Thus, at the sufficiently high strain, the energy level of conduction band for electron-hole recombination is no longer L point but becomes Γ point, and the valence bands split off as seen in Fig. 3.2. The upper valence band is the 1st valence band (1st VB), and the other band is the 2nd valence band (2nd VB). In uniaxial tensile strain, these bands indicate light hole (LH) and heavy hole (HH), respectively. The ratio of HH and LH masses is 0.33/0.043 [109]. Thus, strain results in a sharp decrease in density of states (DOS) effective mass by pulling up the 1st VB [110], which offers an increase in optical gain [19]. The movement of Γ valley (downward) and valence bands (upward) [58] further reduces the band gap via increasing strain, which enhances the direct band transition.

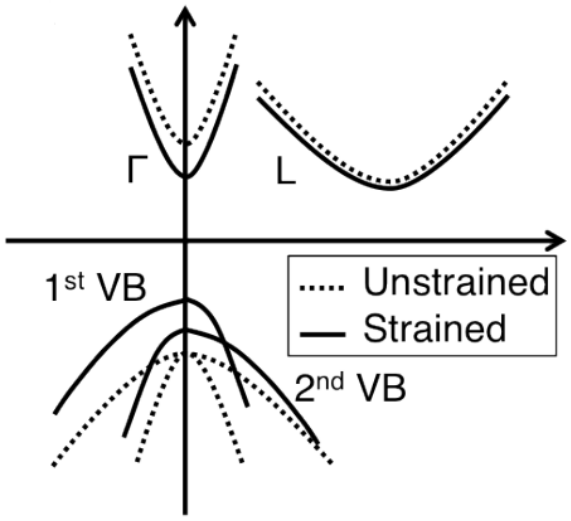

Figure 3.2 Movement of Ge band energies with the effect of tensile strain [95] 1st VB represents light holes (LH), and 2nd VB is heavy holes (HH).

In the conduction band of Ge, strain leads to a shift in energy. This effect is stated by some researchers with deformation potentials [111]. Hydrostatic deformation taking place in the conduction band [112] with taken non-diagonal strain tensors as zero is

$$\Delta E_{hydrostatic\ def.} = \left(\Xi_d + \frac{1}{3}\Xi_u\right)\left[\vec{1}:\left(\varepsilon_{xx} + \varepsilon_{yy} + \varepsilon_{zz}\right)\right] \tag{3.10}$$

where $\vec{1}$ denotes unit tensor, and Ξ_d (Ξ_u) indicates the dilation (shear) deformation constant, and for Ge, the expression $\Xi_d + \frac{1}{3}\Xi_u$ equals to 2.34 eV [18].

If the stress is implemented in the <110> and <111> directions, shear deformation is observed as follows [112], [113].

$$\Delta E_{shear\ def.,<110>} = \left|\frac{1}{6}S_{44}\Xi_u\sigma_{<110>}\right| \tag{3.11}$$

$$\Delta E_{shear\ def.,<111>} = \begin{cases} \frac{1}{3}S_{44}\Xi_u\sigma_{<111>} \\ -\frac{1}{9}S_{44}\Xi_u\sigma_{<111>} \end{cases} \tag{3.12}$$

where S_{44} is compliance constant, and Ξ_u is 16.2±0.4 eV [113].

In the light of all the mathematical expressions [108], [111]–[113], the following inference for the change in Γ valley and L valley of conduction band due to strain has been made [58] with taken non-diagonal strain tensors as zero as

$$\Delta E_\Gamma = E_\Gamma - E_{\Gamma,\mathrm{unstrained}} = a_\mathrm{c}\left(\varepsilon_{xx} + \varepsilon_{yy} + \varepsilon_{zz}\right) \tag{3.13}$$

$$\Delta E_\mathrm{L} = E_\mathrm{L} - E_{\mathrm{L,unstrained}} = \left(\Xi_d + \frac{1}{3}\Xi_u\right)\left(\varepsilon_{xx} + \varepsilon_{yy} + \varepsilon_{zz}\right) \tag{3.14}$$

where a_c is hydrostatic deformation potential and equals -8.24 eV by the theory of model solid [72].

In the valence band of Ge, spin-orbit split-off and/or shear strains are the reasons for electronic bands splitting [72]. Bir-Pikus and Luttinger-Kohn Hamiltonian methods are stated to explain the split-off reaction [107]. Hence, band-edge energies

of heavy holes (HH), light holes (LH) and spin-orbit split-off (SO) are given in ref 107 and are also referred to with the addition of unstrained values in ref 58 as

$$E_{\mathrm{HH}} = E_{\mathrm{HH,unstrained}} - P_\varepsilon - Q_\varepsilon \tag{3.15}$$

$$E_{\mathrm{LH}} = E_{\mathrm{LH,unstrained}} - P_\varepsilon + \frac{1}{2}\left(Q_\varepsilon - \Delta + \sqrt{\Delta^2 + 2\Delta Q_\varepsilon + 9{Q_\varepsilon}^2}\right) \tag{3.16}$$

$$E_{\mathrm{SO}} = E_{\mathrm{SO,unstrained}} - P_\varepsilon + \frac{1}{2}\left(Q_\varepsilon - \Delta - \sqrt{\Delta^2 + 2\Delta Q_\varepsilon + 9{Q_\varepsilon}^2}\right) \tag{3.17}$$

where Δ represents the spin-orbit split-off energy, P_ε and Q_ε are

$$P_\varepsilon = -a_v\left(\varepsilon_{xx} + \varepsilon_{yy} + \varepsilon_{zz}\right) \tag{3.18}$$

$$Q_\varepsilon = -\frac{b}{2}\left(\varepsilon_{xx} + \varepsilon_{yy} - 2\varepsilon_{zz}\right) \tag{3.19}$$

where a_v is hydrostatic deformation potential (1.24 eV for Ge [72]) and b is shear deformation potential (-2.16 eV for Ge [114]), which are in general Bir-Pikus deformation potentials. Also, here non-diagonal strain tensors are taken as zero.

As a result of Eqs. from 3.13 to 3.16 with the inclusion of Eqs. 3.4 and 3.5, for biaxial strain along the {100} plane, conduction band energies [Γ point ($E_{c\Gamma}$), and L point ($E_{c\mathrm{L}}$)] and the valence band-edge energies of light holes (E_{lh}) and heavy holes (E_{hh}) are plotted [58] in Fig. 3.3. Here, the required minimum biaxial-strain level of %1.9 where $E_{c\Gamma}$ equals to $E_{c\mathrm{L}}$ is clearly observed.

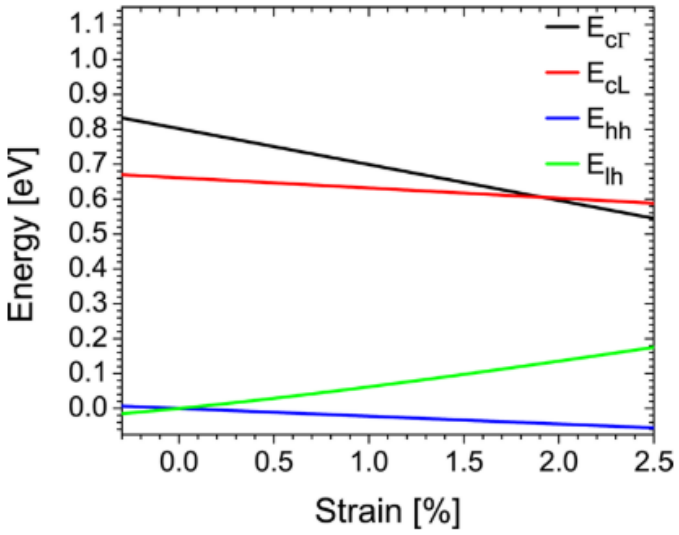

Figure 3.3 The change in energy of valence bands and conduction bands with respect to exercised {100} biaxial strain [58].

3.2.1 Strain-Dependent Energy Band Transitions

The emission resulting from the transition between conduction and valence band edges is associated with light polarization and can be explained by dipole moments [115]. For this purpose, in the study of T. Chong and C. Fonstad, matrix element is used, and four-wave functions of the valence band (v_1, v_2, v_3, v_4) are involved as

For TE polarization through the direction of x-axis or y-axis,

$$M^2{}_{cvi,x(or\ y)} = \begin{cases} \frac{{M_o}^2}{2} & ,\ i = 1,2 \\ \frac{{M_o}^2}{6} & ,\ i = 3,4 \end{cases} \tag{3.20}$$

For TM polarization through the direction of the z-axis,

$$M^2{}_{cvi,z} = \begin{cases} 0 & ,\ i = 1,2 \\ \frac{2{M_o}^2}{3} & ,\ i = 3,4 \end{cases} \tag{3.21}$$

M_o depends on bandgap energy of unstrained material (E_g), electron effective mass (m_c) and spin-orbit split-off energy (Δ) as

$$M_o{}^2 = \frac{3\hbar^2 e^2 E_g\,(\Delta+E_g)}{2m_c E_{cv}{}^2(3E_g+2\Delta)} \tag{3.22}$$

where e is the electron charge, and the energy difference between the conduction band and valence band is represented by $E_{cv} = E_c - E_v$.

Transverse electric (TE) and transverse magnetic (TM) are the modes of electromagnetic waveguides where electric field and magnetic field components are transverse to the propagation direction, respectively. In short, perpendicular polarized light is called TE, and parallel polarized light is TM. In the Eqs. 3.20 and 3.21, v_1 and v_2 refer to heavy holes where light holes are denoted by v_3 and v_4. Hence, it is concluded that the emission due to the transition from conduction band Γ point to heavy holes is only subjected to the TE-polarized light. In contrast, the conduction band Γ point to light holes transition involves both modes, more predominantly TM-polarized light [115]. In other words, TM polarized transition in between Γ point and the light hole is higher than TE polarized case [28], [76]. In the presence of uniaxial tensile strain, because LH is closer to Γ valley than HH, the light emission predominantly results from Γ→LH transition and is mainly TM-polarized [58].

Consequently, the transition energies in between conduction bands and top two valence band edges, which are called interband (IB) transitions (Γ→VB1, VB2 and L→VB1, VB2), and in between valence band energies, which are called intervalence band (IVB) transitions from the top valence band edges to the split-off band (VB1, VB2→VB3), are plotted in Fig. 3.4 with respect to (001) biaxial tensile strain and [100] uniaxial tensile strain [116]. The transitions from Γ to VB1 and VB2 refer to the direct transitions of cΓ→LH and cΓ→HH while the indirect band energies are represented by L valley transitions of cL→LH and cL→HH [98], [117], [118].

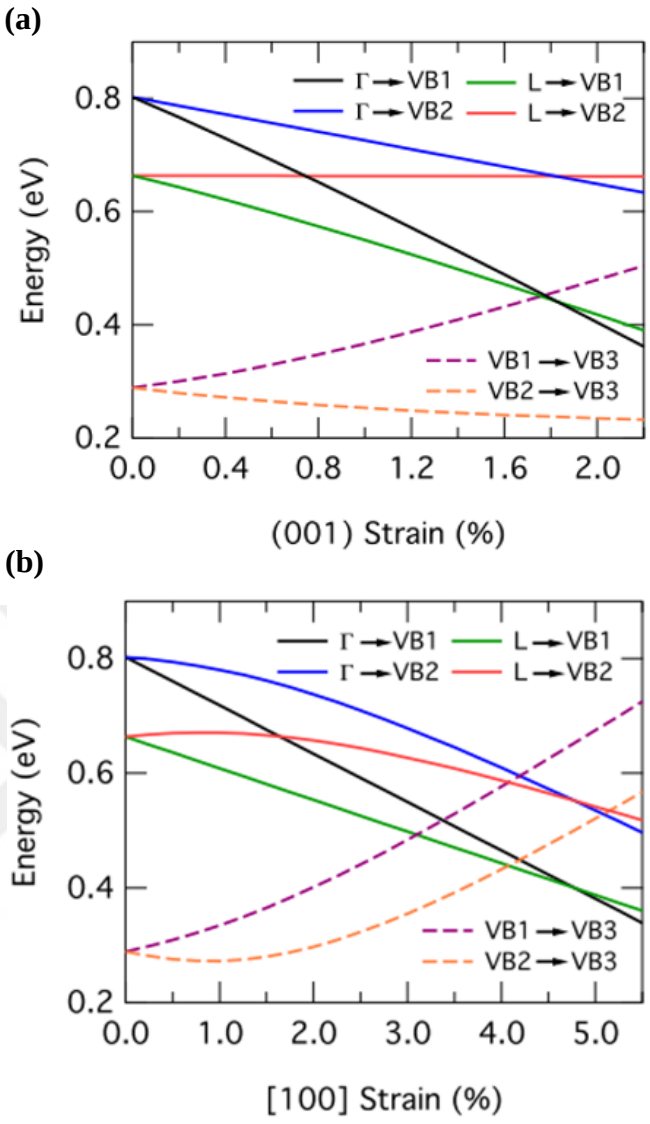

Figure 3.4 Transitions in between Ge band energies for (a) (100) biaxial strain and (b) [100] uniaxial tensile strain, solid lines (dashed lines) indicate interband (intervalence band) transitions [116].

CHAPTER 4

FINITE ELEMENT METHOD (FEM) SIMULATIONS OF STRAIN DISTRIBUTION

The finite element method (FEM) is performed using COMSOL Multiphysics software with a solid mechanics module to determine the dimension of the most efficient Ge microstructures, providing the highest possible biaxial and uniaxial strain levels. Strain distribution on Ge microstructures is analyzed in this chapter. In the light of strain results, a photolithography mask to be used to fabricate the structures is designed considering the simulation dimensions.

4.1 Geometrical Optimization for Uniaxial Tensile-Strained Ge Microstructures

A schematic of Ge microstructure to induce uniaxial tensile strain is shown in Fig. 4.1(a). Here, silicon is the substrate of the structure, where silicon dioxide is an insulator layer underlying the Ge microstructure, and silicon nitride is a stressor film covering Ge's top and sidewalls. Initial tensile stress to SiNx is defined as 1 GPa. The top and bottom layers of Si are assigned as fix constraints. Meshing is constructed considering the dimensions of individual geometries such that while element size for Ge is extremely fine (due to having the smallest size compared to others), it is set as extra fine for SiNx and SiO_2. Besides, the entire geometry is meshed by a free tetrahedral node where the size is extra fine.

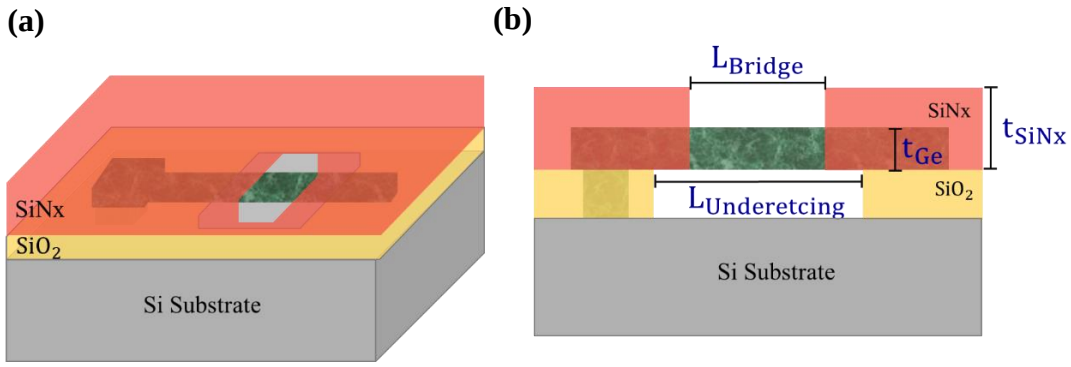

Figure 4.1 Illustration of the designed structure for uniaxial tensile strain induction to Ge microstructure (a) 3-dimensional view and (b) cross-sectional view with parametric denotations.

As observed from the following results, strain level markedly varies with depth and width of the Ge, length of bridge (L_{Bridge}), length of underetching ($L_{Underetcing}$), thicknesses of SiNx (t_{SiNx}) and Ge (t_{Ge}) denoted in Fig. 4.1(b). The width and length of the whole structure are kept constant as 50 µm and 200 µm, respectively, where Si thickness is 300 µm, oxide thickness is 81 nm, and Ge length is 150 µm. First of all, the effect of Ge width (w_{Ge}) on strain level is analyzed. Strain decreases by increasing Ge width ,as indicated in Fig. 4.2, where t_{SiNx} = 700 nm, t_{Ge} = 400 nm, L_{Bridge}= 50 µm and $L_{Underetcing}$= 100 µm. Therefore, Ge width is set as small as possible (i.e., 2 µm) by considering the fabrication precision.

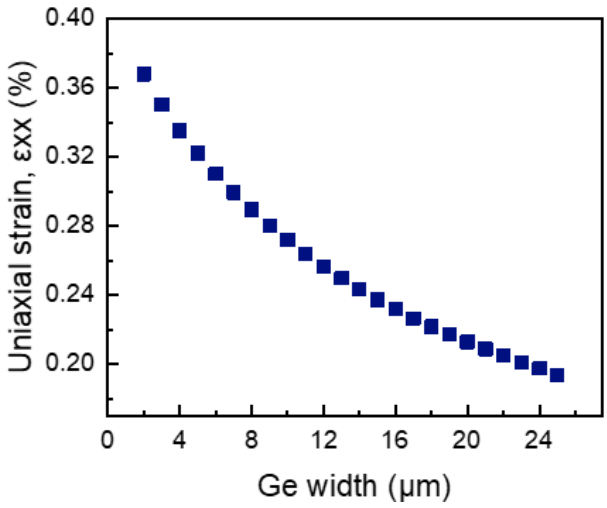

Figure 4.2 Change in uniaxial strain with respect to Ge width.

L_{Bridge} followed by $L_{Underetcing}$ are varied as given in Fig. 4.3. While uniaxial strain diminishes with increasing the length of the bridge in Fig. 4.3(a), it climbs up in almost direct proportion to underetching length in Fig. 4.3(b). The bridge length is set as 4 μm during the investigation of underetching length.

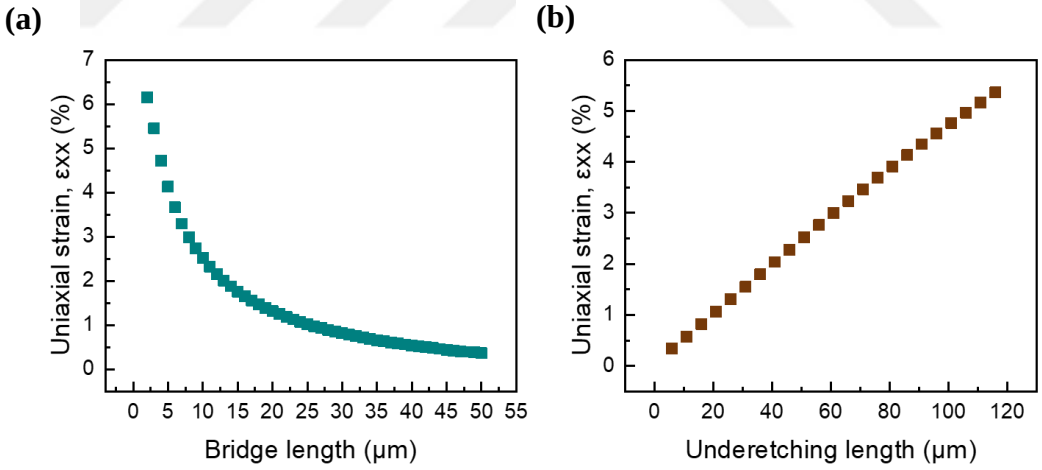

Figure 4.3 Change in uniaxial strain with respect to (a) bridge length and (b) underetching length.

Following that, how the thicknesses of Ge and SiNx affect the strain level is analyzed where the lengths of bridge and underetching are 4 μm and 116 μm, respectively. Ge

thickness should be reduced to increase the uniaxial strain while SiNx thickness should be increased, as shown in Fig. 4.4(a) and Fig. 4.4(b), respectively.

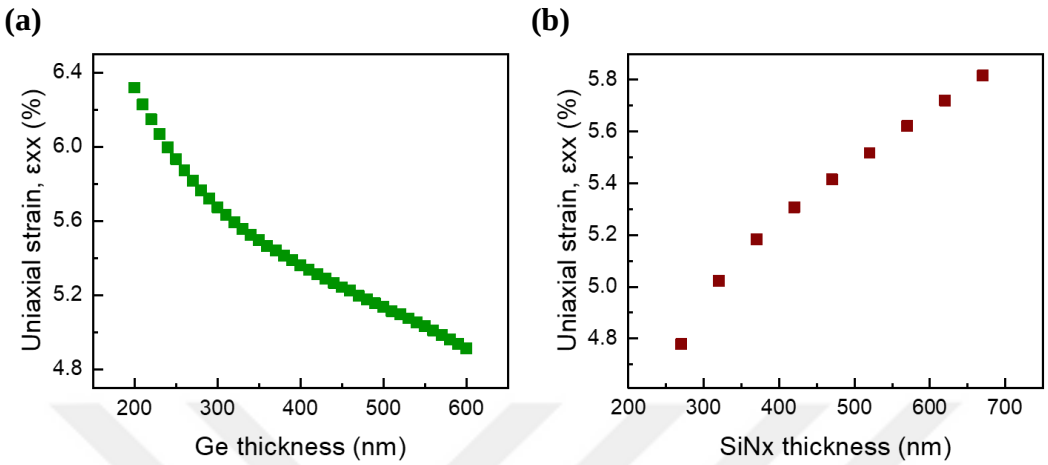

Figure 4.4 Change in uniaxial strain with respect to the thicknesses of (a) Ge and (b) SiNx layer with t_{Ge} = 260 nm.

The constructed exemplary 3D model by COMSOL is given in Fig. 4.5(a), where the parameters are set as different than used in the simulations for easily imagining the whole structure where $L_{Underetcing}$= 10 µm and t_{SiO2}= 0.81 µm. Figure 5.5(b) shows the top view of the structure with w_{Ge} = 2 µm, t_{SiNx} = 700 nm, t_{Ge} = 260 nm, L_{Bridge}= 4 µm and $L_{Underetcing}$= 116 µm, indicating the strain distribution on Ge microstructure by a color legend, and strain line profile along the bridge resulting in the maximum strain as 5.87% is obtained in the middle of the Ge bridge.

Briefly, strain can be increased by decreasing the width and thickness of Ge, and the length of the bridge, increasing the SiNx thickness and the underetching length.

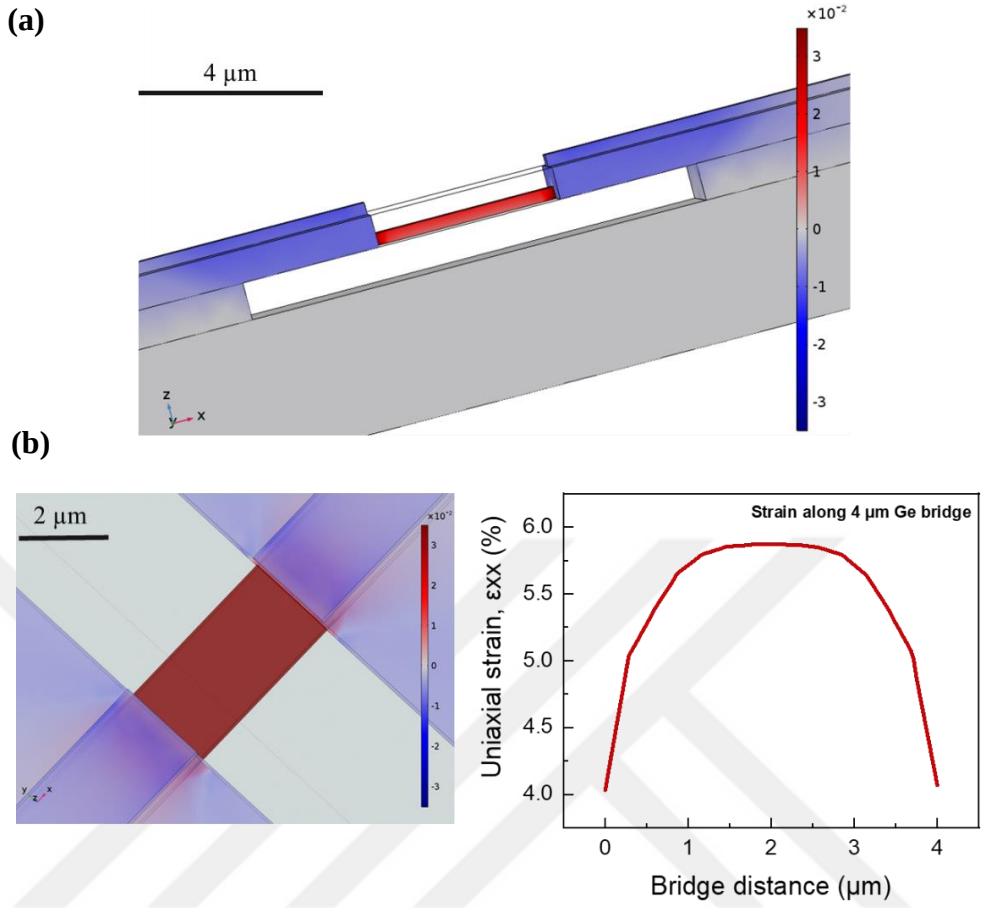

Figure 4.5 Localized strain distribution in constructed 3D COMSOL model of Ge microstructure (a) side view for imagining the whole structure with $L_{Underetcing}$= 10 µm and t_{SiO2}= 0.81 µm, (b) top view of 5.87% uniaxial strained Ge and strain profile along the bridge with w_{Ge} = 2 µm, t_{SiNx} = 700 nm, t_{Ge} = 260 nm, L_{Bridge}= 4 µm and $L_{Underetcing}$= 116 µm.

4.2 Geometrical Optimization for Biaxial Tensile-Strained Ge Microstructures

Y-shaped Ge (120° angled three tails) is designed (in Fig. 4.6) to obtain a biaxial tensile-strained Ge microstructure, for which SiO_2 (the bottom layer of Ge) is etched in a square shape to suspend Ge, and also 1 GPa stressor SiNx layer is etched in the shape of a circle for transferring strain to the mid-region of the Ge where the three

tails meet. Fix constraint domains and meshing element sizes are defined as the same as the previous simulations performed for uniaxial tensile-strained Ge microstructure. Ge width is kept at the smallest value (2µm) as concluded from the previous structure. Thicknesses of Si, SiO_2, SiNx and Ge are set as 3 µm, 81 nm, 700 nm and 260 nm where the area of the total square-shaped structure is 110 μm^2.

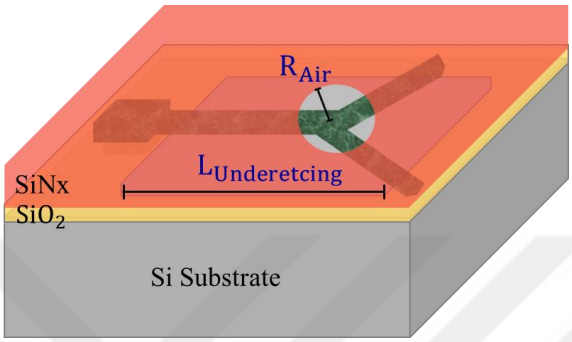

Figure 4.6 Illustration of the designed 3-dimensional model for biaxial tensile strain induction to Ge microstructure.

Firstly, the effect of air in circular shape where Ge is not covered with SiNx is investigated, resulting in strain change with respect to the radius of the circular air gap (R_{Air}) is given in Fig. 4.7(a) where $L_{Underetcing}$ = 65 µm. It is obtained that strain in the middle region of Ge declines by widening the uncovered Ge region, in other words, by increasing the R_{Air}. Therefore, R_{Air} is set to the minimum value (3 µm) and then, $L_{Underetcing}$ is altered. However, even though strain increases with increasing the underetching length, a remarkable change in strain level could not be achieved, as seen in Fig. 4.7(b).

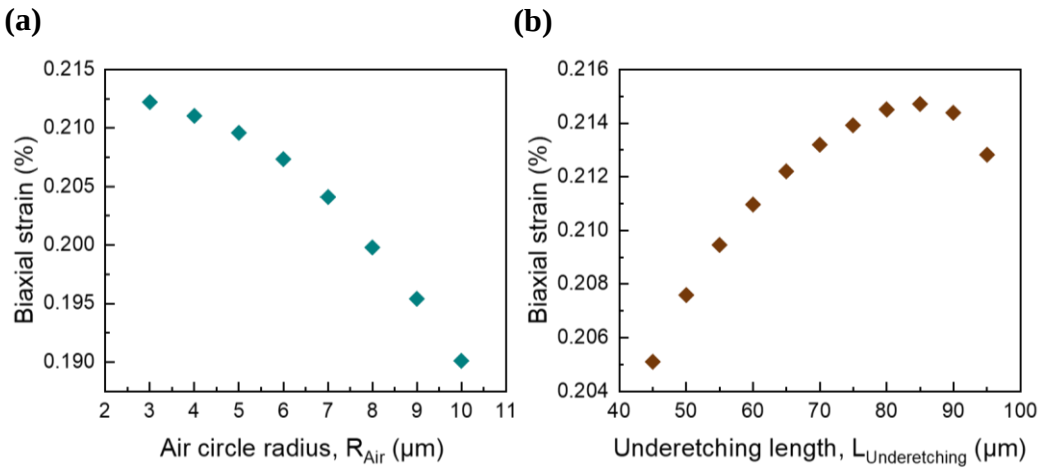

Figure 4.7 Change in biaxial strain with (a) varying air circle radius (R_{Air}) where $L_{Underetcing}$ = 65 μm and (b) varying underetching length ($L_{Underetcing}$) with R_{Air} = 3 μm.

Additional etch holes are designed to increase strain and added in Fig. 4.8(a); the 3-dimensional model of the structure built in the COMSOL is renewed by additional holes, as shown in Fig. 4.8(b).

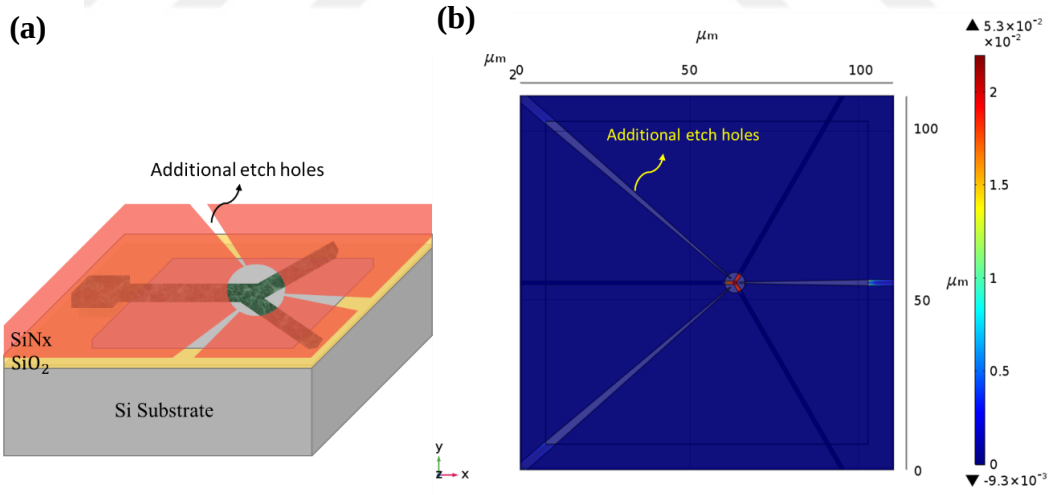

Figure 4.8 Renewed biaxial tensile-strained Ge microstructure design (a) illustration with additional etch holes, and (b) top view of whole structure with biaxial strain distribution performed using COMSOL.

Strain distribution profiles before and after additional etch holes are given in Fig. 4.9(a) and Fig. 4.9(b), respectively. Additional etch holes allow for a significant increase in strain level from 0.2 % to 2.4 %, which are evaluated from a point located at equal distances to x, y and z coordinates of the mid-region of Ge where the three tails meet. Therefore, while designing a photolithography mask, it is decided to include a sublayer to obtain these additional etch holes.

(a) **(b)**

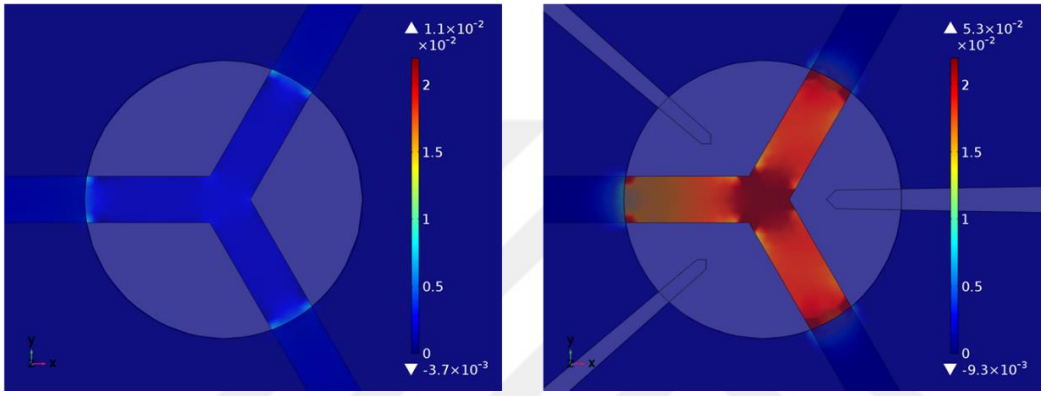

Figure 4.9 Zoom-in strain distribution profile which is localized in the mid-region of Y-shaped Ge microstructure (a) without and (b) with additional etch holes resulting 0.2 % and 2.4 % strain levels, respectively.

CHAPTER 5

FABRICATION OF STRAINED GE MICROSTRUCTURES

This chapter begins with a brief introduction of the liquid phase epitaxy (LPE) technique, which assists in the crystallization of Ge stripes. Following that, fabrication steps of uniaxially and biaxially tensile-strained Ge microstructures via a stressor layer are described, respectively.

5.1 Liquid Phase Epitaxy

The growth method by liquid phase epitaxy (LPE) is first proposed by Liu et al. to deal with the adverse outcomes of the direct Ge film growth on Si substrate, such as dislocations and defects on crystal germanium. Thus, single-crystal Ge with a unique quality is achieved [119].

In this technique, the Ge stripe is in contact with Si substrate from a very narrow region instead of the entire film surface to prevent defect formation and encapsulated with two insulators [119], [120]. Insulator layers play an essential role in holding the liquid Ge into the defined shape during Ge in a liquid form. Until reaching the liquid phase form of Ge, the structure is heated via a rapid thermal annealing system (RTA). The arranged temperature is higher than the melting temperature of Ge, 937 °C, and lower than Si's 1414 °C melting temperature. After that, to initiate the crystal growth of Ge, it is cooled down below the liquid-solid equilibrium temperature within a short time. The area in which Ge touches the Si is called seed. It is very narrow to prevent defect propagation along horizontal direction via the effect of the necking mechanism in Fig. 5.1 where the seed window meets with the Ge stripe [120], [121], which means that beyond the seeding area, defect-free Ge can be achieved.

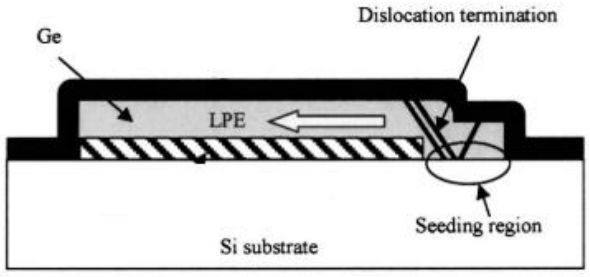

Figure 5.1 Termination of the dislocations in the seed zone by a necking mechanism [121].

Here, Si atoms diffuse into the Ge from the seed window when Ge is in liquid form; the solidification temperature in this region is higher than the Ge stripe's continuation due to higher Si composition availability, as shown in Fig. 5.2 [122], [123]. Hence, the liquid phase epitaxial growth starts from the seed and continues in a lateral direction along the Ge stripe.

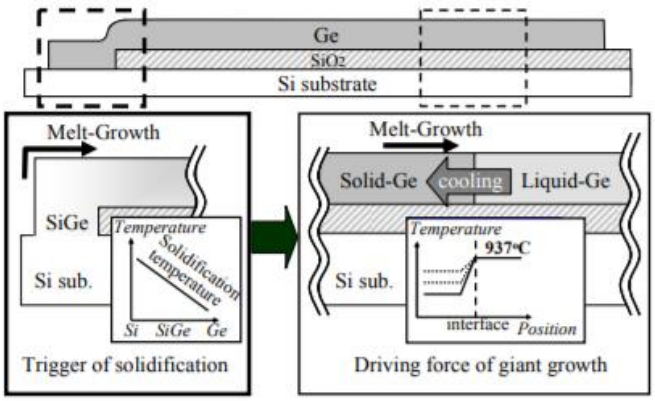

Figure 5.2 Cross-sectional schematics of rapid melting growth by Si/Ge mixing from the seed window and far beyond the seed region [122].

Random nucleation occurs due to the slower growth propagation speed than Ge's crystallizing, making Ge polycrystalline instead of a single crystal [119]. For that matter, heating and cooling temperatures should be adjusted considering this situation. Eventually, the Ge crystallization process from the Ge/Si interface is observed; the orientation of single-crystal Ge becomes identical with a silicon substrate, as shown in Fig. 5.3 [124].

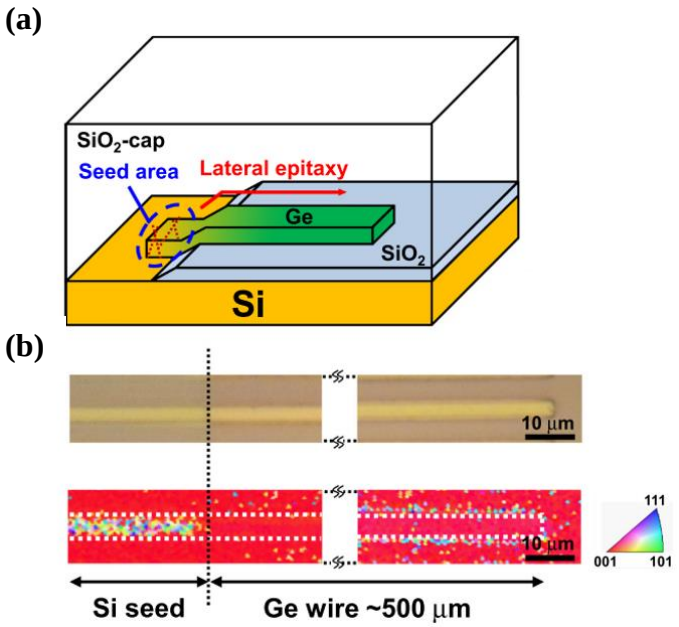

Figure 5.3 Ge-on-insulator structure (GOI). (a) Demonstration of lateral liquid-phase epitaxial growth. (b) Optical microscope image of Ge stripe (top); its crystal orientation via electron backscattering diffraction (EBSD) analysis (bottom), which follows the orientation of (100) Si substrate along the Ge wire [124].

5.2 Process Flow of Strained Ge Microstructures via Stressor Layer

As indicated in chapter 4, the dimension of the microstructures is determined according to COMSOL Multiphysics simulation results giving the highest strain level with respect to the specific designs. In the light of these dimensions, before starting the fabrication of strained Ge microstructures, a photomask that includes patterns of structures to be fabricated is designed via using software programs of CATIA and AutoCAD. This mask is used in photolithography processes to transfer the predefined mask's patterns to a film surface. The mask which is designed for this study consists of 29 different layers (sub-masks). Each layer is coded depending on the process flow and type, as indicated in Fig. 5.4. Design contents of these layers are given in the following sections, where the layers are applied to fabricate the

structures. Mask is manufactured by an institution with a material of Soda Lime glass and the sizes of 5" x 5" x 0.09".

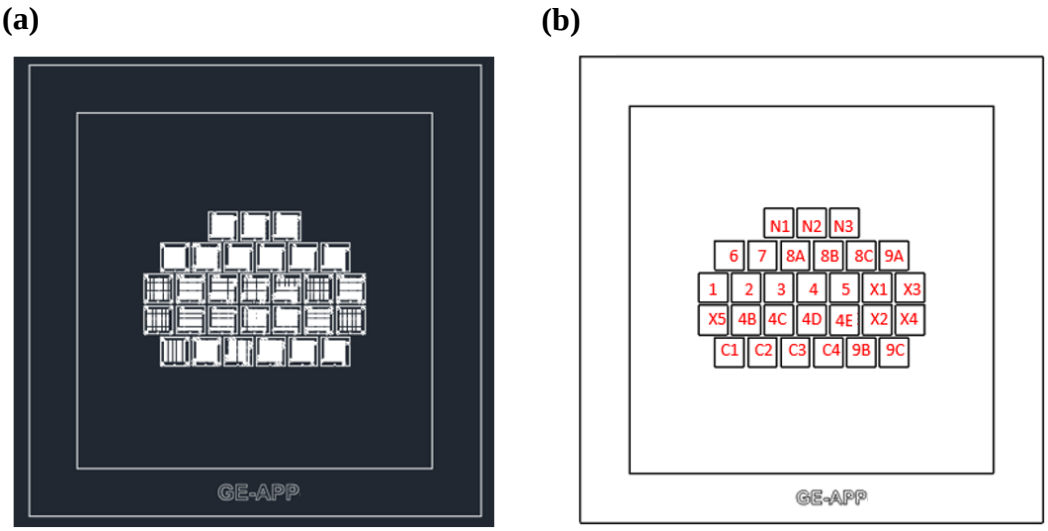

Figure 5.4 Zoom-out view of designed photomask including (a) 29 different mask layers (sub-masks) and (b) the codes of layers.

Non-stoichiometric silicon nitride (referred to as nitride or SiNx) is simultaneously examined for the film's potential to act as a stressor layer and the amount of transferring strain. After that, the fabrication process begins.

5.2.1 Investigation of Silicon Nitride as a Stressor Layer

Before fabricating Ge microstructures, silicon nitride (SiNx) is analyzed since the SiNx film is planning to be used as a stressor layer. For this purpose, a nitride film is deposited on Si substrates (1x1 cm^2) by sputtering deposition, one of the physical vapor deposition (PVD) techniques. It is aimed to find fabrication parameters that provide maximum tensile and compressive stress for transferring strain to the germanium. Sputtering target material, radio-frequency (RF) power, deposition pressure, argon and nitrogen gas flow rates, and deposition duration are the sputtering parameters varied as shown in Table 5.1 to observe their effects on stress

levels. Nitrogen (N_2) and argon (Ar) flow rates are set considering their sum giving 20 sccm. Following that, the thickness and refractive index of the deposited films are determined using ellipsometry measurements (in Table 5.1), where the spectra taken are fitted using the Tauc-Lorentz function. It is observed that the increase in deposition pressure causes a reduction in the refractive index of SiNx film. The film deposited with a high deposition pressure grows in porous form because the SiNx atoms could not be stacked tightly enough on Si substrate due to higher pressure exposure [125].

Table 5.1 Sputtering deposition parameters and ellipsometry measurement results of silicon nitride film.

Sputtering Deposition Parameters							**Ellipsometry Measurements**	
Target	**RF Power (Watts)**	**Pressure (mTorr)**		**Gas Flow Rates (sccm)**		**Duration (min)**	**Film**	
		Deposition Pressure	Base Pressure	Ar Flow	N_2 Flow		Thickness (nm)	Refractive Index (@632.8nm)
SiNx	350	5e-7	4	20	-	50	68.4	1.97
		1.9e-7	6				63	1.94
		1.9e-7	8				62	1.79
		2.3e-7	12				73.9	1.59
		7.5e-7	16				51.9	1.71
		8e-7	20				74.2	1.61
Si	300	2e-6	4	19	1	30	95.4	1.88
				18.5	1.5		40	1.93
				18.4	1.6		62.6	1.94
				18.3	1.7		55.4	1.95
				18.4	1.6	60	101	1.91
				18.4	1.6	120	190	1.98

The type of stress (tensile or compressive) and its level depend on the film's quality. Therefore, Fourier transform infrared spectroscopy (FTIR) measurements are performed to characterize the chemical bonding of the nitride films. FTIR spectra of the films sputtered under 6 different deposition pressure conditions are shown in Fig. 5.5(a). Absorption at roughly the wavelength of 850 cm^{-1} that is more prominent in the spectra of 4 mTorr and 6 mTorr, results from Si-N stretching mode [126]. This peak becomes less pronounced with increasing the deposition pressure, which indicates the weakening of Si-N bonds, forming a porous film.

In order to utilize the LPE technique, SiNx will also undergo an annealing process owning to being the capping layer on the Ge. Therefore, the change in the bond formation after RTA at 1000 °C is also analyzed in Fig. 5.5(b). After annealing, the formation of Si-O stretching mode is observed at higher deposition pressures. That bond can occur due to possible oxygen in the environment during the RTA process. While denser films deposited at lower pressures are not affected, porous films contain Si-O bonds. As seen clearly in Fig. 5.6, silicon nitride film deposited at 4 mTorr preserves its bond structure quality, while oxidation is observed in the 20 mTorr film after annealing.

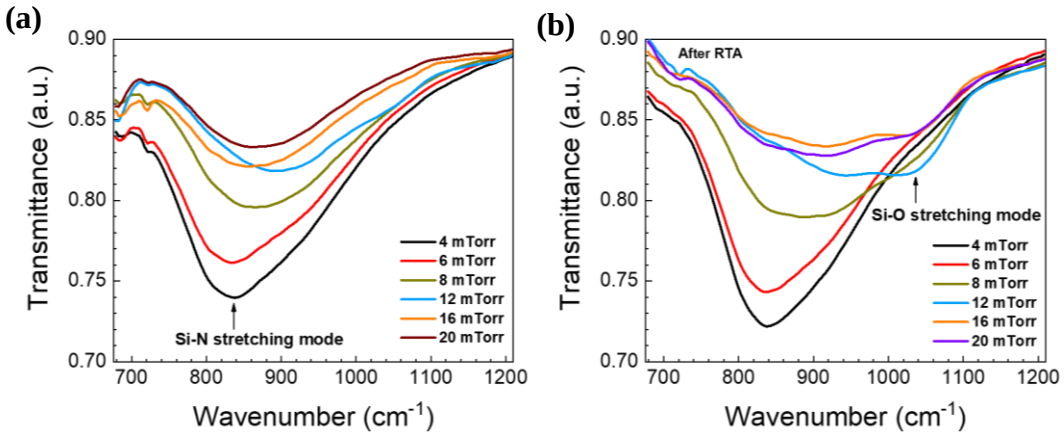

Figure 5.5 FTIR spectra of silicon nitride films sputtered using a SiNx target at different deposition pressures (a) after deposition and (b) after RTA at 1000 °C.

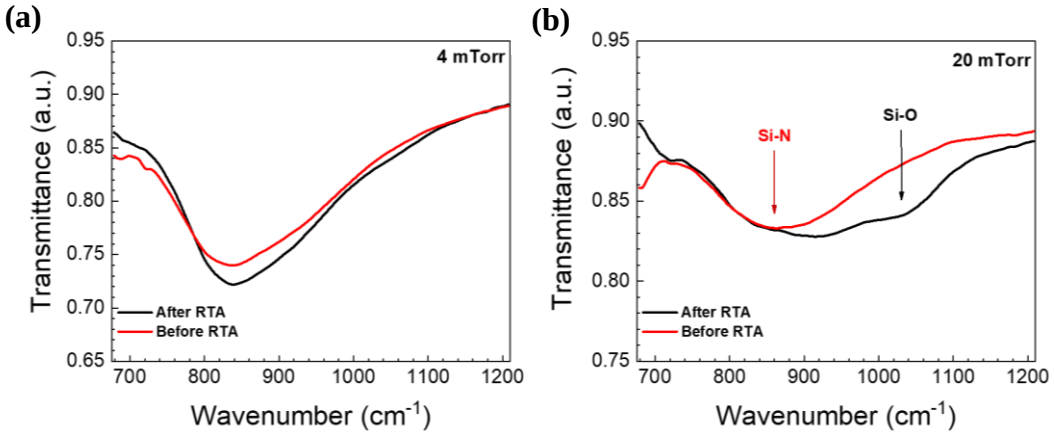

Figure 5.6 FTIR spectra of films deposited using a SiNx target at (a) 4 mTorr and (b) 20 mTorr, before and after RTA at 1000 °C.

Surface profiles of the films sputtered at different pressures are measured before and after annealing, as given in Fig. 5.7, to quantify the surface stresses by using Veeco Dektak 6M Profilometer. As a result, the curvature radii of the profiles are extracted.

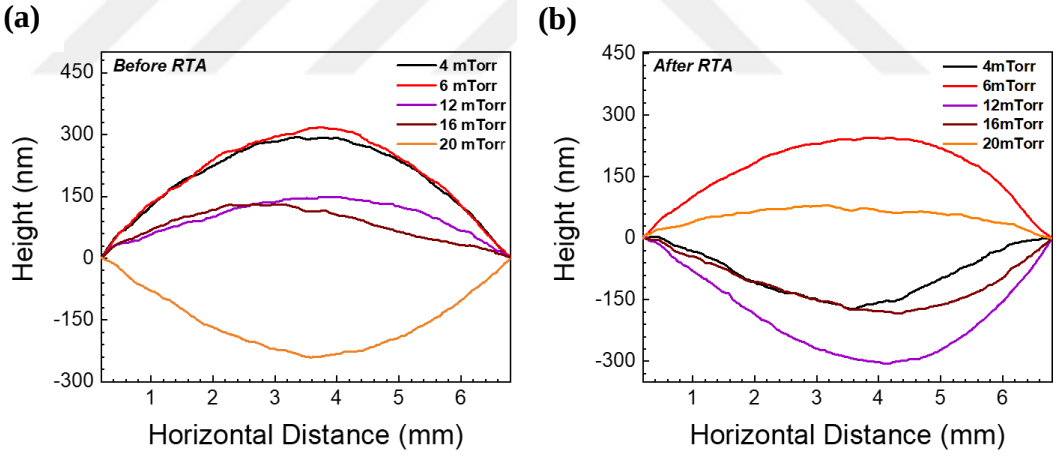

Figure 5.7 Surface profiles of silicon nitride films deposited using a SiNx target in different pressures (a) before RTA and (b) after RTA at 1000 °C.

After that, the radii are used in the equation below to get stress values [127].

$$\sigma_f = \frac{E_s {d_s}^2}{6(1-\nu_s)d_f}\left(\frac{1}{R_f} - \frac{1}{R_o}\right) \tag{5.1}$$

E_s is the young modulus of the substrate, equals 170 GPa for Si, h_s is the thickness of Si substrate that is 300 μm in our case, and thickness of the film is symbolized with h_f where its value is taken from the ellipsometry measurements (in Table 5.1). ν_s is the Poisson ratio (0.27); curvature radii before and after deposition are R_o and R_f. When all these values are substituted in Eq. (5.1), the results of film stresses are given in Fig. 5.8. Here, the positive stress indicates tensile stressed films, while the negative stress is compressively stressed films.

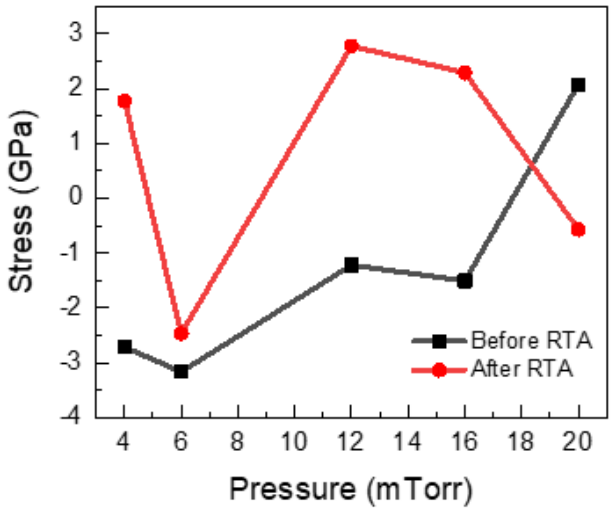

Figure 5.8 Stress values in silicon nitride films deposited using SiNx target at different deposition pressures.

It is observed that compressive stress reduces with increasing deposition pressure before annealing as specified in literature [128], [129]. However, the RTA process mainly causes to alteration of the compressive stress to tensile one. As a result, silicon nitride films with both tensile and compressive stresses are fabricated where the sputtering target is SiNx, and the RTA effect on stress is also investigated.

On the other hand, the deposition rate (nm/min) is below the sufficient level when the target material in sputtering is SiNx. Hence, reactive magnetron sputtering where Si target and nitrogen gas at some degrees have been involved is examined for the

deposition of the silicon nitride film, resulting in the same thickness with less duration as desired (in Table 5.1). Stress quantity and its type using the Si target are analyzed, where deposition pressure is kept constant at 4 mTorr, and nitrogen gas flow is varied, as shown in Table 5.1. Surface profiles and curvature radii of silicon nitride films for 4 different nitrogen gases before and after RTA are taken by Dektak profilometer in Fig. 5.9. From the spectra, it can be asserted that compressive stress is acquired by 1 sccm, 1.5 sccm and 1.6 sccm nitrogen gas flows, while 1.7 sccm causes tensile stress on silicon nitride in Fig. 5.9(a). After annealing the films, stress types deposited with 1.5 sccm and 1.6 sccm nitrogen gases remain unaffected in Fig. 5.9(b). Therefore, in the 1.6 sccm environment, the change in the stress value and its type depending on the film thickness are also investigated following.

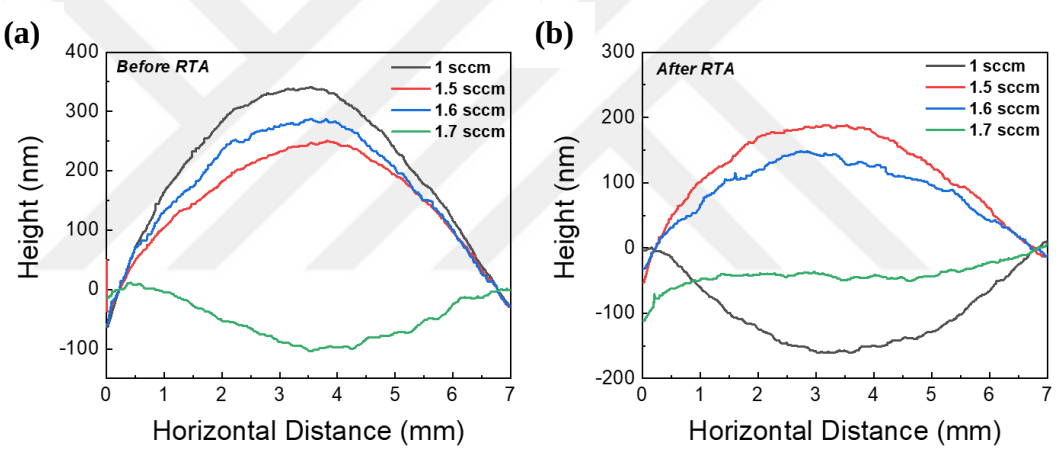

Figure 5.9 Surface profiles of films deposited by reactive magnetron sputtering technique using Si target for different nitrogen gas flows (a) before and (b) after RTA.

Deposition pressure is set as 4 mTorr, and RF power is 300 W. Three different films are sputtered with the duration of 30-, 60- and 120-minutes at 6 sccm. Following that, the surface profiles are measured before and after annealing in Fig. 5.10(a) and in Fig. 5.10(b), respectively. The resulting profiles show that all 3 films fabricated under the same conditions have compressive stress independent of the deposition duration.

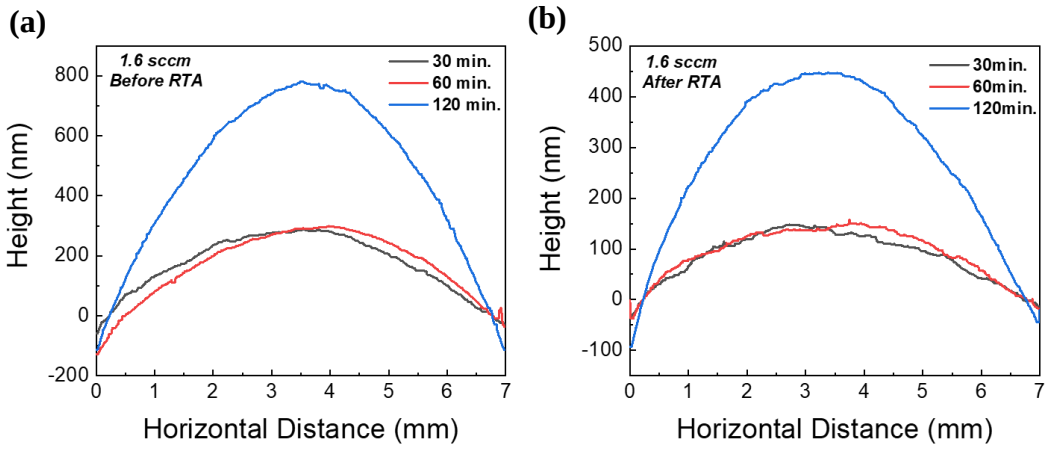

Figure 5.10 Surface profiles of films deposited by reactive magnetron sputtering technique using Si target for different deposition duration at 1.6 sccm nitrogen gas flow (a) before and (b) after RTA.

The radii of curvature obtained from the surface profiles shown in Fig. 5.9 and Fig. 5.10, and the film thicknesses (in Table 5.1) are substituted in Eq. (5.1); after that, the stress values in these films are calculated. The results obtained from the profiles are given in Fig. 5.11(a) and in Fig. 5.11(b), respectively.

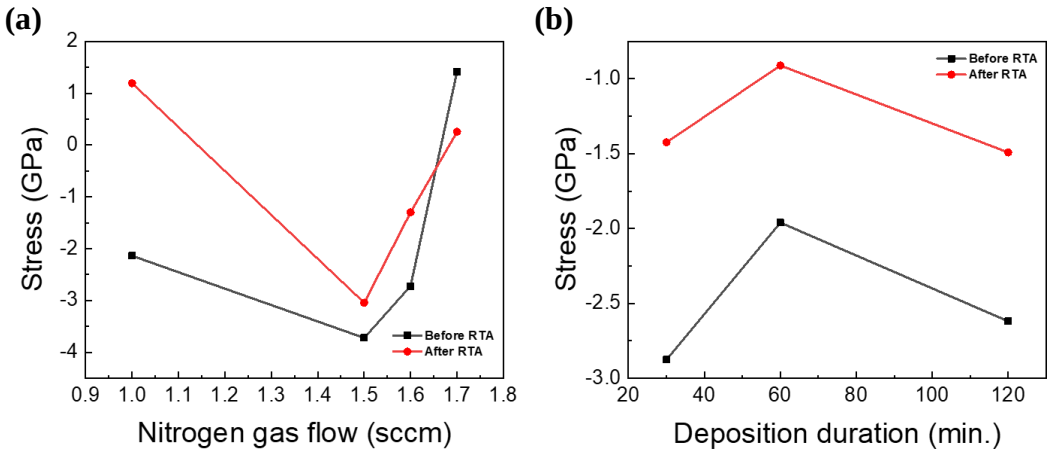

Figure 5.11 Stress values obtained before and after annealing of silicon nitride films deposited by a reactive magnetron sputtering method using the Si target (a) at different nitrogen gas flows and (b) at different deposition duration (thicknesses) in an environment of 1.6 sccm nitrogen gas flow.

In brief, fabrication of silicon nitride film with compressive stress is not only possible by using SiNx target but also Si target in sputtering. Therefore, the Si target can be preferred for time-saving, and Ge microstructures can be capped with a silicon nitride film deposited in an environment where nitrogen gas flow is 1 sccm (19 sccm for oxygen gas flow) to get roughly 1 GPa stress level.

5.2.2 Fabrication Steps

Silicon wafer with the properties given in Table 5.2 is used as a substrate and cleaned using the solutions of RCA-I (i.e., ammonium hydroxide (NH_4OH), hydrogen peroxide (H_2O_2) and DI water with a ratio of 1:1:5) and RCA-II (i.e., hydrochloric acid (HCl), H_2O_2 and DI water with a ratio of 1:1:5) for 10 minutes at 75 °C. This cleaning is necessary to remove the organic contaminants and metal ions from the Si wafer, respectively. The surface of Si is oxidized after the cleaning; therefore, hydrofluoric acid (HF) is employed to obtain a pure Si wafer.

Table 5.2 Silicon wafer properties.

Type of wafer:	Mono n-type
Growth method:	Czochralski (CZ)
Dopant element:	Phosphorus
Thickness:	280 µm
Resistivity:	1-3 ohm.cm
Orientation:	<100>
Wafer finish frontside/backside:	Double Side Polished (DSP)

Following that, the Si wafer's surface is thermally oxidized to acquire a high quality and stress-free silicon dioxide (SiO_2) layer on top of Si with a thickness of 81 nm measured via ellipsometry. The obtained sample is cut into 1.3x1.3 cm^2 squares that is consistent with the dimensions of the sub-masks (i.e., 0.8x0.8 cm^2). To take advantage of the LPE method, seed windows are defined by the following first

photolithography process as illustrated in Fig. 5.12. First of all, the sample in Fig. 5.12(a) is cleaned from the possible organic residues via acetone, isopropyl alcohol (IPA) and deionized (DI) water, respectively in an ultrasonic machine at 55 °C for 10 min.; nitrogen gun and hot plate are used to dry the sample. S1805 positive photoresist (PR), where only UV light exposed regions are solved in the developer solution, is applied to coat the sample by a spin coater at 4000 rpm spin speed. After the coating, dehydration and adhesion of the PR layer are provided by heating the sample at 115°C for 60 seconds on the hot plate, called soft bake. Following that, the designed mask layer 1 (in Fig. 5.13) is used to define 3x3 cm^2seed windows. After contact of the mask and the sample, 26.13 mJ/ cm^2 ultraviolet light (UV) is exposed in Fig. 5.12(b) via a mask aligner system; so that the seed window with the desired pattern is transferred to the sample. The physical property of selectively UV-exposed PR region is changed; therefore, it is dissolved when AZ 726 MIF developer is applied, as shown in Fig. 5.12(c). Here, development time is very crucial. In a long time, all photoresist layers are removed; but the desired dimensions and shapes cannot be obtained in a short time. Therefore, duration should be adjusted very carefully. Then, the sample is kept on the hot plate at 120 °C for 180 seconds to make sure the solvent is completely removed, harden the remaining PR, and make PR resistant to etchant solutions, which is called hard bake. After that, SiO_2 located in the seed region whose surface is not protected by PR is etched by buffered oxide etchant (BOE) in Fig. 5.12(d), and the etching is stopped via DI water after reaching the surface of Si substrate. Whether the SiO_2 in seed window has been etched without any residue left, hydrophobicity of the outside of the mask layer is check. Being hydrophobic is proof that the SiO_2 is etched on Si and the remaining surface is Si that is hydrophobic in nature unlike the SiO_2. The last step is removing the rest of the PR via acetone. Also, to remove PR precisely, acetone, isopropyl alcohol (IPA) and deionized (DI) water are applied respectively in an ultrasonic machine at 55 °C for 5 min. At last, seed window is defined as demonstrated in Fig. 5.12(e).

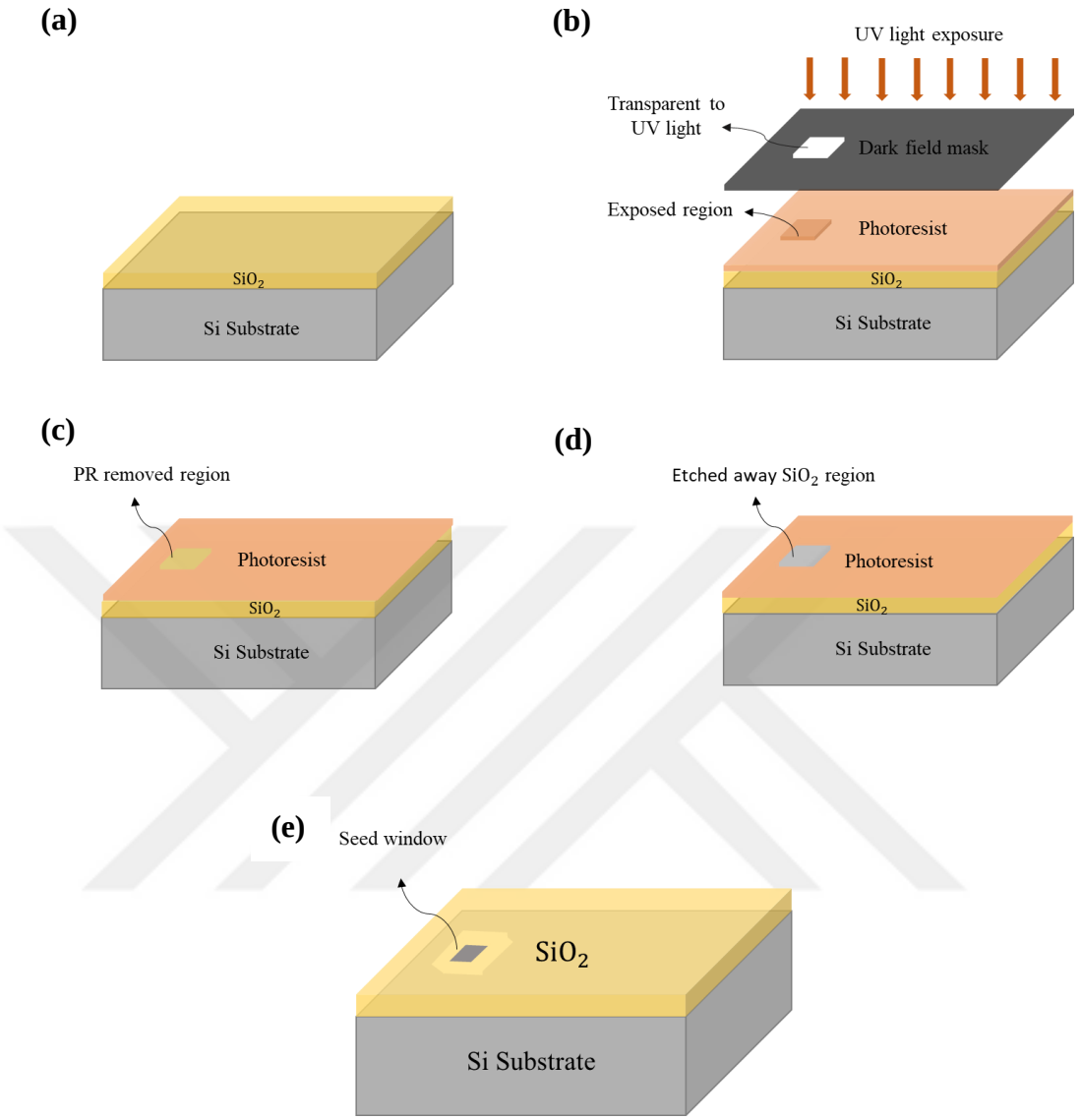

Figure 5.12 Photolithography process flow to create a seed window. (a) Thermally growth SiO_2 on top of the Si sample. (b) Exposing the photoresist (PR) coated sample to UV light in which mask layer 1 is used. (c) After etching the exposed PR region within a developer solution. (d) After etching of the specified SiO_2 area with buffered oxide etchant (BOE). (e) After removal of PR from the surface via acetone and isopropyl alcohol (IPA).

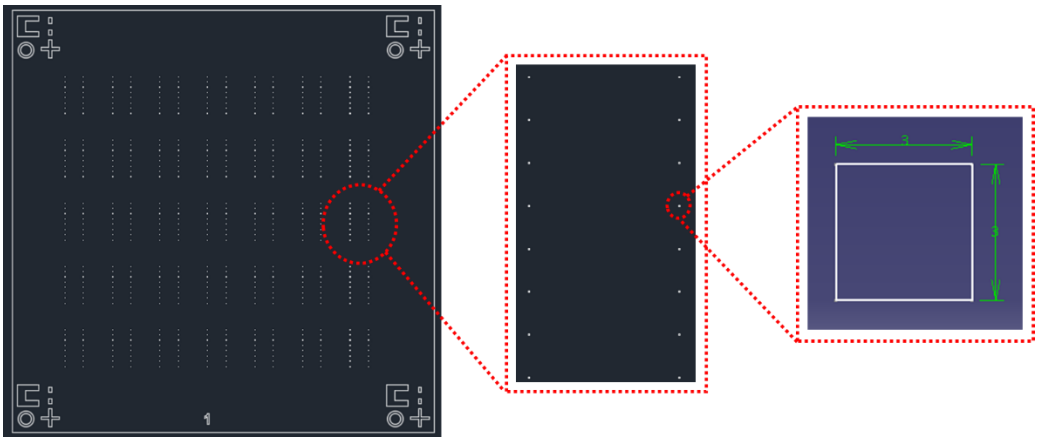

Figure 5.13 Mask layer 1 designed for seed windows photolithography process consisting of 3x3 cm^2squares.

Optical microscope using 100X objective and scanning electron microscope (SEM) images of seed window are taken as given in Fig. 5.14.

(a)

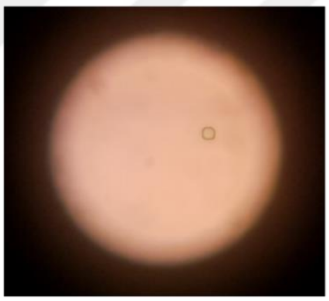

(b)

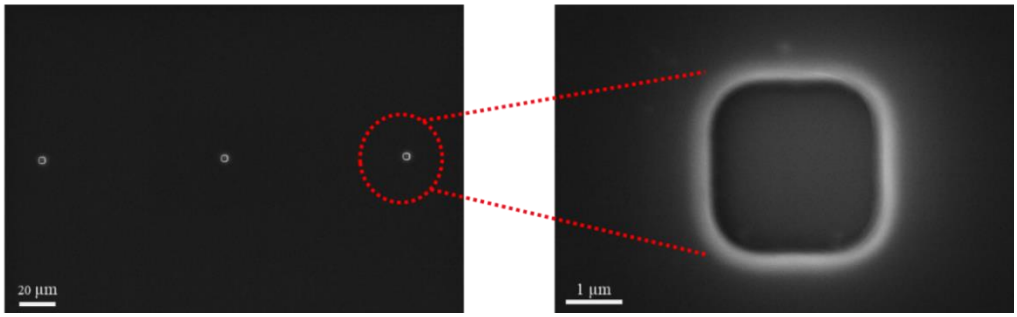

Figure 5.14 The defined seed window's (a) optical microscope image using 100X objective and (b) SEM images with 20 µm and 1 µm (zoom-in) scales, respectively.

Additionally, a seed window before the step of removing the PR (Fig. 5.12(d)) in which roughly 500 nm-thick thermally growth SiO_2 sample used is cut from the midpoint; its 80° tilted SEM image is taken as shown in Fig. 5.15(a). Thereby, the isotropic etching profile with a slight undercut below the PR layer is observed clearly. Also, the height measured approximately 937.5 nm (Fig.5.15(b)) can confirm that SiO_2 in the seed region is successfully removed as being close to the sum of SiO_2 and photoresist heights, which are approximately 500 nm and 400 nm.

(a)

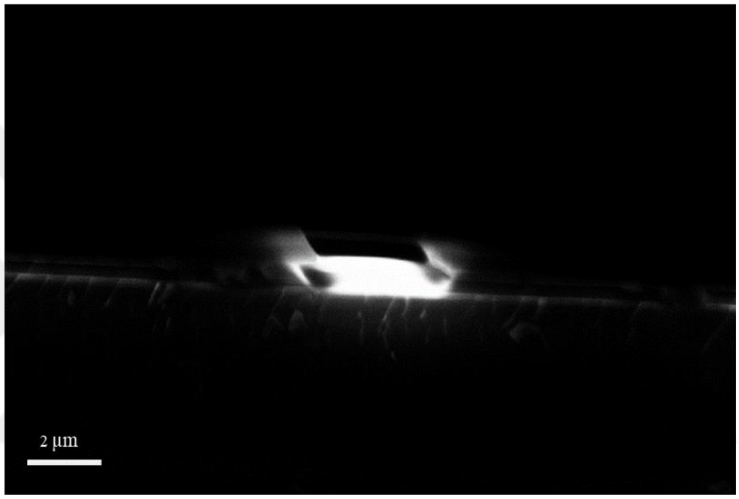

(b)

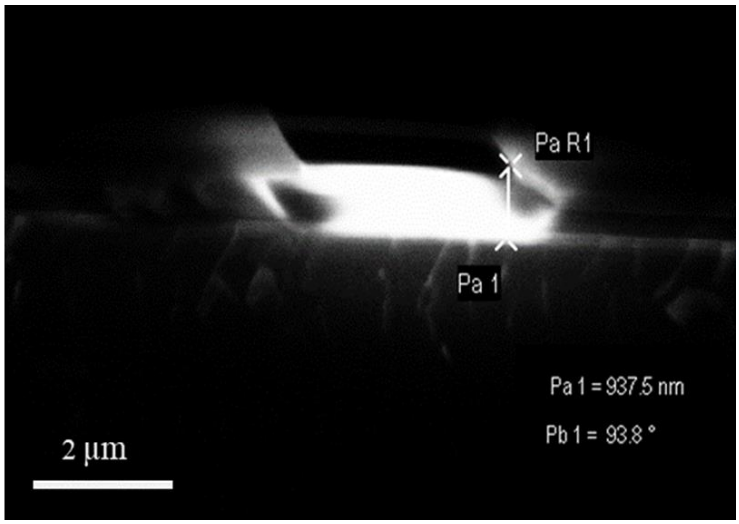

Figure 5.15 80° tilted SEM image of (a) the seed window (b) with height measurement.

After defining the seed windows on the sample, the process flow continues by deposition of the germanium. For that purpose, sputtering deposition is implemented. It takes place in an environment with 200 W RF power, 2 mTorr deposition pressure, 20 sccm argon flow, and a base pressure of approximately $4x10^{-7}$ Torr in Table 5.3.

Table 5.3 Ge film sputtering deposition parameters.

Target	**RF Power (Watts)**	**Pressure**		**Gas Flow Rate**
		Base Pressure (mTorr)	Deposition Pressure (Torr)	Argon Flow Rate (sccm)
Ge	200	2	$4x10^{-7}$	20

Four Ge films are deposited on Si substrate with different power and deposition pressure values in Table 5.4 to determine the RF power and deposition pressure parameters. Then, the roughness of films is measured using atomic force microscopy (AFM). In accordance with the results (in Fig. 5.16), it is obtained that the minimum root mean square (RMS) roughness (Rq) is achieved with higher RF power and lower deposition pressure. Therefore, 200 W and 2 mTorr are chosen as deposition parameters; Ge film in the amorphous form is fabricated with the thickness of roughly 260 nm, which is measured by Veeco Dektak 6M Profilometer. Herein, to ensure that the seed windows are filled with germanium, the thickness of the Ge film is adjusted to be a minimum of 100 nm, thicker than the thickness of the 81 nm-thick thermally growth SiO_2.

Table 5.4 AFM results for different deposition parameters of Ge.

Ge Deposition Parameters	Roughness Average (nm)	Root Mean Square (nm)	Surface Skewness	Surface Kurtosis
200 W, 2 mTorr	0.6132483	0.8629907	3.346755	41.28211
200 W, 5 mTorr	0.8449203	1.129518	-0.9538143	17.12511
200 W, 8 mTorr	1.28428	1.697388	1.712517	43.54001
100 W, 5 mTorr	0.9180121	1.168602	0.3867953	4.884734

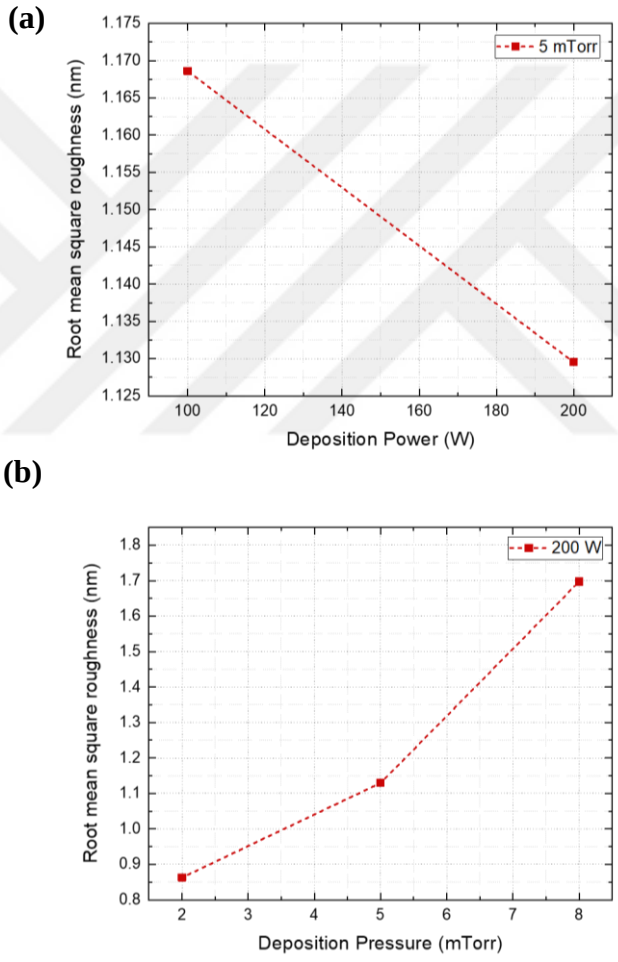

Figure 5.16 The change of root mean square (RMS) roughness (Rq) according to (a) the deposition power where the deposition pressure is kept as 5 mTorr, and (b) the deposition pressure in which the deposition power is 200 W.

An illustration of the sample after deposition of amorphous Ge is given in Fig. 5.17. The inhomogeneous film thickness occurred in the seed region is just ignored for schematic. After deposition, Ge is patterned via the second photolithography process to obtain uniaxial or biaxial strain on Ge.

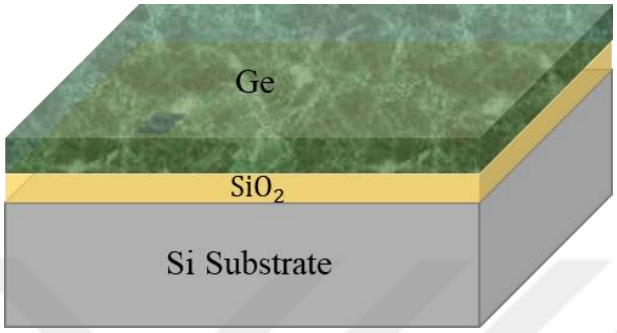

Figure 5.17 Schematic of the sample after the sputtering deposition of Ge.

5.2.2.1 Uniaxially Tensile-Strained Ge Microstructures

The second photolithography process is applied to pattern the Ge film with specific mask layers, which result in uniaxial strain. All the steps, including cleaning the sample, covering it with the PR, baking, and development processes, are the same as the first photolithography. The differences are the mask layer used and marker alignment steps. Sub-mask numbered 2 that consists of the uniaxial microstructures as shown in Fig. 5.18 is applied. For this purpose, it is aligned with the markers of the previous transferred mask layer 1 to overlap the seed windows with the Ge stripes. Thus, all sub-masks include alignment marks located at the corners to superimpose one layer over the previous layers for subsequent patterning. Hence, before exposing the sample to UV light, the alignment marks of the layers are matched with each other in Fig. 5.19 via using the microscope of the mask aligner system.

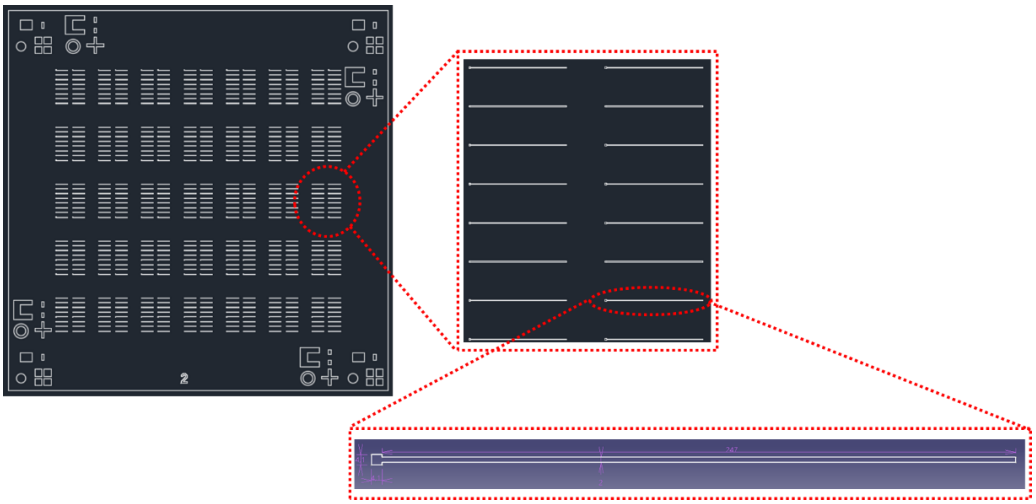

Figure 5.18 Mask layer 2 designed for Ge stripe structure, consisting of a 2x247 μm^2 rectangle and a 4.1x4.1 μm^2 seed square.

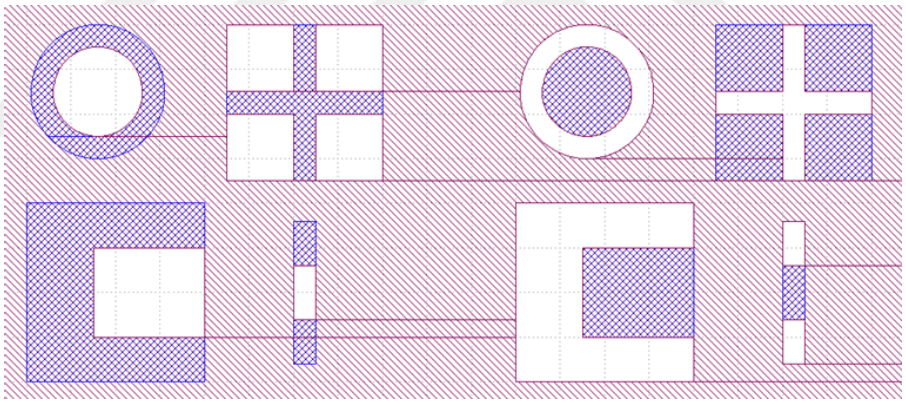

Figure 5.19 The matched view of two alignment marks (filled and unfilled geometrical shapes).

The result of the second photolithography is the patterned PR layer where the sub-mask 2 design is transferred, as illustrated in Fig. 5.20.

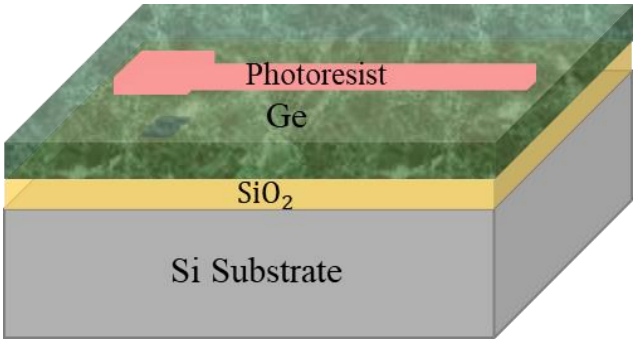

Figure 5.20 Photoresist patterned by second photolithography in which sub-mask 2 is implemented.

The region of Ge film, which is not protected by the PR, is etched with a wet etching process to obtain the Ge in a microwire geometry, called Ge stripe. The mixture of solutions used for the Ge etching contains hydrogen peroxide (H_2O_2), phosphoric acid (H_3PO_4), and deionized water (H_2O) in a ratio of 4:1:1, respectively. After removing the remaining PR with the same PR cleaning steps, Ge takes the shape of the designed structure indicated in sub-mask 2 as illustrated in Fig. 5.21.

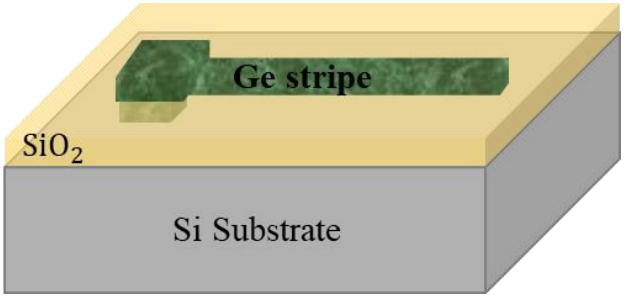

Figure 5.21 Illustration of the Ge microstructure.

Any misalignment of the mask layers 1 and 2 can be observed via the optical microscopy in Fig. 5.22(a). In such a case, the resist is cleaned instead of the Ge etching process at the end of the second lithography. The second lithography is repeated until a successful alignment is achieved, as shown in Fig. 5.23.

(a)

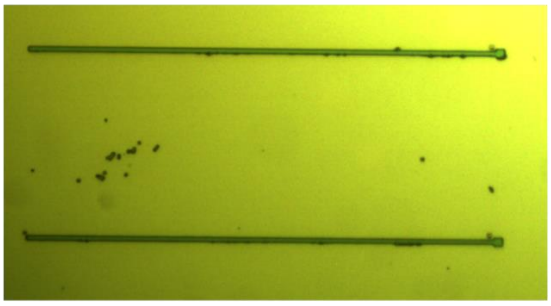

(b)

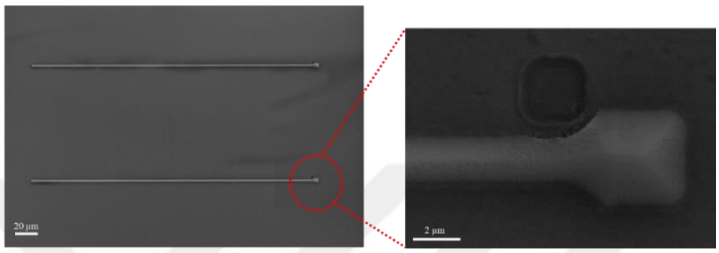

Figure 5.22 Misaligned seed windows (sub-mask 1) with Ge stripes (sub-mask 2). (a) Optical microscope image and (b) SEM images with 20 µm and 2 µm (zoom-in) scales, respectively.

(a)

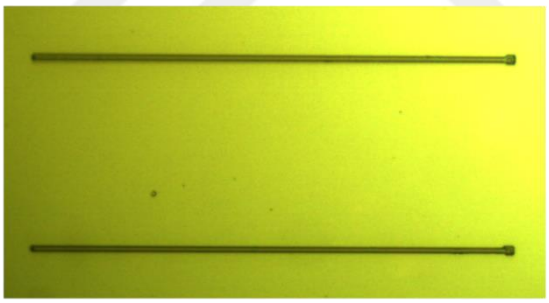

(b)

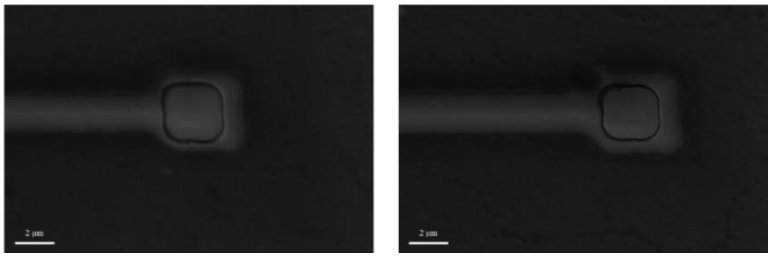

Figure 5.23 Aligned seed windows (sub-mask 1) with Ge stripes (sub-mask 2). (a) Optical microscope image and (b) SEM images of two aligned seed windows and Ge stripes.

Fabrication continues by covering the sample with the silicon nitride (SiNx) stressor layer. It is deposited by the sputtering technique, whose parameters are determined as 300 W RF power and 4 mTorr deposition pressure in a 1.08 x 10^{-6} Torr base pressure environment. Additionally, 1sccm nitrogen gas flow with 19 sccm argon gas flow is applied to obtain 1 GPa silicon nitride film where a Si target is used in sputtering. After the stressor layer deposition, it should be protected by a mask layer that is resistant to the SiNx etching process (i.e., applying hot phosphoric acid at a temperature roughly 160°C) because photoresist cannot be used due to burning nearly at the temperature of 150°C [130], [131]. Therefore, SiO_2 to serve as a thin masking layer is sputtered on top of the SiNx film with the deposition parameters of 300 W RF power and 4 mTorr deposition pressure where the base pressure is 1.3 x 10^{-6} Torr. The gas flows of oxygen and argon are 2.8 sccm and 15 sccm with the Si target material. As a result, the thicknesses of the films grown by the sputtering method are 340 nm for SiNx and 140 nm for SiO_2. After that, the sample is subjected to rapid thermal annealing (RTA) to crystallize the Ge microstructures via the LPE method. Hence, Ge is heated to a temperature above its melting temperature of 937°C. The following RTA recipe is applied. After argon gas is introduced at 0°C for the first 60 seconds, the temperature is increased from 0°C to 800°C in 30 seconds. After waiting for 60 seconds at 800°C, it reaches the desired temperature with an increase rate of 100°C/s and remains at this temperature for 2 seconds. The temperature is then brought to 650°C at a rate of 7°C/s. Four different temperatures, 960°C, 980°C, 1000°C and 1020°C, are investigated. When RTA results are compared considering the optical microscope images in Fig. 5.24, the agglomeration problem of Ge is smallest at 960°C through a faster lateral crystal growth rate than the random nucleation. Therefore, it is decided to perform the RTA process at 960°C, whose RTA recipe is given in Fig. 5.25. Otherwise, Ge stripe becomes disjointed along its length due to the formation of islands, as demonstrated in Fig. 5.26.

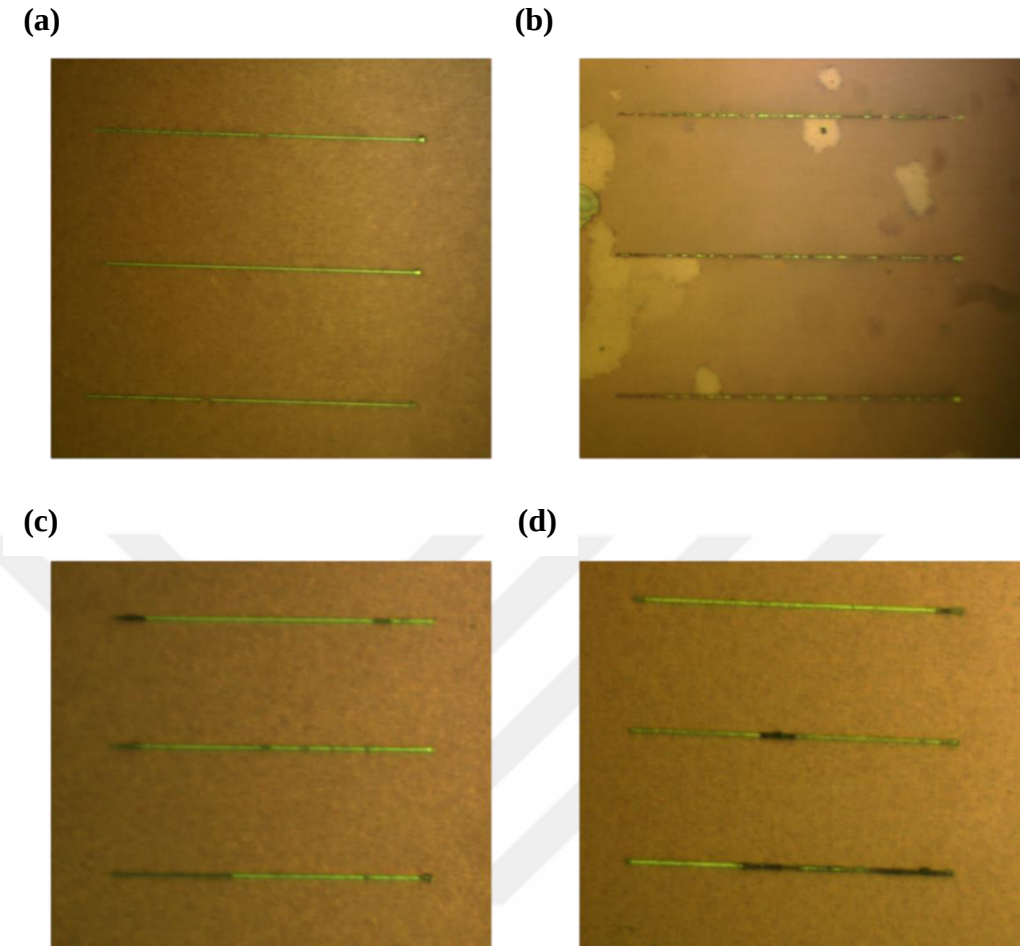

Figure 5.24 Optical microscope image of the Ge microstructures after RTA process at (a) 960°C (b) 980°C (c) 1000°C (d) 1020°C.

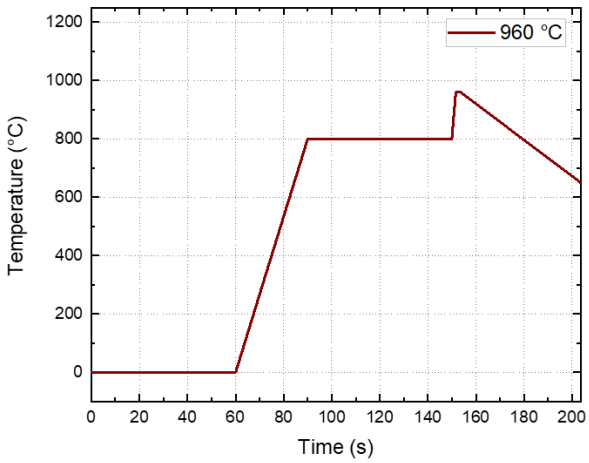

Figure 5.25 RTA recipe of 960°C used to crystallize the Ge by the LPE technique.

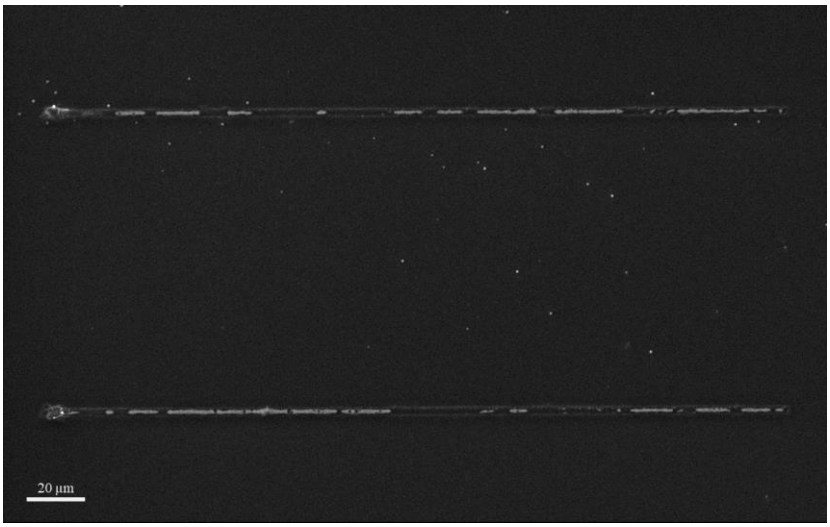

Figure 5.26 SEM image of disjointed Ge stripe by the effect of 980°C RTA process.

The last photolithography is applied to pattern the SiO_2 masking layer after 960°C RTA process in Fig. 5.27(a). As in the case of the second lithography, all the steps, including cleaning, the PR application, baking and development processes, are the same as the first photolithography. In this photolithography, the mask layer numbered 5, including the design of the 4x20 μm^2 etching holes (Fig. 5.28), is used and aligned with the marker of the previous sub-mask numbered 2. As a result of this, mask layer 5 is transferred to the PR.

Following the third photolithography, the sample is exposed to BOE solution till reaching SiNx film; so that the defined SiO_2 region that is not protected via the PR is etched away as shown in Fig. 5.27(b) after removing the remaining PR. To etch unprotected SiNx region, hot phosphoric acid (H_3PO_4), which continues to be heated on the hot plate to keep the temperature of solution around 156°C - 160°C, is exercised. The etching rate of SiNx film is observed to be about 0.94 nm/sec. Additional information here is that dummy SiO_2 and SiNx films are also deposited on top of Si substrate simultaneously with the original sample deposition; annealed with the same RTA recipe. Before performing the etching steps of the sample, to determine the etching duration, film dummies are etched. Then, these etching times are considered while etching the films of the sample. Through etching the defined

SiNx area, Ge microstructure is reached in Fig. 5.27(c). Then, the oxide layer underneath the Ge is etched via BOE to a certain length without etching the Ge. The final structure is shown in Fig. 5.27(d) and a side-view cross-section schematic to better illustrate the underetching that plays a critical role in the strain transfer. When the stand-alone portion of the nitride film releases its tensile stress, it stretches the stripe from both ends in opposite directions (as indicated with the arrows in Fig. 5.27(d)) since the top and side surfaces of the stripe are enclosed by the underetched nitride. This fabrication step also etches the sputtered SiO_2 masking layer whose thickness was adjusted accordingly to be etched earlier than thermally growth SiO_2 layer. It is also an advantage that thermally grown SiO_2 is etched more slowly than that the sputtered one. As a result, a portion of the stripe is suspended, called microbridge (MB) in this study, possessing uniaxial strain.

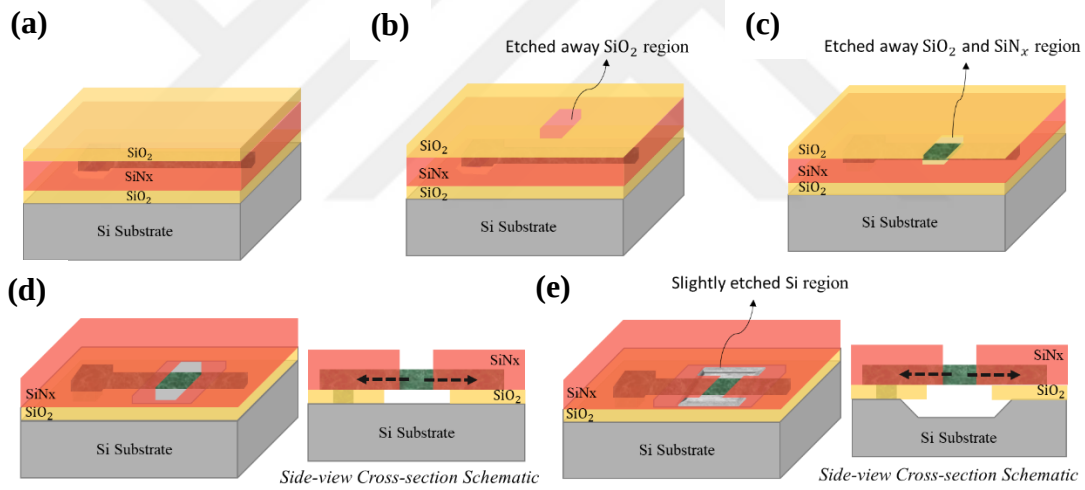

Figure 5.27 Wet etching process flow to achieve a suspended Ge microstructure. (a) The sample after deposition of the capping layers, SiNx and SiO_2, in which mask layer 5 is applied by the last photolithography. (b) Etching the unprotected SiO_2 region till reaching SiNx film. (c) Etching the defined SiNx area by hot phosphoric acid. (d) Etching the masking and sacrificial oxide layers via BOE, resulting in the suspended Ge microstructure (left) and its cross-sectional illustration (right). (e) KOH etching of Si (left) and its cross-sectional illustration (right).

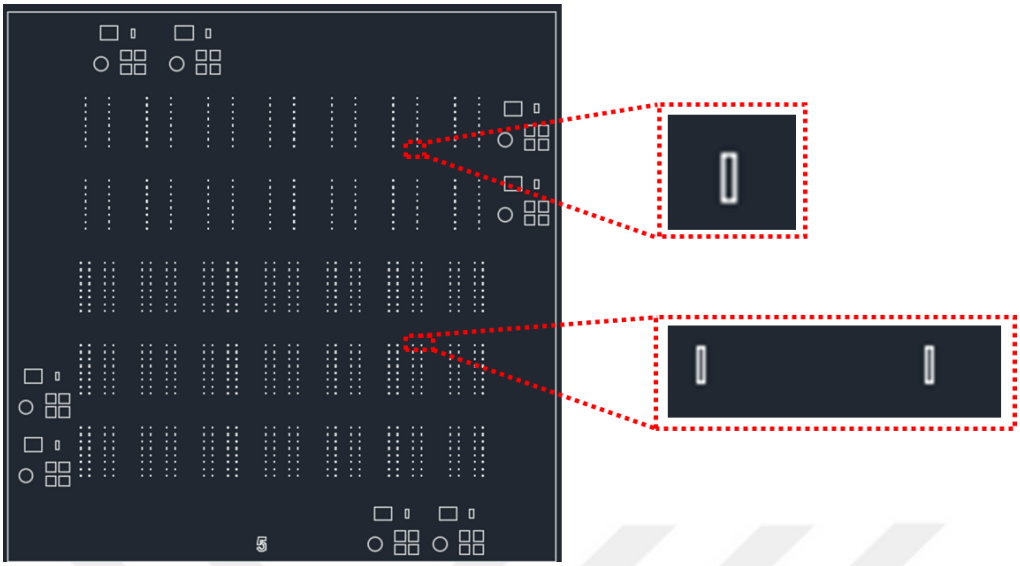

Figure 5.28 Mask layer numbered 5 designed for etching holes including the 4x20 μm^2 rectangles.

The duration of each wet etching steps is significant in terms of acquiring desired dimensions. If the first BOE is applied longer than it should be, the etch hole, namely MB, gets wider, as seen in Fig. 5.29(a), ideal (left) and unintentional (right) etch holes dimensions' microscope images. In the case of not exposing to hot H_3PO_4 for a sufficient time, nitride etching is interrupted in Fig. 5.29(b), where the film residues in the etch hole region are the sign of that. Through an additional hot H_3PO_4, the residues are totally etched; clear etch holes are achieved in Fig. 5.29(c).

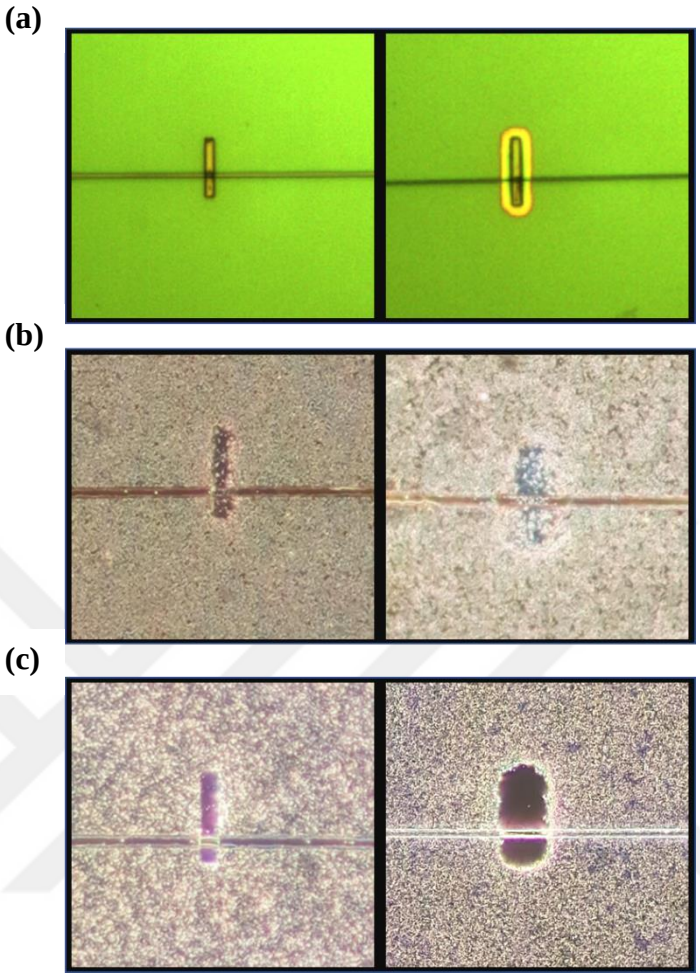

Figure 5.29 Microscope images of etch holes, namely Ge MBs. (a) Bright-field microscope images with an ideal dimension (left) and unintentional dimension (right) due to over BOE exposure time. (b) Darkfield microscope images before the film residues existing and (c) after the residues are totally etched via an additional hot H_3PO_4 etching process.

Moreover, the last BOE etching time must also be set very carefully. If the sample is subjected to the BOE for a short time, the Ge will not be suspended. On the other hand, in case of prolonged exposure, the underlying SiO_2 will be removed entirely. One possible reason is that the SiNx film, which acts as a masking layer in BOE etching, is dissolved even if the etching rate is minimal. Another reason is the

penetration of BOE also from the corners of the sample where SiNx film does not exist, completely removing the thermally growth SiO_2 layer.

SEM images taken from the germanium microbridges are given in Fig. 5.30.

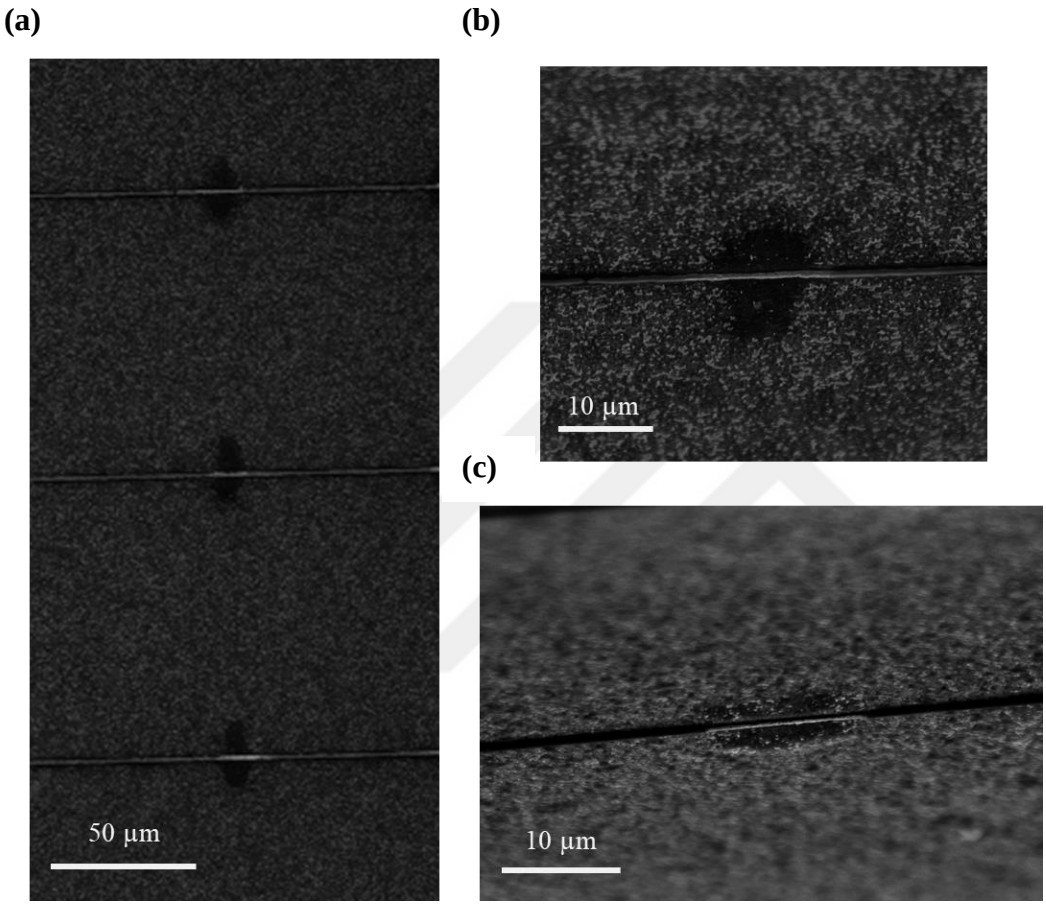

Figure 5.30 SEM images of Ge MBs. (a) SEM image from the top view demonstrating three Ge MBs. (b) 55° tilted and (c) 75° tilted SEM images of two different MBs.

An additional wet etching is implemented to some samples to ensure complete suspension of Ge microstructure by preventing the possible cases of collapse and sticking and to extend the underetching more underneath the nitride film to increase the amount of the induced strain in Fig. 5.27(d). Also, larger strain can be induced into shorter suspended structures as inferred from the FEM simulation results, 2.5-

μm-long MBs are fabricated. The fabrication of these structures is enabled by using the lithography mask with 4x20 μm^2 etchant windows on it, and simply keeping the first BOE etching duration shorter than the nominal one. After the subsequent nitride and underlying oxide etching processes, the structure is exposed to KOH. Thus, the Si surface reached at the etch hole region is slightly etched using 3.85 wt.% aqueous potassium hydroxide (KOH) solution at 70°C in Fig. 5.27(e). SEM images of 2.5-μm-long Ge MBs after KOH etching are given in Fig. 31(a). Duration of KOH is varied, which results in different portions of underetched nitride film as specified in Fig.31(b), wider for longer etching duration as expected. Also, the lengths of nitride-encapsulated Ge stripe that occurs due to collapse some parts of the free-standing nitride film right at both edges of the bridge get wider. The Ge MBs where the middle region of Ge is suspended by itself, and its edges on both sides are encapsulated by a part of nitride are shown in Fig. 5.31(b), which affects the strain level as well.

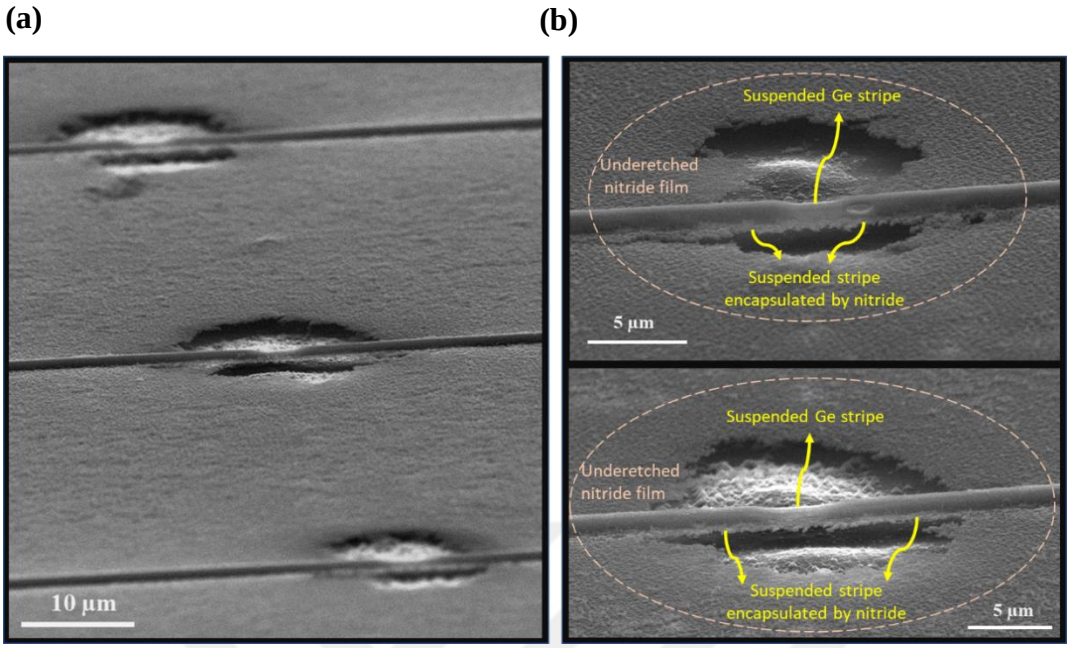

Figure 5.31 A tilted-stage high resolution SEM images of (a) 2.5-µm-long Ge MBs after the KOH etching, and (b) zoom-in views of two MBs exposed to different KOH etching, where the middle bright region of the stripe is suspended without any encapsulation, and darker regions of the suspended stripe on both sides are capped by the collapsed nitride film. The oval shown with the dashed line is used to indicate the region in which the nitride film is free-standing. The dimension of the oval is not scaled to the real dimension of the underetched nitride film.

5.2.2.2 Biaxially Tensile-Strained Ge Microstructures

Biaxially tensile-strained Ge microstructures are fabricated by the same processes of the previous uniaxial case where different sub-masks are used. For this purpose, Y-shape (4.1x4.1 μm^2 seed region with three 120° angled 2x50 μm^2 tails) is transferred to the Ge using the sub-mask 7 in Fig. 5.32, and the eth hole via the last photolithography for suspension of the Ge is defined by sub-mask N3 (three tails connected to a 6 µm diameter circle) in Fig. 5.33.

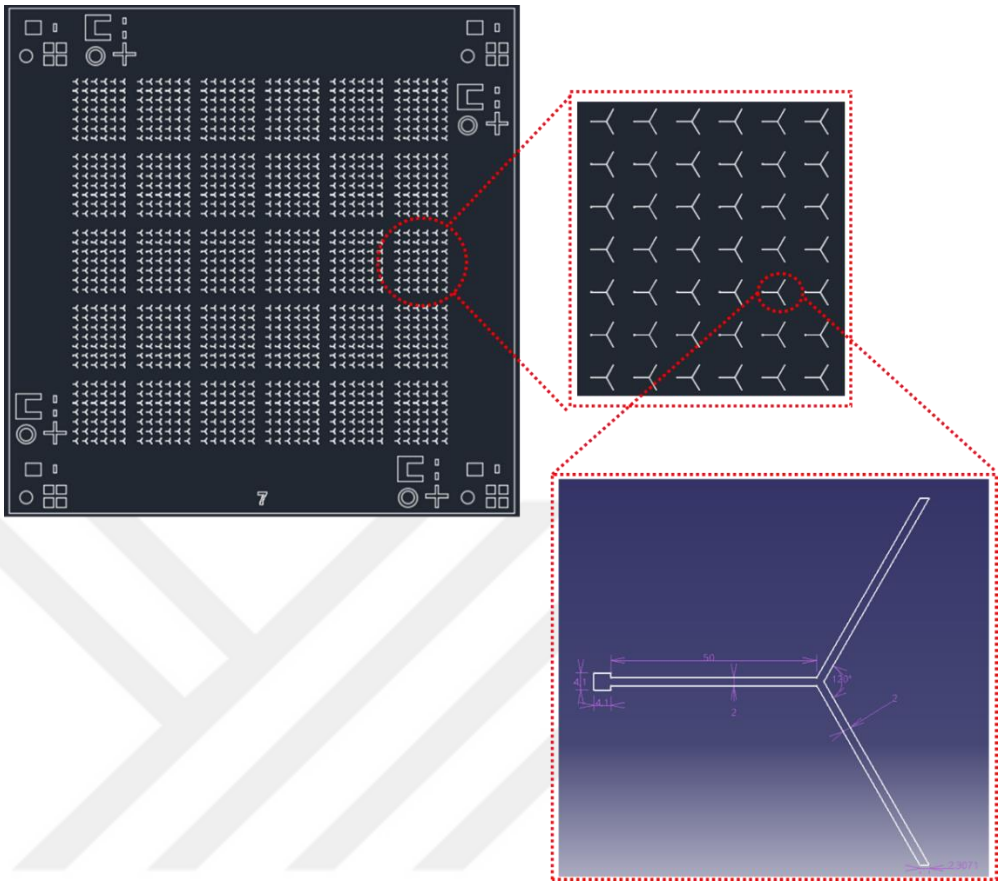

Figure 5.32 Mask layer 7 designed for Y-shaped Ge microstructures, consisting of a 4.1x4.1 μm^2 seed region with three 120° angled 2x50 μm^2 tails.

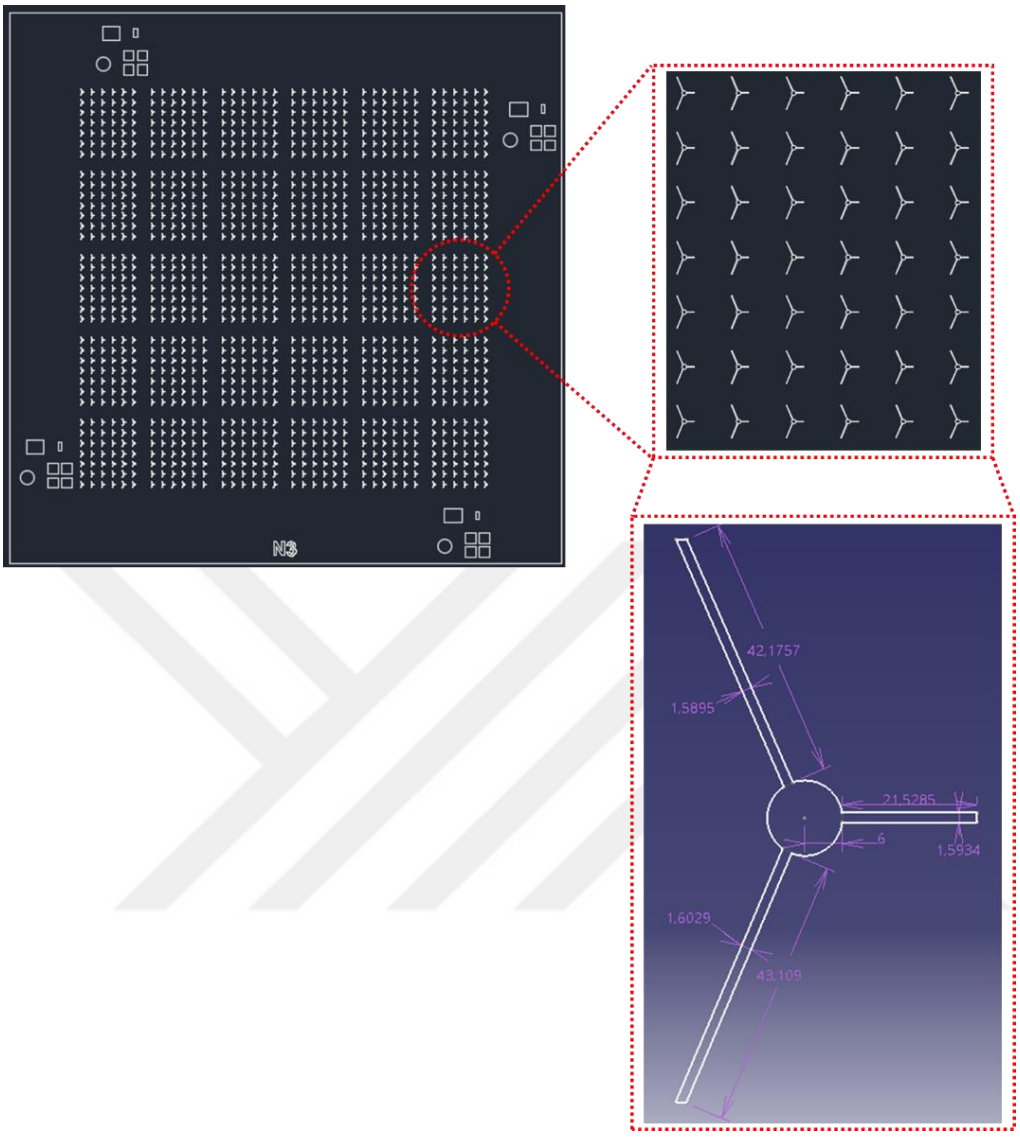

Figure 5.33 Mask layer N3 designed for etch holes of Y-shaped Ge microstructures, consisting of roughly three tails (1.6x42 μm^2, 1.6x43 μm^2 and 1.6x21.5 μm^2) connected to a 6 μm diameter circle.

SEM image of the Y-shaped Ge microstructures before the RTA and the last photolithography steps is shown in Fig. 5.34.

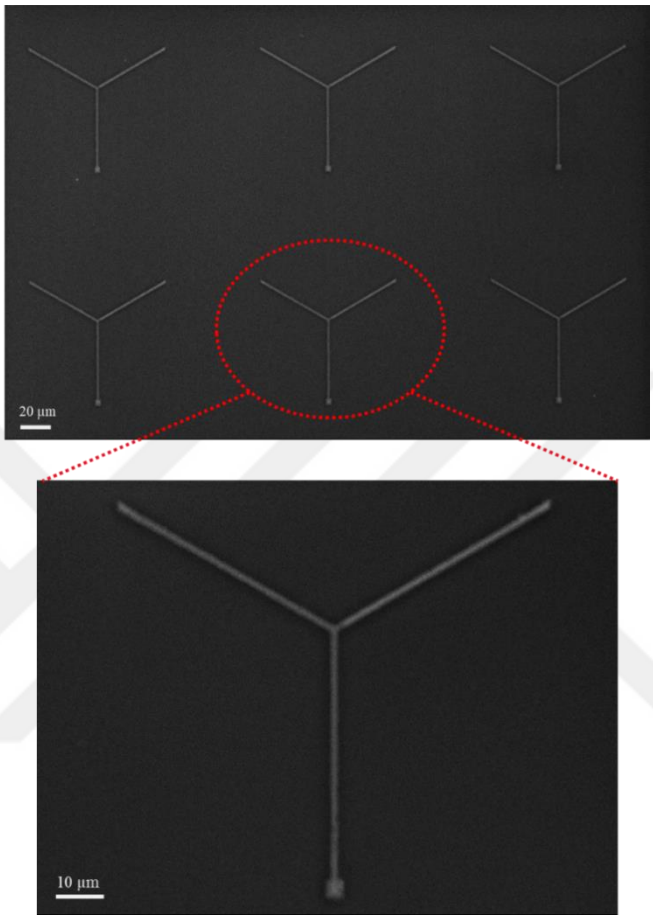

Figure 5.34 SEM image of Y-shaped Ge microstructures (top), zoom-in view (bottom).

After the etch hole patterns are transferred to the sample, wet etching steps of BOE and hot phosphoric acid are applied. If the wet etching is performed at an ideal duration, the successful structure with the predefined dimension of sub-mask layers 7 and N3 is observed in Fig. 5. 35(a). Otherwise, the shape is distorted, as seen in Fig. 5.35(b) with wider etch holes.

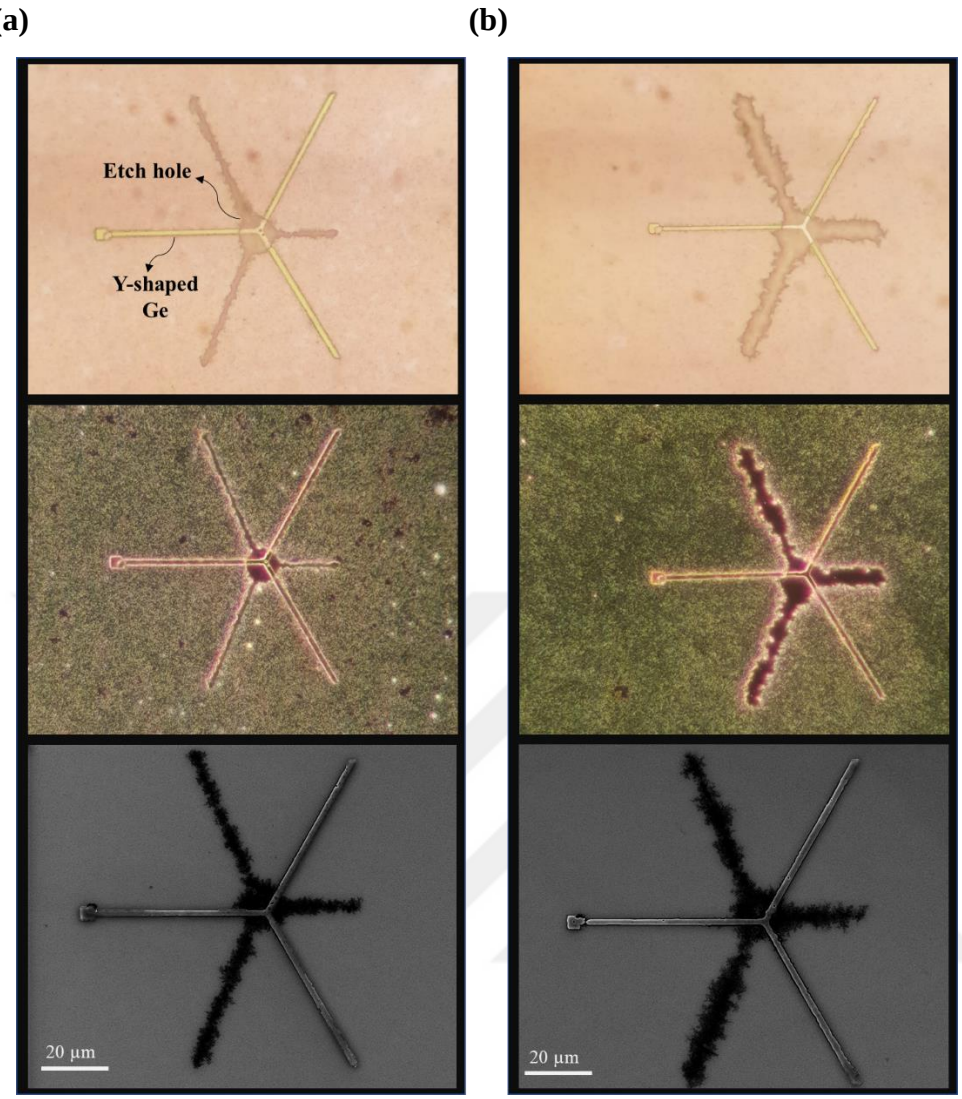

Figure 5.35 Bright field microscope, dark field microscope and SEM images of Y-shaped suspended Ge microstructures, respectively, with (a) an ideal dimension and (b) distorted ones.

The bending of the Y-shaped Ge microstructure in the middle region of the etch hole indicates that the structure is suspended as desired, as shown in Fig. 5.36.

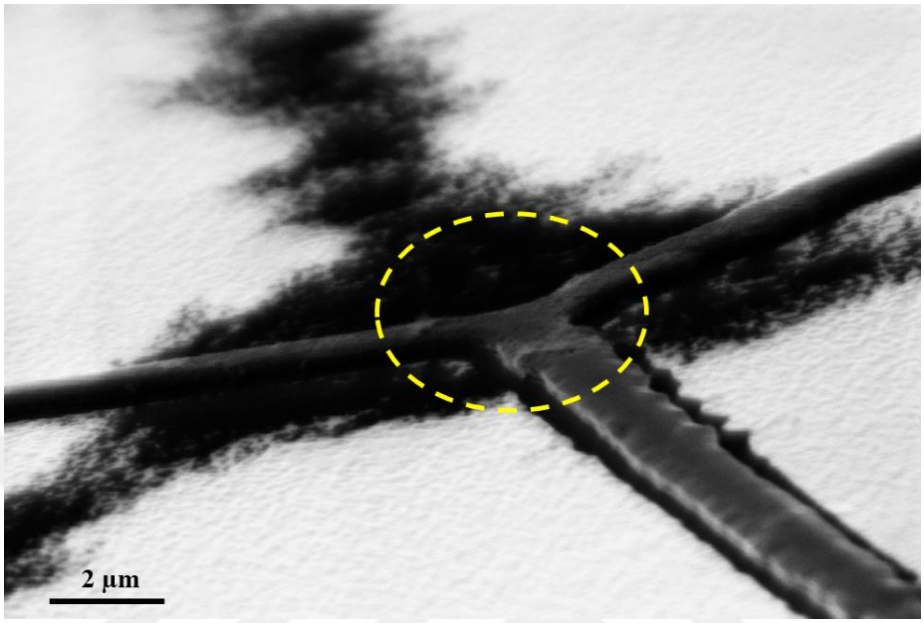

Figure 5.36 SEM image of the suspended Y-shaped Ge microstructure taken with 75° tilt angle.

However, it is realized that applied last BOE to remove oxide undesirably also etches the whole SiNx capping layer as inferred from the SEM image in Fig. 5.37. Here, Ge surface remained uncovered not only in the etch hole region but also in the tails of Ge, which indicates the sputtered poor quality SiNx. It is probably an oxidized SiNx (silicon oxynitride) due to higher base pressure of the sputtering system that could not be reduced somehow compared to the deposition condition of the one deposited SiNx layer on top of the uniaxial microstructures.

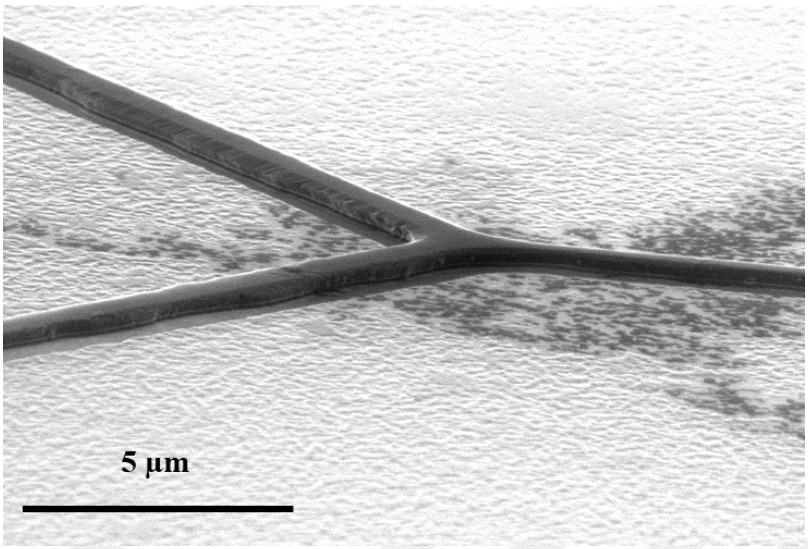

Figure 5.37 SEM image of Y-shaped Ge microstructure remained unintentionally uncoated after etching.

The sputtering environment should be away from factors that cause oxidation. As well as affecting the capping layer, oxide also has an influence on Ge quality. As shown in Fig. 5.38, Ge is observed in a perforated form (in another set of fabrication), unlike the Ge given in Fig. 5.37.

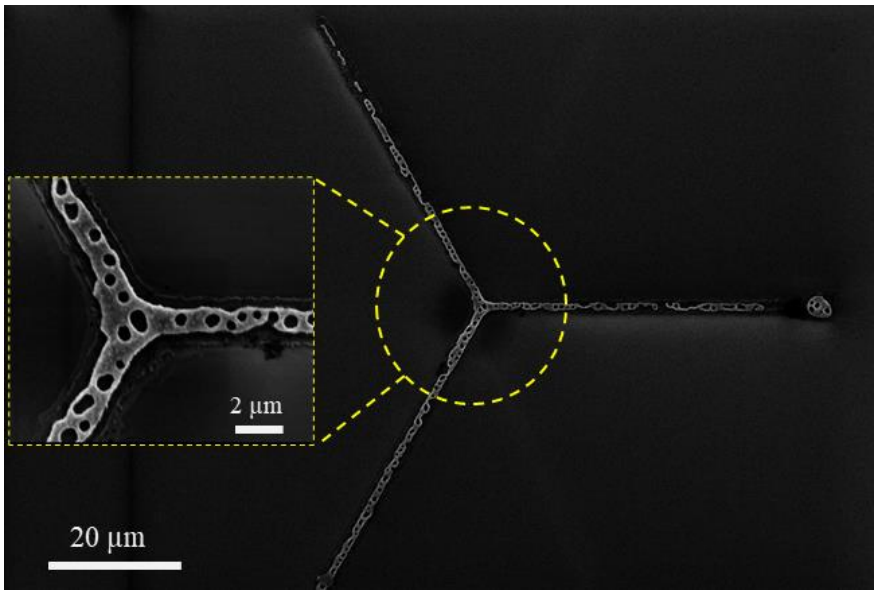

Figure 5.38 SEM image of perforated Y-shaped Ge microstructure with an inset of its zoom-in view.

The disrupted Ge layer can be due to the probability of Ge oxidation during the sputtering of Ge caused by potential impurities inside the chamber or the oxidized capping layer. Oxide, as an impurity inside the Ge layer, has a solubility of $1.3x10^{6}$ μm^{-3} at 1210.15 K [30]. It is claimed that volatile GeOx can be composed involuntarily if the masking layer on top of Ge includes oxygen, which results in partial loss of the Ge layer due to Ge islands formed via nucleation [38]. Another reason for the holey structure is that oxidized Ge is water soluble [33]. Some oxidized parts of the germanium layer are also unintentionally etched while stopping the wet etching processes with DI water.

Moreover, delamination of the capping layer can also be observed owning to the high-pressure environment in the sputtering chamber, as seen in Fig. 5.39. The film can peel off at the edges of the samples in Fig. 5.39(a) or from the whole surface in Fig. 5.39(b).

Figure 5.39 Peeling off behavior (a) at the edges of the samples, or (b) from the whole surface (right) and its optical microscope image (left).

This peeling-off behavior can also be stemmed from the adhesion problem in between two films. Adhesion energy decreases with increasing the released energy while atoms join together in the interface region [104]. Higher lattice mismatch results in a higher residual strain, boosting energy release. Therefore, the film peels off from its substrate after the reduction of adhesion energy. Accumulation of opening stress and shear stress can also reason for spalling the film surface [100]. These results show that the quality of the germanium and the cap layer exceedingly depends on the sputtering environment, which has an incredible effect of reversing the whole trend.

CHAPTER 6

CHARACTERIZATION OF GE MICROSTRUCTURES

The crystal orientation of Ge is analyzed by electron backscatter diffraction (EBSD) measurements. Strain-dependent emission properties of the Ge microstructures are characterized by micro photoluminescence (μ-PL) measurements, and micro-Raman spectroscopy measurements verify the amounts of the induced strain levels into the structures. PL setup and the results of three characterization tools are reported in this chapter.

6.1 Photoluminescence Measurements

The Micro-PL system is constructed as illustrated in Fig. 6.1. For that purpose, a 980 nm wavelength laser operated at the pulsed mode is used to excite the sample. The spot size of the laser incident on the sample is varied with the laser power. The laser is directed by two mirrors angled 45° (M1 and M2) and passed through a pinhole (P1) to filter unwanted components (noise) of the laser beam. After that, a beam splitter (B1) is mounted to the propagation path of the laser because here, a light source also merges into the system. Therefore, utilization of both sources simultaneously is made possible by including this beam splitter. Then, laser/light is passed through P2 and B2 followed by P3. The aim of using B2 is to direct laser/light (reflection) to the region where the sample is located and then direct the collected signals (transmission) towards a collimating lens (L1). A 52X reflecting objective (O1) is used to prevent chromatic aberrations and focus the laser to a single point. In other words, both the sample is excited, and radiation from the sample is collected through the reflective objective. A removable motorized camera is placed just in front of the filter (F1). Hence, the laser-excited sample surface is imaged simultaneously while both laser and light sources are on. Thus, the laser is easily

focused on the desired area. After the camera is removed, emitted PL signals are passed through the filter (F1) placed in front of the monochromator. F1 is used to avoid the second and higher harmonics of the 980-nm laser in the measured spectrum. The filter is a long-pass filter that allows passing just the wavelengths above 1400 nm. Then, passed signals are directed into a computer-controlled monochromator and detected in a range of 1400 nm to 2400 nm, where an Indium gallium arsenide (InGaAs) detector with a 2.4 μm cutoff is used. PL measurements are performed with a power-controlled laser operating at 980-nm and modulated at a frequency of 30 Hz. Since the laser is used in pulsed mode, a lock-in amplifier is included to detect of the emitted light where the time constant is arranged as 30 seconds, sensitivity is 1 mV/nA, and high reserve is used. The power of the laser is kept as small as possible to avoid laser-induced heating effect and adjusted to fit with the dimensions of the etched central region of the Ge microstructures considering the laser spot size that changes with the laser power. Measurements are conducted at room temperature. The measured PL spectra are corrected with respect to the responsivity of the detector and spectral response of the grating, fitting by Gaussian function.

As aforementioned in section 3.2.1, TM mode is the parallel polarized light; therefore, it cannot be detected by this PL system where only the vertically emitted photons are collected [98], [118]. In other words, the peaks in the PL spectrum are due to Gamma - first valence band (Γ-VB1) and Gamma - second valence band (Γ-VB2) transitions of TE mode.

(a)

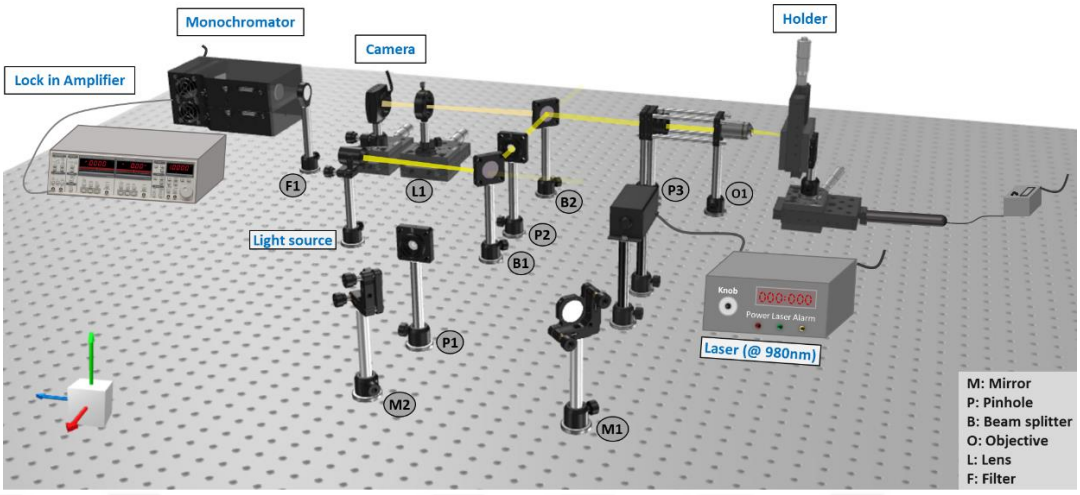

(b)

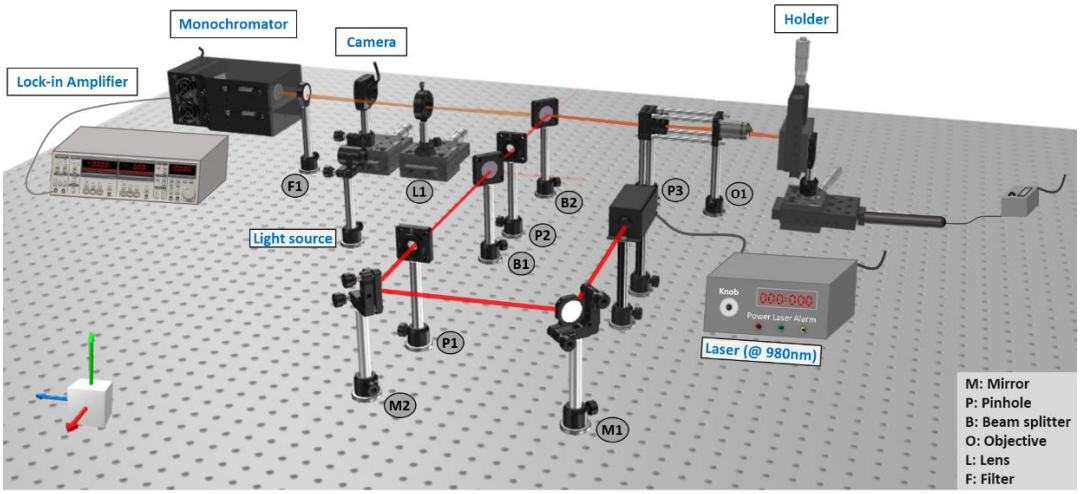

Figure 6.1 A schematic of the constructed micro-photoluminescence measurement system (a) with a light source on for imagining the sample, or (b) with laser on for collecting PL signals.

6.2 EBSD and Raman Measurements

EBSD and Raman measurements are conducted in METU Central Laboratory. Raman spectra are obtained with Renishaw inVia Raman microscope where the etch hole is excited by a 532 nm laser-focused through 100X objective. The spot size is roughly 1.1 µm. Therefore, the strain introduced into the middle of the suspended

bridges can be extracted via these measurements. The system is calibrated using a reference Si wafer at 520 cm^{-1}. Laser power is kept as small as possible (i.e., 50 µW) to avoid laser-induced heating effects, which can cause a shift in the emission wavelength and may be misinterpreted between the strain induction and the shift due to heating.

6.3 Measurement Results and Discussion

6.3.1 Uniaxially Tensile-Strained Ge Microstructures

First of all, EBSD measurements are performed to verify the formation of the single crystalline Ge stripes. For that purpose, the capping layers, SiO_2 and SiNx, are completely etched by wet etching processes of BOE and H_3PO_4 at 160 °C, respectively. Thus, the sample is prepared to be suitable for EBSD measurement. Figure 6.3 shows the EBSD analysis of 250-µm-long Ge stripe, which demonstrates the crystallization of the whole Ge stripe in the (100) direction imitating the crystal orientation of the underlying Si substrate as desired.

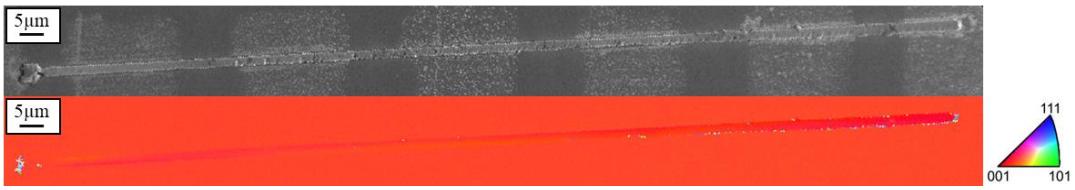

Figure 6.2 EBSD analysis of the Ge stripe microstripe shown together with the SEM image of the same region, indicating crystallized 250-µm-long Ge stripe in the (100) direction via the red color of the orientation color code triangle.

After ensuring the crystallization of the stripes in the (100) direction, the samples are capped with nitride and oxide layers. The last photolithography step is performed on the masking oxide layer to define 4x20 μm^2 etch holes. After etching processes as described in detail in chapter 5, a portion of the stripe is suspended, and Ge microbridge structure is obtained. Dimension of etch hole can be varied by adjusting

the first BOE etching duration. The length of the microbridge is made wider when 90-seconds-long BOE etching is applied instead of the etching duration of 30-seconds (for nominal dimensions). This situation results in 20-μm-long and 4-μm-long single-crystalline Ge MBs, respectively; after that, the subsequent hot phosphoric acid and last BOE etching processes are applied for the tensile strain induction into the MBs.

The strain-dependent emission properties of these two MBs are characterized with a power-adjustable PL spectroscopy measurements, and the amounts of the induced strain levels into the MBs are verified by the Raman spectroscopy measurements, shown in Fig. 6.3. PL spectra of the MBs are shown in Fig. 6.3(a) and Fig. 6.3(b) with dark-field microscope images in the insets. The laser's spot size is arranged to be roughly 20 μm where the average power of the laser incident on the sample is adjusted to 2 mW, which means that the full length of 20-μm-long Ge MB is pumped while for 4-μm-long Ge MB, the bridge together with the portion of the microstripe capped by the underetched stressor film is pumped. PL spectra of MBs are fitted by Gaussian peaks where 20-μm-long MB is fitted with a single Gaussian peak in Fig. 6.3(a), and 4-μm-long MB is fitted by three Gaussian peaks (plotted with the dotted lines) in Fig. 6.3(b). To estimate the amount of the tensile strain inducted into MBs, the peak wavelengths of the Gaussian fits are fitted onto the strain-dependent bandgap energy curves calculated by Nam et al. [117] using the deformation potential theory for the Ge uniaxially strained in (100) direction. The corresponding strain levels to the peak energies of red, grey and blue fitting curves are acquired as 1.4% (blue symbol), 0.5% (grey symbol) and 1.9% (red symbols), as demonstrated in Fig. 6.3(c). While the peak position of the PL spectrum measured from 20-μm-long Ge MB corresponds to a strain level of 1.4%, the emission for 4-μm-long Ge MB is not only collected from a 1.9%-strained region but also detected from a region with a strain level of 0.5%. The short-wavelength-emission peak resulting in 0.5% strain is predicted to originate from the part of the Ge MB encapsulated by the nitride film, whereas the amount of strain location in the suspended and uncapped region of the Ge MB is 1.9%. This longer wavelength emission peak is due to the transitions

between the Gamma - first valence band (Γ-VB1) and Gamma - second valence band (Γ -VB2) of TE mode. The transition with light holes (Γ-VB1) is stronger than the transition with heavy holes (Γ-VB2), and in fact, the longer wavelength emission is dominated by the transitions between the electrons of the Γ valley of the conduction band and the light holes of TM mode, not TE mode. However, the transitions between the electrons of the Γ-VB2 appear stronger than the Γ-VB1, as shown in Fig. 6.3(b), because the TM mode is undetectable with our setup. Therefore, the emission corresponding to the shorter wavelength, which is mostly due to the transitions between the electrons of the Γ valley of the conduction band and the heavy holes, appears to be stronger than the other peak. The mostly TM-polarized G-VB1 emission peak could not be resolved in the emission spectrum of the 1.4%-strained bridge because the detectable TE component emission arising from such transitions becomes more favorable with increasing strain, as observed in earlier work, as well [98]. On the other hand, the strain-induced PL enhancement [117] could not be observed because of the difference between the lengths of the strained regions of the stripes; it is 20 μm for the 1.4% strained structure, which is the same as the spot size of the pump, and only 4 μm for the 1.9% strained structure. It would be possible to observe the strain-induced PL enhancement by reducing the spot size of the pump down to 4 μm. However, the only way to reduce the spot size of the pump laser down to 4 μm was to reduce its average power at the same time, which resulted in the pump power to be insufficient for yielding detectable PL.

After the PL measurements, the micro-Raman spectroscopy measurements are performed on these two MBs, which are also in very good agreement with the results obtained from the PL analysis. The measured Raman shifts are compared with the one obtained from the Raman shift of bulk Ge at 301.3 cm^{-1}, and the uniaxial strain values are calculated as 1.5% and 1.9% for the 20-μm-long and 4μm-long MBs using the relationship given in Ref. [132] where the Raman shifts are 299.0 cm^{-1} and 298.35 cm^{-1}, respectively as shown in Fig. 6.3(d).

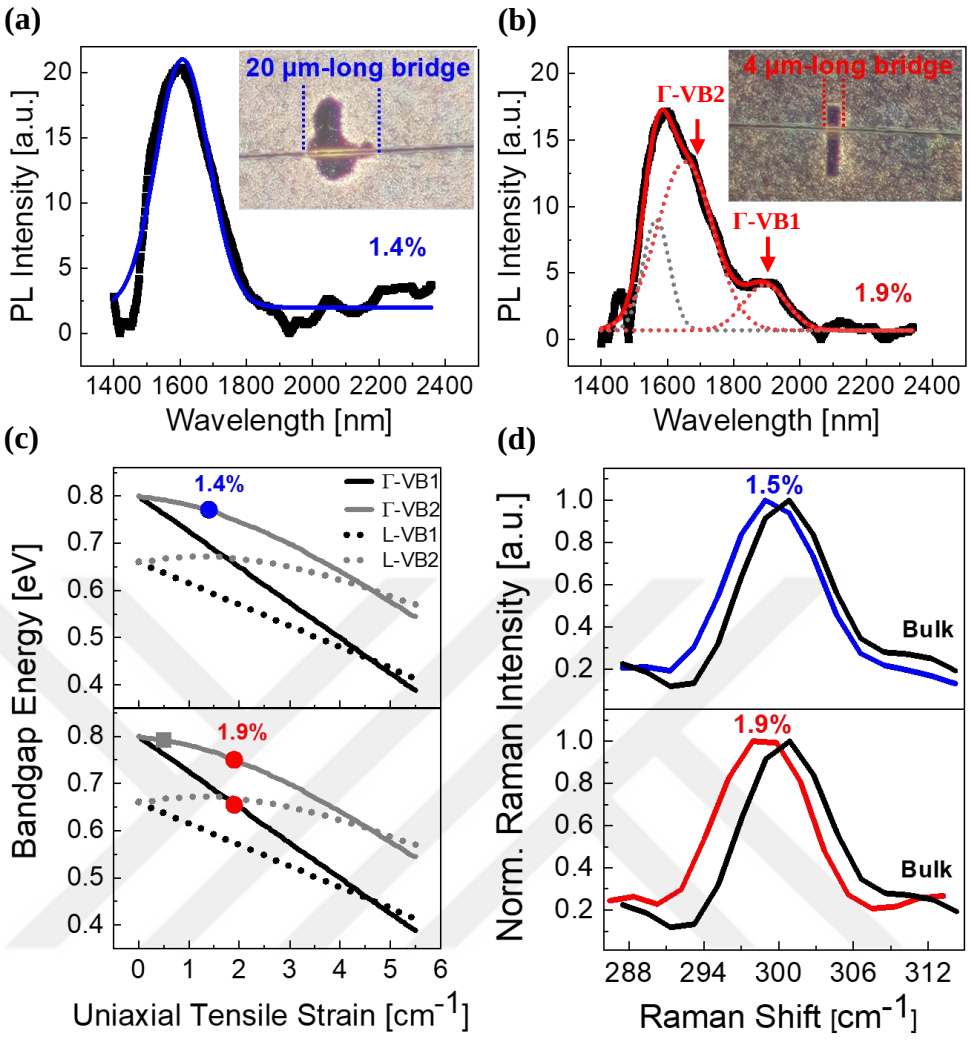

Figure 6.3 Strain analysis of Ge MBs by PL and Raman spectroscopy measurements. (a) PL spectra of Ge 20-μm-long and (b) 4-μm-long single-crystalline Ge MBs (shown with the black symbols) fitted with Gaussian peaks (i.e., the dotted lines colored blue, red and grey). The insets show the dark field microscope images of the corresponding microstripes. (c) The peak wavelengths of the Gaussian fits are fitted onto the strain-dependent bandgap energy curves [117], and the corresponding strain levels of 1.4% (blue symbol), 0.5% (grey symbol) and 1.9% (red symbols) are acquired. (d) Raman spectra colored with the same corresponding colors demonstrate 1.5% (solid blue line) and 1.9% (solid red line) strain levels in comparison with the measured Raman spectrum of the bulk Ge (solid black line).

These PL and Raman spectroscopy results are also consistent with the results obtained from the FEM simulations constructed by the exact dimensions with MBs as shown in Fig. 6.4, where the volume-averaged strain on Ge MBs is visualized with the strain color legend. The unknown parameter of $L_{Underetcing}$ (in Fig. 4.1) is predicted by FEM simulations. 1.95% and 1.4% strain values are obtained when the underetching lengths are arranged as 44 µm and 108 µm for 4-µm-long and 20-µm-long MBs, respectively. Here, the resulting portion of underetched nitride film is larger for longer MB, which fits with experiments. For the same duration of the last BOE etching, larger $L_{Underetcing}$ is observable because the solvent attacks the underlying oxide passing through a wider opening. Besides, The insets showing the strain values along 20-µm-long lines passing through the middle of the corresponding stripes validate the observation of the strain nonuniformity in the PL spectrum of the 4-µm-long bridge as compared to 20-µm-long bridge, when PL is measured with a pump spot size of 20 µm.

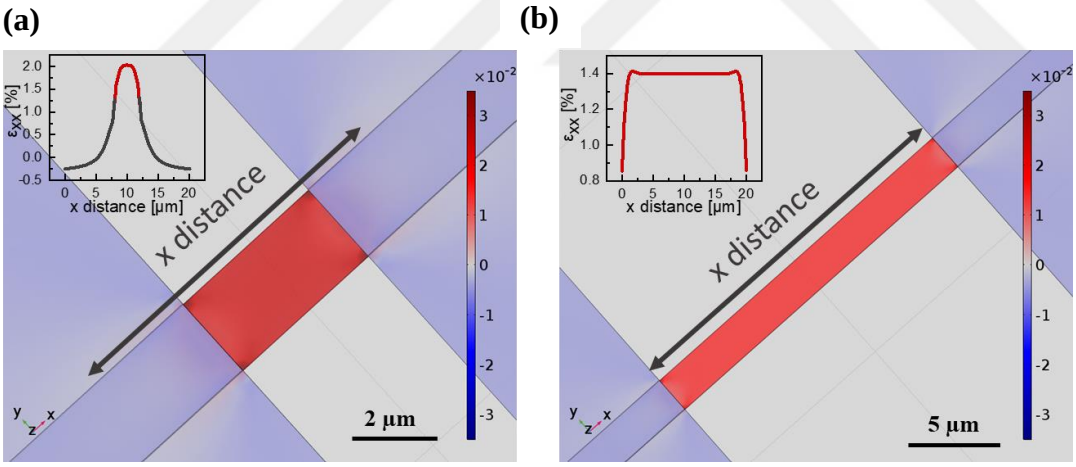

Figure 6.4 Finite element method (FEM) simulation results of (a) 4-µm-long and (b) 20-µm-long Ge MBs with 44-µm-long and 108-µm-long underetched nitride films ($L_{Underetcing}$) resulting in 1.95% and 1.4% volume-averaged strain on Ge MBs, respectively. The corresponding 20-µm-long line strain graphs along the stripe axis of MBs are given in the insets of strain profiles visualized with a color legend.

The 2.5-μm-long Ge MBs exposed KOH etching are also characterized. Strain enhancement is observed with both PL and Raman spectroscopy measurements in Fig. 6.5. Three different KOH exposure durations that are 30-, 60- and 90-seconds are investigated. PL spectra of these MBs are given in Fig. 6.5(a) with multiple Gaussian peak fits (shown with dotted lines), where the average laser power incident on the structure is increased up to 5 mW to provide sufficient pump power to these shorter bridges which brings about the enlargement of the pump spot size to 30 μm. The peak wavelengths of the Gaussian fits are fitted onto the strain-dependent bandgap energy curves using the same colors as the corresponding fitting curves to acquire uniaxial strain levels, as seen in Fig. 6.5(b). The grey fitting curves resolve the emission due to the nitride-encapsulated region of the Ge stripe; the colored peaks correspond to the strain localized region(2.5-μm-long suspended region of the microstripe), where no encapsulation is present. A red shift in wavelengths of both Γ-VB1 and Γ-VB2 transitions are obtained, as shown in Fig. 6.5(a), which is the sign of strain enhancement. The strain level increases from 2.3% to 3.4% with increasing the KOH duration by 60 seconds. The reason is that a much larger portion of nitride film around the bridge collapses, as shown in Fig. 6.6(a) and its underetch length increases, which in turn enables the larger strain transmission from the stressor to the middle region of the MB (i.e., strain localization). Strain uniformity arisen from collapse regions causes broadening in the PL spectra. Raman spectroscopy measurement results obtained from these MBs in Fig. 6.5(c) are also in very good agreement with the PL measurement results. The slight difference between strain levels obtained from PL and Raman measurements is originated from the shorter-wavelength laser used in the Raman measurements. That causes the detection of the strain close to the top surface of the bridge, which reaches the maximum strain value as observed in the simulations, as well. Same colors as the corresponding PL spectra are used in Raman graphs, where 2.3%, 3% and 3.5% strain levels are obtained from the Raman shifts of 297.71cm^{-1}, 296.67cm^{-1} and 295.89cm^{-1}, respectively using the relationship given in Ref. [132].

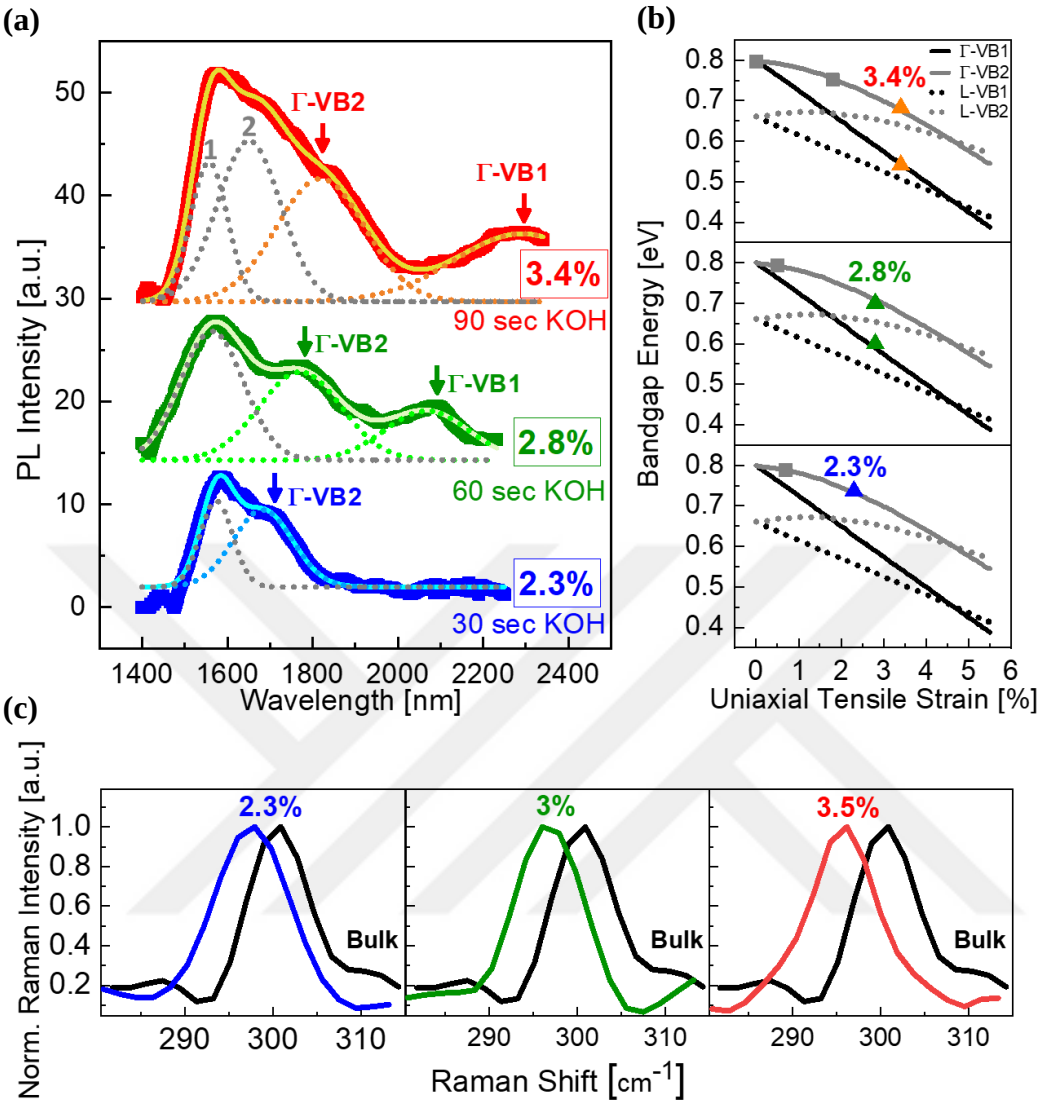

Figure 6.5 Strain analysis of 2.5-µm-long Ge MBs exposed KOH etching process. (a) PL spectra of three 2.5-µm-long MBs differing with KOH exposure time, 30-, 60- and 90-seconds, fitted Gaussian peaks (i.e., the dotted lines colored blue, green, red and common grey). (c) The peak wavelengths of the Gaussian fits are fitted onto the strain-dependent bandgap energy curves [117], the corresponding maximum strain levels are obtained as 2.3% (blue symbol), 2.8% (green symbols), and 3.4% (red symbols) for 30-, 60- and 90-seconds KOH exposure time, respectively. (c) Raman spectra colored with the same corresponding colors demonstrate 2.3% (solid blue line), 3% (solid green line) and 3.5% (solid red line) strain levels in comparison with the Raman spectrum of the bulk Ge (solid black line).

PL and Raman measurement results are supported by FEM simulations, as illustrated in Fig. 6.6(b). The simulated structures are constructed using the dimensions of the bridges shown in the SEM images in Fig. 6.6(a). The only unknown dimension, which is the amount of the underetched portion of the nitride film ($L_{Underetcing}$) is predicted as 69-μm-long and 90-μm-long; so that the resulting strain in the middle region of the MB is calculated as 3% and 3.5% (as already determined by PL and Raman measurements) for the structure etched with KOH for 60- and 90-seconds, respectively, as demonstrated in Fig. 6.6(b). Additionally, the strain profiles along 30-μm-long lines (i.e., the spot size of pump laser) passing through the middle of the stripes along their axes (x-axes) are given in the insets in Fig. 6.6(b). These line profiles verify the nonuniformity in strain distribution, reaching maximum at the center of the bridge and gradually decreasing and becoming even compressive in the part of the stripe capped by the stressor. Therefore, the PL spectra measured from samples exposed to KOH for 60- and 90-seconds are fitted with broader Gaussian peaks. The grey colored fitting curves in the PL spectrum resulting in 3.4% strain in Fig. 6.5(a) are predicted to originate mainly from the regions indicated as 1 and 2 in the corresponding SEM image in Fig. 6.6(a) based on the calculated strain profile shown in the inset in Fig. 6.6(b). As expected, the area closer to the middle region of MB has a larger strain than the far regions due to strain localization in the middle. Therefore, region 2 has a large strain gradient potentially averaging to 2% giving rise to the peak numbered as 2 in Fig. 6.5(a), while strain in region 1 has a much smaller gradient with an average strain of around 0% resulting in the emission peak numbered as 1. It is important to note that such strain nonuniformities existing in the fabricated microstructures were observed in the measured PL spectra due to the large spot size of the pumping laser, since the spot size of the pump couldn't be reduced down to few microns without sacrificing the pump power. Nevertheless, well-resolved emission peaks are demonstrated from 2.5-μm-long Ge MBs that apparently red-shifts and getting enhanced with increasing KOH exposure time of the structures, providing clear evidence of increasing strain.

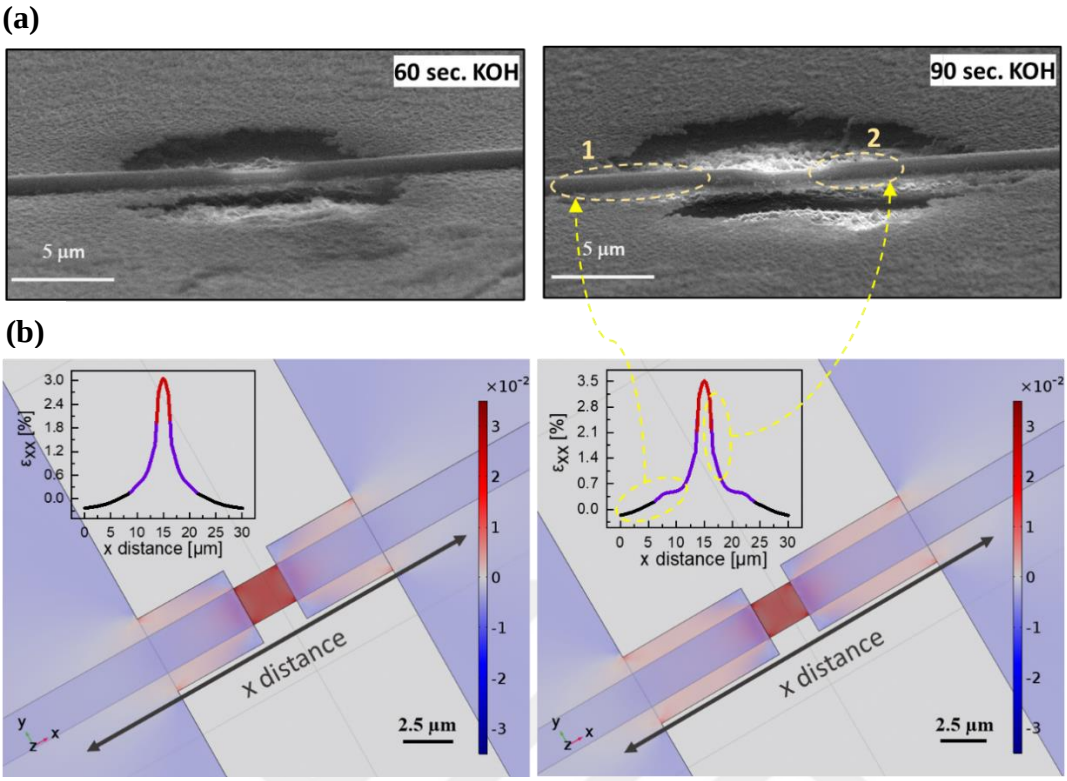

Figure 6.6 (a) SEM images of 60- and 90-seconds KOH applied Ge MBs, where the nitride film around the bridge is collapsed, and using the extracted dimensions from the SEM images (b) the corresponding FEM simulations are constructed, resulting in 3% and 3.5% with 69-µm-long and 90-µm-long underetched nitride films ($L_{Underetcing}$) for 60- and 90-seconds exposure time, respectively. The corresponding 30-µm-long line strain graphs along the stripe axes of MBs are given in the insets of strain profiles visualized with a color legend.

6.3.2 Biaxially Tensile-Strained Ge Microstructures

EBSD analysis is performed to examine the crystal orientation of biaxially tensile-strained Ge microstructures whose capping layers are completely removed by wet etching processes to be suitable for EBSD measurement conditions. Crystallization of the Y-shaped Ge microstructure is obtained as poly-crystalline in Fig. 6.7. One of the reasons is that although seed-stripe are aligned on top of each other, the oxide in the seed region may not be completely etched, and the residues of the oxide here may

prevent the single crystal formation. Another reason is the low quality of the capping layer that is oxidized SiNx (silicon oxynitride). Therefore, during the RTA process, liquid Ge could not be held effectively into the defined shape, disrupting the formation of a single crystal.

As a result, it is impossible to extract its strain level where Raman spectroscopy and PL measurements depend on the crystal orientation of the structure that should be single-crystalline. Therefore, PL and Raman measurements could not be performed for this structure.

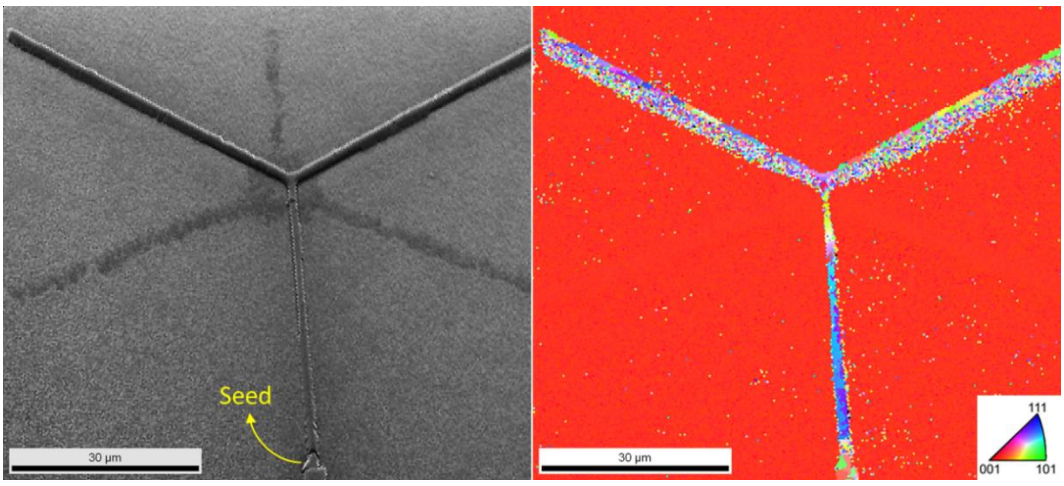

Figure 6.7 EBSD analysis of Y-shaped Ge microstructure (right) given with SEM image of the corresponding area (left), indicating poly-crystallized Y-shaped Ge microstructure.

CHAPTER 7

CONCLUSIONS AND OUTLOOK

In this thesis, both uniaxially and biaxially tensile-strained Ge microstructures are investigated. The expected fabrication steps could not be achieved for the biaxially strained Ge microstructures. Therefore, the proposed strain levels could not be obtained. For the uniaxial case, tensilely-strained, single-crystalline germanium microbridges are fabricated with very practical, cost-effective and easy-to-apply CMOS-compatible fabrication processes. The fabricated microstructures demonstrate room-temperature light emission, paving the way for the potential demonstration of monolithically integrated infrared Ge laser. Deposition of the film layers -other than a thin layer of thermally grown oxide- is performed by sputtering, which is a straightforward, low-cost and environmentally friendly physical vapor deposition method operating at room temperature. It is demonstrated a single rapid thermal annealing process utilized in the LPE technique converts the sputtered amorphous Ge into the single crystalline form in the (100) direction while at the same time transforming the capping layer (i.e., silicon nitride film) into a stressor material, where the fabrication is based on the photolithography and wet etching processes. EBSD measurement verifies the (100) crystal orientation of the whole Ge stripe. Following that, the photolithography and wet etching processes form several Ge MBs as well as the induction of uniaxial tensile strain into the single-crystalline Ge microstripes. The amount of strain is controlled and tuned by simply changing the wet etching process's type and duration. Raman spectroscopy and Photoluminescence measurements are performed at room temperature to characterize the amount of the induced strain levels and strain-dependent emission properties of MBs, respectively. Two different MB structures are formed with and without the KOH exposure conditions where the first BOE etching duration is varied as well, which is diversified by the underetched portion of the stressor layer and

studied within themselves. Unexposed 20-μm-long and 4-μm-long single-crystalline Ge MBs result in about 1.4% and 1.9% strain; the KOH exposed 2.5-μm-long Ge MBs exhibit the strain levels of approximately 2.3%, 2.8% and 3.4% according to the exposure time of 30-, 60- and 90-seconds, respectively. Room-temperature PL spectra measured from the MBs that are common in length but differ in terms of the underetched portion of the stressor layer demonstrate red-shift and enhancement with increasing strain. These observations are verified via Raman spectroscopy measurements, as well as the FEM simulations.

It is important to note that the fabrication method introduced in this work is compatible with the development of uniaxially strained, doped Ge microstructures, as well. More specifically, an ion implantation process added to our fabrication flow would result in the development of moderately doped Ge microstructures that can be strained up to 3.5%, forming a material platform providing gain. Therefore, the methods introduced in this work can be employed to demonstrate an on-chip infrared Ge laser, where cost-inefficient GOI wafers are not required since a single RTA process both crystallizes Ge and enables tensile strain induction in Ge that is realized via a room-temperature-operated deposition technique as opposed to the more complicated chemical vapor deposition methods.

As future work, the fabrication steps of the Y-shaped Ge microstructures will be repeated with a high-quality capping layer after ensuring that the oxide is completely removed from the seed region. Thus, Ge will be stay covered by silicon nitride stressor layer on top and sides even after the wet etching processes like in the case of uniaxially strained Ge MBs, which will result in a high level of the biaxial strain. This assumption can be inferred from the FEM simulations that verify PL and Raman measurements as observed in the uniaxial case. Furthermore, different stressor layers, namely silicon dioxide (SiO_2), titanium dioxide (TiO_2) and zinc oxide (ZnO) will be examined for the quantity of the transferring strain to Ge microstructures larger than the strain levels transferred by the nitride layer.

REFERENCES

[1] A. M. Kuhlmann, “The Second Most Abundant Element in the Earth’s Crust,” *Jom*, vol. 15, no. 7, pp. 502–505, 1963, doi: 10.1007/bf03378936.

[2] R. Soref, “The past, present, and future of silicon photonics,” *IEEE J. Sel. Top. Quantum Electron.*, vol. 12, no. 6, pp. 1678–1687, 2006, doi: 10.1109/JSTQE.2006.883151.

[3] B. Jalali and S. Fathpour, “Silicon photonics,” *J. Light. Technol.*, vol. 24, no. 12, pp. 4600–4615, 2006, doi: 10.1109/JLT.2006.885782.

[4] D. J. Paul, “Si/SiGe heterostructures: from material and physics to devices and circuits,” *Semicond. Sci. Technol.*, vol. 19, no. 10, pp. 75–108, 2004, doi: 10.1088/0268-1242/19/10/R02.

[5] T. Tsuchizawa, K. Yamada, H. Fukuda, T. Watanabe, J. Takahashi, and M. Takahashi, “Microphotonics Devices Based on Silicon Microfabrication Technology,” *IEEE J. Sel. Top. QUANTUM Electron.*, vol. 11, no. 1, pp. 232–240, 2005, doi: 10.1109/JSTQE.2004.841479.

[6] G. K. Celler and S. Cristoloveanu, “Frontiers of silicon-on-insulator,” *J. Appl. Phys.*, vol. 93, no. 9, pp. 4955–4978, 2003, doi: 10.1063/1.1558223.

[7] K. Yamada, T. Shoji, T. Tsuchizawa, T. Watanabe, J. Takahashi, and S. Itabashi, “Silicon-wire-based ultrasmall lattice filters with wide free spectral ranges,” *Opt. Lett.*, vol. 28, no. 18, p. 1663, 2003, doi: 10.1364/ol.28.001663.

[8] C. Batten, C. W. Holzwarth, H. I. Smith, J. L. Hoyt, F. X. Ka, and R. J. Ram, “BUILDING MANY-CORE PROCESSOR-TO-DRAM NETWORKS WITH MONOLITHIC CMOS SILICON PHOTONICS,” *IEEE Comput. Soc.*, pp. 8–21, 2009, doi: 10.1109/MM.2009.60.

[9] N. L. Rowell, J. P. Noël, D. C. Houghton, and M. Buchanan, “Electroluminescence and photoluminescence from Si1x Ge x alloys,” *Appl. Phys. Lett.*, vol. 58, no. 9, pp. 957–958, 1991, doi: 10.1063/1.104454.

[10] S. S. Iyer and Y. H. Xie, “Light Emission from Silicon,” *Science (80-.).*, vol. 260, no. 5104, pp. 40–46, Apr. 1993, doi: 10.1126/science.260.5104.40.

[11] H. J. J. Yeh and J. S. Smith, “Fluidic Self-Assembly for the Integration of GaAs Light-Emitting Diodes on Si Substrates,” *IEEE PHOTONICS Technol. Lett.*, vol. 6, no. 6, pp. 706–708, 1994, doi: 10.1109/68.300169.

[12] M. Fujii, M. Yoshida, Y. Kanzawa, S. Hayashi, and K. Yamamoto, “1.54 μm photoluminescence of Er3+ doped into SiO2 films containing Si nanocrystals: Evidence for energy transfer from Si nanocrystals to Er3+,” *Appl. Phys. Lett.*, vol. 71, no. 9, pp. 1198–1200, 1997, [Online]. Available: http://ojps.aip.org/aplo/aplcr.jsp.

[13] H. S. Han, S. Y. Seo, and J. H. Shin, “Optical gain at 1.54 μm in erbium-doped silicon nanocluster sensitized waveguide,” *Appl. Phys. Lett.*, vol. 79, no. 27, pp. 4568–4570, 2001, doi: 10.1063/1.1419035.

[14] X. Sun, J. Liu, L. C. Kimerling, and J. Michel, “Room-temperature direct bandgap electroluminesence from Ge-on-Si light-emitting diodes,” *Opt. Lett.*, vol. 34, no. 8, p. 1198, 2009, doi: 10.1364/ol.34.001198.

[15] D. J. Lockwood, “Light emission in silicon nanostructures,” *J Mater Sci Mater Electron*, vol. 20, pp. 235–244, 2009, doi: 10.1007/s10854-007-9552-6.

[16] M. L. Cohen and T. K. Bergstresser, “Band Structures and Pseudopotential Form Factors for Fourteen Semiconductors of the Diamond and Zinc-blende Structures,” *Phys. Rev.*, vol. 141, no. 2, pp. 789–796, 1966, doi: https://doi.org/10.1103/PhysRev.141.789.

[17] F. Zhang, V. H. Crespi, and P. Zhang, “Prediction that Uniaxial Tension along <111> Produces a Direct Band Gap in Germanium,” *Phys. Rev. Lett.*, vol. 102, no. 156401, pp. 1–4, 2009, doi: 10.1103/PhysRevLett.102.156401.

[18] J. Menéndez and J. Kouvetakis, “Type-I Ge⁄Ge1−x−ySixSny strained-layer heterostructures with a direct Ge bandgap,” *Appl. Phys. Lett.*, vol. 85, no. 7, pp. 1175–1177, 2004, doi: 10.1063/1.1784032.

[19] J. Liu *et al.*, “Tensile-strained, n-type Ge as a gain medium for monolithic laser integration on Si,” *Opt. Express*, vol. 15, no. 18, p. 11272, 2007, doi: 10.1364/oe.15.011272.

[20] D. V. Freck and J. Wakefield, “Gamma-Ray Spectrum obtained with a Lithium-drifted p-i-n Junction in Germanium,” *Nature*, vol. 193, no. 4816, p. 669, 1962, doi: 10.1038/193669a0.

[21] R. R. Moskalyk, “Review of germanium processing worldwide,” *Miner. Eng.*, vol. 17, no. 3, pp. 393–402, 2004, doi: 10.1016/j.mineng.2003.11.014.

[22] M. E. Straumanis and E. Z. Aka, “Lattice Parameters, Coefficients of Thermal Expansion, and Atomic Weights of Purest Silicon and Germanium,” *J. Appl. Phys.*, vol. 23, no. 3, pp. 330–334, 1952, doi: 10.1063/1.1702202.

[23] O. L. Krivanek, S. Isoda, and K. Kobayashi, “Lattice imaging of a grain boundary in crystalline germanium,” *Philos. Mag.*, vol. 36, no. 4, pp. 931–940, 1977, doi: 10.1080/14786437708239768.

[24] F. Herman, “Calculation of the Energy Band Structures of the Diamond and Germanium Crystals by the Method of Orthogonalized Plane Waves,” *Phys. Rev.*, vol. 93, no. 6, pp. 1214–1225, 1954, doi: 10.1103/PhysRev.93.1214.

[25] S. Kumar, P. Kumar, K. Kumari, and S. Avasthi, “Optimization of controlled two-step liquid phase crystallization of Ge-on-Si,” in *2018 4th IEEE*

International Conference on Emerging Electronics, ICEE 2018, 2018, pp. 1–4, doi: 10.1109/ICEE44586.2018.8937975.

[26] Z. Liu *et al.*, "Lateral growth of single-crystal Ge on insulating substrate using amorphous Si seed by rapid melting growth," *Thin Solid Films*, vol. 597, pp. 39–43, 2015, doi: 10.1016/j.tsf.2015.11.025.

[27] J. R. Chelikowsky and M. L. Cohen, "Nonlocal pseudopotential calculations for the electronic structure of eleven diamond and zinc-blende semiconductors," *Phys. Rev. B*, vol. 14, no. 2, pp. 556–582, 1976, doi: 10.1103/PhysRevB.14.556.

[28] G. Pizzi, M. Virgilio, and G. Grosso, "Tight-binding calculation of optical gain in tensile strained [001]-Ge/SiGe quantum wells," *Nanotechnology*, vol. 21, no. 5, 2010, doi: 10.1088/0957-4484/21/5/055202.

[29] J. Liu *et al.*, "Ge-on-Si optoelectronics," *Thin Solid Films*, vol. 520, no. 8, pp. 3354–3360, 2012, doi: 10.1016/j.tsf.2011.10.121.

[30] Otfried Madelung, "Semiconductors: Group IV Elements and III-V Compounds," in *Springer-Verlag Berlin Heidelberg*, 1991, pp. 28–39.

[31] J. Liu, X. Sun, L. C. Kimerling, and J. Michel, "Direct-gap optical gain of Ge on Si at room temperature," *Opt. Lett.*, vol. 34, no. 11, p. 1738, 2009, doi: 10.1364/ol.34.001738.

[32] H. R. Huff, "From The Lab to The Fab: Transistors to Integrated Circuits," vol. 3, no. October, pp. 3–39, 2003, doi: 10.1063/1.1622451.

[33] D. P. Brunco *et al.*, "Germanium: The Past and Possibly a Future Material for Microelectronics," *ECS Trans.*, vol. 11, no. 4, pp. 479–493, 2007, doi: 10.1149/1.2779584.

[34] R. K. Chanana, "Is a 600-1000V competitive Wurtzite Germanium Carbide power MOSFET having PECVD SiO 2 as the gate dielectric feasible ? Is a 600-1000V competitive Wurtzite Germanium Carbide power MOSFET having PECVD SiO 2 as the gate dielectric feasible ?," *IOSR J. Electr. Electron. Eng.*, vol. 14, no. 6, pp. 23–24, 2019, doi: 10.9790/1676-1406012324.

[35] M. B. Prince, "Drift Nobilities in Semiconductors. I. Germanium," *Phys. Rev.*, vol. 92, no. 3, 1953, doi: https://doi.org/10.1103/PhysRev.92.681.

[36] C. Choi, "Modeling of Nanoscale MOSFETs (doctoral dissertation)," 2002.

[37] Y. Hoshina, K. Iwasaki, A. Yamada, and M. Konagai, "First-Principles Analysis of Indirect-to-Direct Band Gap Transition of Ge under Tensile Strain," *Jpn. J. Appl. Phys.*, vol. 48, no. 04C125, 2009, doi: 10.1143/JJAP.48.04C125.

[38] J. Michel, J. Liu, and L. C. Kimerling, "High-performance Ge-on-Si

photodetectors," *Nat. Photonics*, vol. 4, no. 8, pp. 527–534, 2010, doi: 10.1038/nphoton.2010.157.

[39] M. Prost *et al.*, "Analysis of optical gain threshold in n-doped and tensile-strained germanium heterostructure diodes," *J. Appl. Phys.*, vol. 118, no. 12, 2015, doi: 10.1063/1.4931580.

[40] J. Jiang *et al.*, "Strain-Induced Enhancement of Electroluminescence from Highly Strained Germanium Light-Emitting Diodes," *ACS Photonics*, vol. 6, no. 4, pp. 915–923, 2019, doi: 10.1021/acsphotonics.8b01553.

[41] Z. Qi, H. Sun, M. Luo, Y. Jung, and D. Nam, "Strained germanium nanowire optoelectronic devices for photonic-integrated circuits," *J. Phys. Condens. Matter*, vol. 30, no. 334004, p. 13pp, 2018, doi: 10.1088/1361-648X/aad0c0.

[42] and K. C. S. Chi On Chui, Kailash Gopalakrishnan, Peter B. Griffin, James D. Plummer, "Activation and diffusion studies of ion-implanted p and n dopants in germanium," *Appl. Phys. Lett.*, vol. 83, no. 16, p. 3275, 2003, doi: 10.1063/1.1618382.

[43] J. Wang and S. Lee, "Ge-photodetectors for Si-based optoelectronic integration," *Sensors*, vol. 11, no. 1, pp. 696–718, 2011, doi: 10.3390/s110100696.

[44] T. R. Harris, Y. K. Yeo, M. Y. Ryu, R. T. Beeler, and J. Kouvetakis, "Observation of heavy- and light-hole split direct bandgap photoluminescence from tensile-strained GeSn (0.03% Sn)," *J. Appl. Phys.*, vol. 116, no. 10, pp. 0–7, 2014, doi: 10.1063/1.4894870.

[45] S. Wirths *et al.*, "Lasing in direct-bandgap GeSn alloy grown on Si," *Nat. Photonics*, vol. 9, no. 2, pp. 88–92, 2015, doi: 10.1038/nphoton.2014.321.

[46] R. Geiger, T. Zabel, and H. Sigg, "Group iv direct band gap photonics: methods, challenges, and opportunities," *Front. Mater.*, vol. 2, no. 52, 2015, doi: 10.3389/fmats.2015.00052.

[47] J. Margetis *et al.*, "Si-Based GeSn Lasers with Wavelength Coverage of 2−3 μm and Operating Temperatures up to 180 K," *ACS Photonics*, vol. 5, no. 3, pp. 827–833, 2018, doi: 10.1021/acsphotonics.7b00938.

[48] V. Reboud *et al.*, "Optically pumped GeSn micro-disks with 16% Sn lasing at 3.1 μm up to 180 K," *Appl. Phys. Lett.*, vol. 111, no. 092101, 2017, doi: 10.1063/1.5000353.

[49] S. Al-Kabi *et al.*, "An optically pumped 2.5 μm GeSn laser on Si operating at 110 K," *Appl. Phys. Lett.*, vol. 109, no. 171105, 2016, doi: 10.1063/1.4966141.

[50] F. Pezzoli, A. Giorgioni, D. Patchett, and M. Myronov, "Temperature-Dependent Photoluminescence Characteristics of GeSn Epitaxial Layers,"

ACS Photonics, vol. 3, no. 11, pp. 2004–2009, 2016, doi: 10.1021/acsphotonics.6b00438.

[51] D. Stange *et al.*, "Optically Pumped GeSn Microdisk Lasers on Si," *ACS Photonics*, vol. 3, no. 7, pp. 1279–1285, 2016, doi: 10.1021/acsphotonics.6b00258.

[52] A. Ghrib *et al.*, "All-Around SiN Stressor for High and Homogeneous Tensile Strain in Germanium Microdisk Cavities," *Adv. Opt. Mater.*, vol. 3, pp. 353–358, 2015, doi: 10.1002/adom.201400369.

[53] D. S. Sukhdeo, D. Nam, J.-H. Kang, M. L. Brongersma, and K. C. Saraswat, "Direct bandgap germanium-on-silicon inferred from 5.7% ⟨100⟩ uniaxial tensile strain [Invited]," *Photonics Res.*, vol. 2, no. 3, pp. A8–A13, 2014, doi: 10.1364/PRJ.2.0000A8.

[54] R. W. Millar *et al.*, "Analysis of Ge micro-cavities with in-plane tensile strains above 2 %," *Opt. Express*, vol. 24, no. 5, p. 4365, 2016, doi: 10.1364/oe.24.004365.

[55] F. T. Armand Pilon *et al.*, "Lasing in strained germanium microbridges," *Nat. Commun.*, vol. 10, no. 2724, 2019, doi: 10.1038/s41467-019-10655-6.

[56] J. Yin, X. Cui, X. Wang, P. Sookchoo, M. G. Lagally, and R. Paiella, "Flexible nanomembrane photonic-crystal cavities for tensilely strained-germanium light emission," *Appl. Phys. Lett.*, vol. 108, no. 241107, 2016, doi: 10.1063/1.4954188.

[57] A. Elbaz *et al.*, "Germanium microlasers on metallic pedestals," *APL Photonics*, vol. 3, no. 106102, 2018, doi: 10.1063/1.5025705.

[58] C. Boztug, J. R. Sánchez-Pérez, F. Cavallo, M. G. Lagally, and R. Paiella, "Strained-Germanium Nanostructures for Infrared Photonics," *ACS Nano*, vol. 8, no. 4, pp. 3136–3151, 2014, doi: 10.1021/nn404739b.

[59] S. Bao *et al.*, "Low-threshold optically pumped lasing in highly strained germanium nanowires," *Nat. Commun.*, vol. 8, no. 1845, 2017, doi: 10.1038/s41467-017-02026-w.

[60] A. Gassenq *et al.*, "1.9% bi-axial tensile strain in thick germanium suspended membranes fabricated in optical germanium-on-insulator substrates for laser applications," *Appl. Phys. Lett.*, vol. 107, no. 191904, 2015, doi: 10.1063/1.4935590.

[61] A. Ghrib *et al.*, "Tensile-strained germanium microdisks," *Appl. Phys. Lett.*, vol. 102, no. 221112, 2013, doi: 10.1063/1.4809832.

[62] J. R. Jain, A. Hryciw, T. M. Baer, D. A. B. Miller, M. L. Brongersma, and R. T. Howe, "A micromachining-based technology for enhancing germanium light emission via tensile strain," *Nat. Photonics*, vol. 6, no. 6, pp. 398–405,

2012, doi: 10.1038/nphoton.2012.111.

[63] M. El Kurdi *et al.*, “Enhanced photoluminescence of heavily n-doped germanium,” *Appl. Phys. Lett.*, vol. 94, no. 19, p. 191107, 2009, doi: 10.1063/1.3138155.

[64] R. E. Camacho-Aguilera *et al.*, “An electrically pumped Ge-on-Si laser,” *Opt. Express*, vol. 20, no. 10, pp. 11316–11320, 2012, doi: 10.1364/ofc.2012.pdp5a.6.

[65] G. He and H. A. Atwater, “Interband Transitions in SnxGe1-x Alloys,” *Phys. Rev. Lett.*, vol. 79, no. 10, pp. 1937–1940, 1997, doi: 10.1103/PhysRevLett.79.1937.

[66] P. Moontragoon, Z. Ikonić, and P. Harrison, “Band structure calculations of Si-Ge-Sn alloys: Achieving direct band gap materials,” *Semicond. Sci. Technol.*, vol. 22, no. 7, pp. 742–748, 2007, doi: 10.1088/0268-1242/22/7/012.

[67] M. R. Bauer *et al.*, “Tunable band structure in diamond-cubic tin-germanium alloys grown on silicon substrates,” *Solid State Commun.*, vol. 127, no. 5, pp. 355–359, 2003, doi: 10.1016/S0038-1098(03)00446-0.

[68] R. Ragan, K. S. Min, and H. A. Atwater, “Direct energy gap group IV semiconductor alloys and quantum dot arrays in SnxGe1 - x/Ge and SnxSi1 - x/Si alloy systems,” *Mater. Sci. Eng. B Solid-State Mater. Adv. Technol.*, vol. 87, no. 3, pp. 204–213, 2001, doi: 10.1016/S0921-5107(01)00732-2.

[69] J. Liu, “Monolithically Integrated Ge-on-Si Active Photonics,” *Photonics*, vol. 1, no. 3, pp. 162–197, 2014, doi: 10.3390/photonics1030162.

[70] M. Chu, Y. Sun, U. Aghoram, and S. E. Thompson, “Strain: A Solution for Higher Carrier Mobility in Nanoscale MOSFETs,” *Annu. Rev. Mater. Res.*, vol. 39, pp. 203–229, 2009, doi: 10.1146/annurev-matsci-082908-145312.

[71] D. S. Sukhdeo, D. Nam, J.-H. Kang, M. L. Brongersma, and K. C. Saraswat, “A Nanomembrane-Based Bandgap-Tunable Germanium Microdisk Using Lithographically-Customizable Biaxial Strain for Silicon-Compatible Optoelectronics,” *ArXiv*, pp. 1–28, 2014, [Online]. Available: http://arxiv.org/abs/1411.0772.

[72] C. G. Van de Walle, “Band lineups and deformation potentials in the model-solid theory,” *Phys. Rev. B*, vol. 39, no. 3, pp. 1871–1883, 1989, doi: https://doi.org/10.1103/PhysRevB.39.1871.

[73] O. Aldaghri, Z. Ikonić, and R. W. Kelsall, “Optimum strain configurations for carrier injection in near infrared Ge lasers,” *J. Appl. Phys.*, vol. 111, no. 053106, 2012, doi: 10.1063/1.3691790.

[74] J. Liu *et al.*, “Deformation potential constants of biaxially tensile stressed Ge

epitaxial films on Si(100)," *Phys. Rev. B*, vol. 70, no. 155309, pp. 1–5, 2004, doi: 10.1103/PhysRevB.70.155309.

[75] M. El Kurdi, G. Fishman, Ś. Sauvage, and P. Boucaud, "Band structure and optical gain of tensile-strained germanium based on a 30 band kp formalism," *J. Appl. Phys.*, vol. 107, no. 013710, 2010, doi: 10.1063/1.3279307.

[76] P. H. Lim, S. Park, Y. Ishikawa, and K. Wada, "Enhanced direct bandgap emission in germanium by micromechanical strain engineering," *Opt. Express*, vol. 17, no. 18, p. 16358, 2009, doi: 10.1364/oe.17.016358.

[77] M. Clavel *et al.*, "Heterogeneously-Grown Tunable Tensile Strained Germanium on Silicon for Photonic Devices," *ACS Appl. Mater. Interfaces*, vol. 7, no. 48, pp. 26470–26481, 2015, doi: 10.1021/acsami.5b07385.

[78] Y. Huo *et al.*, "Strong enhancement of direct transition photoluminescence with highly tensile-strained Ge grown by molecular beam epitaxy," *Appl. Phys. Lett.*, vol. 98, no. 011111, 2011, doi: 10.1063/1.3534785.

[79] Y. Y. Fang *et al.*, "Perfectly tetragonal, tensile-strained Ge on Ge1-ySny buffered Si(100)," *Appl. Phys. Lett.*, vol. 90, no. 061915, 2007, doi: 10.1063/1.2472273.

[80] N. Pavarelli *et al.*, "Optical Emission of a Strained Direct-Band-Gap Ge Quantum Well Embedded Inside InGaAs Alloy Layers," *Phys. Rev. Lett.*, vol. 110, no. 177404, pp. 1–5, 2013, doi: 10.1103/PhysRevLett.110.177404.

[81] Z. M. Huang *et al.*, "Emission of direct-gap band in germanium with Ge-GeSn layers on one-dimensional structure," *Sci. Rep.*, vol. 6, no. 24802, pp. 1–7, 2016, doi: 10.1038/srep24802.

[82] J. Greil, A. Lugstein, C. Zeiner, G. Strasser, and E. Bertagnolli, "Tuning the Electro-optical Properties of Germanium Nanowires by Tensile Strain," *Nano Lett.*, vol. 12, no. 12, pp. 6230–6234, 2012, doi: 10.1021/nl303288g.

[83] C. H. Boztug Yerci, "Tensilely strained germanium nanomembranes for infrared light emitting devices (PhD dissertation)," 2014.

[84] A. Ayan *et al.*, "Strain Engineering of Germanium Nanobeams by Electrostatic Actuation," *Sci. Rep.*, vol. 9, no. 4963, 2019, doi: 10.1038/s41598-019-41097-1.

[85] K. Tani, K. Oda, and T. Ido, "Analysis of stress distribution for strain engineering with external stressors for enhanced light emission in germanium," *Opt. Express*, vol. 28, no. 25, p. 38268, 2020, doi: 10.1364/oe.413503.

[86] G. Capellini *et al.*, "Strain analysis in SiN/Ge microstructures obtained via Si-complementary metal oxide semiconductor compatible approach," *J. Appl. Phys.*, vol. 113, no. 013513, 2013, doi: 10.1063/1.4772781.

[87] R. W. Millar *et al.*, “Extending the emission wavelength of Ge nanopillars to 225 μm using silicon nitride stressors,” *Opt. Express*, vol. 23, no. 14, p. 18193, 2015, doi: 10.1364/oe.23.018193.

[88] A. Ghrib *et al.*, “Control of tensile strain in germanium waveguides through silicon nitride layers,” *Appl. Phys. Lett.*, vol. 100, no. 20, 2012, doi: 10.1063/1.4718525.

[89] G. Capellini *et al.*, “Tensile Ge microstructures for lasing fabricated by means of a silicon complementary metal-oxide-semiconductor process,” *Opt. Express*, vol. 22, no. 1, 2014, doi: 10.1364/OE.22.000399.

[90] M. El Kurdi *et al.*, “Direct Band Gap Germanium Microdisks Obtained with Silicon Nitride Stressor Layers,” *ACS Photonics*, vol. 3, no. 3, pp. 443–448, 2016, doi: 10.1021/acsphotonics.5b00632.

[91] K. Oda, T. Okumura, K. Tani, S. I. Saito, and T. Ido, “Improvement of photoluminescence from Ge layer with patterned Si3N4 stressors,” *Thin Solid Films*, vol. 557, pp. 355–362, 2014, doi: 10.1016/j.tsf.2013.08.117.

[92] J. Ke, L. Chrostowski, and G. Xia, “Stress Engineering with Silicon Nitride Stressors for Ge-on-Si Lasers,” *IEEE Photonics J.*, vol. 9, no. 2, pp. 1–15, 2017, doi: 10.1109/JPHOT.2017.2675401.

[93] D. Nam *et al.*, “Strained germanium thin film membrane on silicon substrate for optoelectronics,” *Opt. Express*, vol. 19, no. 27, pp. 25866–25872, 2011, doi: 10.1364/OE.19.025866.

[94] D. Nam *et al.*, “Electroluminescence from strained germanium membranes and implications for an efficient Si-compatible laser,” *Appl. Phys. Lett.*, vol. 100, no. 131112, 2012, doi: 10.1063/1.3699224.

[95] B. J. H. Stadler, *Vapor Processes*. Elsevier Inc., 2016.

[96] C. L. Claeys and E. R. Simoen, “Stress-induced Defect Generation,” in *Encyclopedia of Materials: Science and Technolog*, no. 3, P. V. K.H. Jürgen Buschow, Robert W. Cahn, Merton C. Flemings, Bernhard Ilschner, Edward J. Kramer, Subhash Mahajan, Ed. 2001, pp. 8904–8912.

[97] Y. Sun, S. E. Thompson, and T. Nishida, *Strain Effect in Semiconductors: Theory and Device Applications*. New York, 2010.

[98] J. R. Sanchez-Perez *et al.*, “Direct-bandgap light-emitting germanium in tensilely strained nanomembranes,” *Proc. Natl. Acad. Sci.*, vol. 108, no. 47, pp. 18893–18898, 2011, doi: 10.1073/pnas.1107968108.

[99] R. S. Jacobsen *et al.*, “Strained silicon as a new electro-optic material,” *Nature*, vol. 441, no. 7090, pp. 199–202, 2006, doi: 10.1038/nature04706.

[100] S. W. Bedell *et al.*, “Kerf-Less Removal of Si, Ge, and III–V Layers by Controlled Spalling to Enable Low-Cost PV Technologies,” *IEEE J.*

Photovoltaics, vol. 2, no. 2, pp. 141–147, 2012, doi: 10.1109/JPHOTOV.2012.2184267.

[101] S. Saito *et al.*, "Group IV Light Sources to Enable the Convergence of Photonics and Electronics," *Front. Mater.*, vol. 1, no. September, pp. 1–15, 2014, doi: 10.3389/fmats.2014.00015.

[102] S. Saito, A. Z. Al-Attili, K. Oda, and Y. Ishikawa, "Towards monolithic integration of germanium light sources on silicon chips," *Semicond. Sci. Technol.*, vol. 31, no. 043002, p. 19pp, 2016, doi: 10.1088/0268-1242/31/4/043002.

[103] Y. Ishikawa, K. Wada, D. D. Cannon, J. Liu, H.-C. Luan, and L. C. Kimerling, "Strain-induced band gap shrinkage in Ge grown on Si substrate," *Appl. Phys. Lett.*, vol. 82, no. 13, pp. 2044–2046, 2003, doi: 10.1063/1.1564868.

[104] X. Li and R. Yang, "Effect of lattice mismatch on phonon transmission and interface thermal conductance across dissimilar material interfaces," *Phys. Rev. B*, vol. 86, no. 5, 2012, doi: 10.1103/PhysRevB.86.054305.

[105] G. D. M. Sune Pettersson, "Theory of the thermal boundary resistance between dissimilar lattices," *Phys. Rev. B*, vol. 42, no. 12, pp. 7386–7390, 1990, [Online]. Available: http://prb.aps.org/abstract/PRB/v42/i12/p7386_1.

[106] L. Carroll *et al.*, "Direct-Gap Gain and Optical Absorption in Germanium Correlated to the Density of Photoexcited Carriers, Doping, and Strain," *Phys. Rev. Lett.*, vol. 109, no. 057402, pp. 1–5, 2012, doi: 10.1103/PhysRevLett.109.057402.

[107] C. Yi-Ping Chao and S. Lien Chuang, "Spin-orbit-coupling effects on the valence-band structure of strained semiconductor quantum wells," *Phys. Rev. B*, vol. 46, no. 7, 1992, doi: https://doi.org/10.1103/PhysRevB.46.4110.

[108] S. L. Chuang, *Physics of Photonic Devices*, 2nd ed. Hoboken, New Jersey: John Wiley & Sons, Inc., 2009.

[109] Y. Sun, S. E. Thompson, and T. Nishida, "Physics of strain effects in semiconductors and metal-oxide-semiconductor field-effect transistors," *J. Appl. Phys.*, vol. 101, no. 10, 2007, doi: 10.1063/1.2730561.

[110] T. Inaoka, Y. Kinjyo, S. Yanagisawa, and K. Tomori, "Anisotropy of the silicon valence band induced by strain with various orientations," *J. Appl. Phys.*, vol. 113, no. 18, 2013, doi: 10.1063/1.4804412.

[111] C. G. Van de Walle and R. M. Martin, "Theoretical calculations of heterojunction discontinuities in the Si/Ge system," *Phys. Rev. B*, vol. 34, no. 8, pp. 5621–5634, Oct. 1986, doi: 10.1103/PhysRevB.34.5621.

[112] Y. S. Choi, J. S. Lim, T. Numata, T. Nishida, and S. E. Thompson, "Mechanical stress altered electron gate tunneling current and extraction of

conduction band deformation potentials for germanium," *J. Appl. Phys.*, vol. 102, no. 10, 2007, doi: 10.1063/1.2809374.

[113] I. Balslev, "The influence of high uniaxial stress on the indirect absorption edge in silicon," *Solid State Commun.*, vol. 3, no. 8, pp. 213–218, 1965, doi: 10.1016/0038-1098(65)90294-2.

[114] M. V. Fischetti and S. E. Laux, "Band structure, deformation potentials, and carrier mobility in strained Si Ge, and SiGe alloys," *J. Appl. Phys.*, vol. 80, pp. 2234–2252, 1996, doi: 10.1063/1.363052.

[115] T. C. Chong and C. G. Fonstad, "Theoretical Gain of Strained-Layer Semiconductor Lasers in the Large Strain Regime," *IEEE J. Quantum Electron.*, vol. 25, no. 2, pp. 171–178, 1989, doi: 10.1109/3.16260.

[116] R. Geiger, "Direct Band Gap Germanium for Si-compatible Lasing (PhD dissertation)," 2016.

[117] D. Nam, D. S. Sukhdeo, B. R. Dutt, and K. C. Saraswat, "(Invited) Light Emission from Highly-Strained Germanium for On-Chip Optical Interconnects," *ECS Trans.*, vol. 64, no. 6, pp. 371–381, 2014, doi: 10.1149/06406.0371ecst.

[118] D. S. Sukhdeo, Y. Kim, S. Gupta, K. C. Saraswat, B. R. Dutt, and D. Nam, "Anomalous threshold reduction from <100> uniaxial strain for a low-threshold Ge laser," *Opt. Commun.*, vol. 379, pp. 32–35, 2016, doi: 10.1016/j.optcom.2016.05.030.

[119] Y. Liu, M. D. Deal, and J. D. Plummer, "High-quality single-crystal Ge on insulator by liquid-phase epitaxy on Si substrates," *Appl. Phys. Lett.*, vol. 84, no. 14, 2004, doi: 10.1063/1.1691175.

[120] Y. Liu, M. D. Deal, and J. D. Plummer, "Rapid Melt Growth of Germanium Crystals with Self-Aligned Microcrucibles on Si Substrates," *J. Electrochem. Soc.*, vol. 152, no. 8, pp. G688–G693, 2005, doi: 10.1149/1.1946368.

[121] Y. Liu, M. D. Deal, and J. D. Plummer, "High-quality single-crystal Ge on insulator by liquid-phase epitaxy on Si substrates," *Appl. Phys. Lett.*, vol. 84, no. 14, 2004, doi: 10.1063/1.1691175.

[122] I. Mizushima, T. Sadoh, and M. Miyao, "Formation of Ge-on-Insulator Structures on Si Platform by SiGe-Mixing-Triggered Rapid-Melting Growth using RTA Technique," *2013 13th Int. Work. Junction Technol.*, pp. 30–31, 2013, doi: 10.1109/IWJT.2013.6644498.

[123] C. G. Littlejohns *et al.*, "Next Generation Device Grade Silicon-Germanium on Insulator," *Sci. Rep.*, vol. 5, no. 8288, 2015, doi: 10.1038/srep08288.

[124] M. Matsue, Y. Yasutake, S. Fukatsu, T. Hosoi, T. Shimura, and H. Watanabe, "Strain-induced direct band gap shrinkage in local Ge-on-insulator structures

fabricated by lateral liquid-phase epitaxy," *Appl. Phys. Lett.*, vol. 104, no. 031106, 2014, doi: 10.1063/1.4862890.

[125] M. Ohring, *Materials Science of Thin Films*. 2002.

[126] B. B. Sahu, Y. Y. Yin, T. Tsutsumi, M. Hori, and J. G. Han, "The role of plasma chemistry on functional silicon nitride film properties deposited at low-temperature by mixing two frequency powers using PECVD," *Phys. Chem. Chem. Phys.*, vol. 18, pp. 13033–13044, 2016, doi: 10.1039/c6cp00986g.

[127] R. R. Nistala, X. Zhu, X. Li, D. Lin, S. K. Singh, and S. P. Zhao, "Si (004) measurements of wafer curvature due to the stress introduced by PECVD / HDP SiN films in wafer fabrication," *2017 IEEE 24th Int. Symp. Phys. Fail. Anal. Integr. Circuits*, pp. 1–4, 2017, doi: 10.1109/IPFA.2017.8060139.

[128] M. J. Mescher, M. L. Reed, and T. E. Schlesinger, "Stress control in sputtered silicon nitride films," in *Materials Research Society Symposium - Proceedings*, 1997, vol. 472, pp. 239–244, doi: 10.1557/proc-472-239.

[129] V. Bhatt and S. Chandra, "Silicon nitride films deposited by RF sputtering for microstructure fabrication in MEMS," *J. Electron. Mater.*, vol. 38, no. 9, pp. 1979–1989, 2009, doi: 10.1007/s11664-009-0846-8.

[130] K. R. Williams, K. Gupta, and M. Wasilik, "Etch rates for micromachining processing - Part II," *J. Microelectromechanical Syst.*, vol. 12, no. 6, pp. 761–778, 2003, doi: 10.1109/JMEMS.2003.820936.

[131] J. Akedo, J. Park, and H. Tsuda, "Fine patterning of ceramic thick layer on aerosol deposition by lift-off process using photoresist," *J. Electroceramics*, vol. 22, no. 1–3, pp. 319–326, 2009, doi: 10.1007/s10832-007-9385-y.

[132] A. Gassenq *et al.*, "Accurate strain measurements in highly strained Ge microbridges," *Appl. Phys. Lett.*, vol. 108, no. 24, pp. 1–10, 2016, doi: 10.1063/1.4953788.